Université du Québec

INRS Institut national de la recherche scientifique

Centre Énergie Matériauxet Télécommunications

Catalyst Design at Atomic Level for the Electrochemical Carbon Dioxide Reduction

Par

Zhangsen Chen

Thèse présentée pour l'obtention du grade de

Philosophiae Doctor (Ph.D.)

en sciences de l'énergie et des matériaux

Jury d'évaluation

Président du jury et examinateur interne	Prof. Andreas Ruediger INRS-EMT, Canada
Examinateur externe	Prof. Mohamed Siaj Université du Québec à Montréal Canada
Examinateur externe	Prof. Xiaolei Wang University of Alberta, Canada
Directeur de recherche	Prof. Shuhui Sun INRS-EMT, Canada

© Droits réservés de *Zhangsen Chen*, 05 2023

REMERCIEMENTS

First, I would like to thank Prof. Shuhui Sun for allowing me to study in his group at INRS-EMT. And my sincere gratitude for his patient guidance, constructive suggestions, and constant encouragement during my Ph.D. study. Prof. Sun allowed me to explore my research ideas freely with patience and his full support. His profound insights and academic accuracy help me make big progress in my research. Besides, Prof. Sun's kindness and care for colleagues and students are engraved in my heart. I could not accomplish my Ph.D. study without his supervision.

I would also like to express my gratitude to my jury members, including Prof. Andreas Ruediger, Prof. Mohamed Siaj, and Prof. Xiaolei Wang, for their invested time and effort on the jury committee. Thanks to Prof. Mohamed Mohamedi and Prof. Luca Razzari for their advice on my doctoral exam, which has been a great help in later research.

I would like to offer my special thanks to Prof. Gaixia Zhang for her valuable instructions and support throughout my Ph.D. study. I learned so much from her profound comments on my research and paper writing. Guided by her extensive knowledge and rigorous academic attitude, I was able to sharpen my scientific perspective and achieve my research goals. Prof. Zhang's willingness to give her time so generously has been very much appreciated.

I am honored to work in Prof. Sun's research group full of hardworking and supportive colleagues. Special thanks to Dr. Mingjie Wu, Dr. Xin Tong, Dr. Xiaohua Yang, Dr. Lei Du, Prof. Jai Prakash, Diane Rawach, Dr. Zonghua Pu, Jun Zhang, Hongliu Dai, Dr. Qingmin Hu, Huiyu Lei, Fang Dong, Dr. Pan Wang, Sixiang Liu, Dr. Ke Wang, Dr. Nathaneal Komba, Dr. Amir Hasanpour, and so on. The Ph.D. life became easier and more colorful along with them. I would like to express my gratitude to all the professors who have taught me at INRS that greatly broadened my horizon and enriched my knowledge. I would also like to thank the colleagues outside Prof. Sun's group for their collaborative work, especially Dr. Simon Vallieres and Dr. Hui Zhang. The collaborations are inspiring and fulfilling. I thank all the administrative staff at INRS for their help and support.

My sincere gratitude to Prof. Yi Zheng for the introduction to Prof. Sun and her support at the beginning of my Ph.D. study.

I am grateful to the beam scientists at Canadian Light Source, special thanks to Dr. Ning Chen, Dr. Teak Boyko, Dr. Jian Wang, Dr. Yongfeng Hu, Dr. Jigang Zhou, Dr. Mohsen Shakouri, Dr. Qunfeng Xiao, Dr. Weifeng Chen, Dr. Tom Regier, Dr. Jay Dynes, Dr. Roman Chernikov, Dr.

Emilio Heredia, Dr. Scott Rosendahl, and Dr. Stuart Read for their technical assistance and guidance. In addition, I thank the support from the CLSI Student Travel Support Program.

I also would like to acknowledge INRS for the financial support.

Finally, I would like to extend my deep gratitude to my family and friends for their constant care and unconditional support.

RÉSUMÉ

Le dioxyde de carbone (CO_2) est l'un des produits finaux de la combustion de carburant et le principal composant des gaz à effet de serre. La réduction du CO_2 atmosphérique diminue non seulement la pollution de l'environnement, mais produit également des produits chimiques à valeur ajoutée, offrant une solution possible aux problèmes énergétiques et environnementaux simultanément. Un défi fatal est la faible efficacité de conversion de la réduction du CO_2 en raison de l'inertie de la molécule de CO_2. La conception des nanomatériaux catalyseurs avec une sélectivité, une stabilité et des capacités d'activation élevées pour la conversion du CO_2 est nécessaire.

Les catalyseurs à un seul atome (SAC) dérivés de la structure imidazolate zéolitique (ZIF-8) sont largement étudiés dans de nombreuses réactions catalytiques telles que la réaction de dégagement d'hydrogène (HER), la réaction de réduction de l'oxygène (ORR) et les réactions de réduction du CO_2 (CO_2RR). Les procédures de broyage impliquées dans la synthèse des SAC dérivés de ZIF-8 pourraient affecter les performances catalytiques mais sont moins évaluées dans la littérature. Ce travail présente une série de SAC de cobalt dérivés de ZIF-8 (C-Co-ZIF) avec différents processus de broyage pour étudier l'impact des degrés de broyage sur les performances de la réaction de réduction électrochimique du CO_2 (ECO_2RR). Le processus de broyage modéré offre une augmentation de l'efficacité faradique du CO (FE, environ 15 % supérieure à celle du C-Co-ZIF d'origine) et les densités de courant les plus élevées parmi tous les échantillons. Les variations de la structure électronique des sites actifs Co dans les catalyseurs broyés sont confirmées par la spectroscopie d'absorption des rayons X (XAS) et la spectroscopie d'émission des rayons X (XES) pour des performances catalytiques améliorées. L'augmentation des micro-pores dans le catalyseur modérément broyé fournit des sites actifs plus exposés tandis que l'augmentation des méso- et macro-pores favorise le transfert de masse, ce qui profite aux performances ECO_2RR. Cela suggère que l'impact des processus de broyage sur la synthèse des SAC dérivés de ZIF-8 devrait être pris en compte pour l'évaluation des performances catalytiques.

Les catalyseurs dispersés atomiquement à base de métaux de transition sont prometteurs pour la sélectivité et l'activité élevées dans ECO_2RR. Inspiré par les résultats prometteurs obtenus avec les précédents Co-SAC, la combinaison de Co avec d'autres éléments de métaux de transition pour fabriquer des SAC multimétalliques est proposée pour promouvoir les performances d'ECO_2RR. Une série de catalyseurs bimétalliques Co, Fe dispersés atomiquement

en carbonisant le cadre Co-zéolitique-imidazolate introduit par Fe (C-Fe-Co-ZIF) pour la génération de gaz de synthèse à partir d'ECO_2RR est présentée. L'effet synergique du catalyseur bimétallique favorise la production de CO. Comparé au C-Co-ZIF pur, le C-Fe-Co-ZIF facilite la production de CO avec une augmentation de l'efficacité faradique (FE) du CO, avec un FE_{CO} optimal d'environ 52 %, un FE_{H2} d'environ 42 % à -0,55 V et du CO densité de courant de 8,0 mA cm^{-2} à -0,7 V vs électrode à hydrogène réversible (RHE). Le rapport H_2/CO est réglable de 0,8 à 4,2 dans une large fenêtre de potentiel de -0,35 à -0,8 V vs RHE. Le total FE_{CO+H2} se maintient à 93 % sur 10 heures. La bonne quantité d'ajout de Fe pourrait augmenter le nombre de sites actifs et créer de légères distorsions pour les environnements nanoscopiques de Co et Fe, ce qui est essentiel pour l'amélioration de la production de CO dans ECO_2RR. Les impacts positifs des catalyseurs bimétalliques Cu-Co et Ni-Co démontrent la polyvalence et l'application potentielle de la stratégie bimétallique pour ECO_2RR.

Avec les preuves montrant le potentiel de Fe dans ECO_2RR, des SAC de Fe fabriqués à partir de la pyrolyse à haute température assistée par ZIF sont fabriqués. Les Fe SACs autorisent le FEco jusqu'à 76 %, ce qui est supérieur à ceux des Co-SACs précédents. Le dépôt de couche atomique (ALD), capable de construire des catalyseurs avec une précision au niveau atomique de manière hautement contrôlable, est une technique prometteuse pour résoudre les problèmes clés de la réduction du CO_2. Les Fe-SAC revêtus d'ALD-Al_2O_3 sont préparés pour effectuer les tests ECO_2RR. La bonne quantité de revêtement ALD-Al_2O_3 (25 cycles d'ALD) peut légèrement favoriser le FEco de FeNC jusqu'à 80 %. En plus, l'ALD-Al_2O_3 peut empêcher de manière significative le vieillissement du FeNC. 25 ALD-Al_2O_3 FeNC a même maintenu son activité ECO_2RR après le vieillissement de 10 mois. L'importance des catalyseurs ALD à structure fine reste à explorer pour mieux comprendre les bénéfices catalytiques en termes de performances dans le futur.

Mots-clés : Réduction du CO_2, électrocatalyse, production de gaz de synthèse, cobalt, fer, catalyseurs dérivés du ZIF-8, procédé de broyage, catalyseurs bimétalliques, dépôt de couche atomique

ABSTRACT

Carbon dioxide (CO_2) is one of the end products of fuel combustion and the major component of greenhouse gases. The reduction of atmospheric CO_2 not only decreases environmental pollution but also produces value-added chemicals, providing a possible solution to energy and environment issues simultaneously. One fatal challenge is the low conversion efficiency of CO_2 reduction due to the inertness of the CO_2 molecule. The design of the catalyst nanomaterials with high selectivity, stability, and activation capabilities for the conversion of CO_2 is needed.

The zeolitic imidazolate framework (ZIF-8) derived single-atom catalysts (SACs) are widely studied in many catalytic reactions such as hydrogen evolution reaction (HER), oxygen reduction reaction (ORR), and CO_2 reduction reactions (CO_2RR). Grinding procedures involved in the synthesis of ZIF-8-derived SACs could affect the catalytic performance but are less evaluated in the literature. This work presents a series of ZIF-8-derived cobalt SACs (C-Co-ZIFs) with different grinding processes to investigate the impact of the grinding degrees on the performance of the electrochemical reduction reaction of CO_2 (ECO_2RR). The moderate grinding process affords a boost in CO Faradaic efficiency (FE, around 15 % higher than that of the original C-Co-ZIF) and the highest current densities among all the samples. The variations in the electronic structure of the Co active sites in the ground catalysts are confirmed by X-ray absorption spectroscopy (XAS) and X-ray emission spectroscopy (XES) for improved catalytic performance. The increased micro-pores in the moderately ground catalyst provide more exposed active sites while the increased micro- and macro-pores promote the active site hosting and mass transfer, respectively, benefiting the ECO_2RR performance. It suggests that the impact of grinding processes on the synthesis of ZIF-8-derived SACs should be considered for the evaluation of the catalytic performance.

Transition metal-based atomically dispersed catalysts are promising for the high selectivity and activity in ECO_2RR. Inspired by the promising results obtained from the previous Co-SACs, the combination of Co with other transition metal elements to fabricate multi-metallic SACs is proposed to promote the ECO_2RR performance. A series of atomically dispersed Co, Fe bimetallic catalysts by carbonizing the Fe-introduced Co-zeolitic-imidazolate-framework (C-Fe-Co-ZIF) for the syngas generation from ECO_2RR are presented. The synergistic effect of the bimetallic catalyst promotes CO production. Compared to the pure C-Co-ZIF, C-Fe-Co-ZIF facilitates CO production with a CO FE boost, with optimal FE_{CO} of around 52%, FE_{H2} of around 42% at -0.55 V, and CO current density of 8.0 mA cm^{-2} at -0.7 V vs reversible hydrogen electrode (RHE). The

H_2/CO ratio is tunable from 0.8 to 4.2 in a wide potential window of -0.35 to -0.8 V vs. RHE. The total FE_{CO+H2} maintains as high as 93% over 10 hours. The proper adding amount of Fe could increase the number of active sites and create mild distortions for the nanoscopic environments of Co and Fe, which is essential for the enhancement of the CO production in ECO_2RR. The positive impacts of Cu-Co and Ni-Co bimetallic catalysts demonstrate the versatility and potential application of the bimetallic strategy for ECO_2RR.

With the evidence showing the potential of Fe in ECO_2RR, Fe SACs made from ZIF-assisted high-temperature pyrolysis are fabricated. The Fe SACs allow the FEco up to 76 %, which is higher than those of the previous Co-SACs. Atomic layer deposition (ALD), capable of constructing catalysts with atomic-level precision in a highly controllable manner, is a promising technique to address the key problems in CO_2 reduction. The ALD-Al_2O_3-coated Fe-SACs are prepared to conduct the ECO_2RR tests. The proper amount of ALD-Al_2O_3 coating (25 cycles of ALD) can slightly promote the FEco of FeNC up to 80%. 25 ALD-Al_2O_3 FeNC even maintained its ECO_2RR activity after the aging of 10 months. The significance of the ALD catalysts with fine structures remains to be explored to obtain a better understanding of the catalytic-performance-aimed benefits in the future.

Keywords: CO_2 reduction, electrocatalysis, syngas production, cobalt, iron, ZIF-8 derived catalysts, grinding process, bimetallic catalysts, atomic layer deposition

SOMMAIRE RÉCAPITULATIF

La surémission de CO_2 dans l'atmosphère a été l'une des principales préoccupations de la société humaine. En attendant, le CO_2 peut servir de matière première pour de nombreuses productions chimiques. Si nous pouvons réduire le CO_2 en produits à valeur ajoutée grâce à des conditions catalytiques douces telles que ECO_2RR qui utilise l'électricité provenant d'énergies renouvelables, il serait souhaitable de consommer le CO_2 surémis et de produire des carburants chimiques supplémentaires pour la crise énergétique. Ces dernières années, les SAC sont extrêmement populaires dans le domaine ECO_2RR en raison de leurs sites actifs très efficaces et de leur capacité à maximiser l'utilisation des atomes métalliques. Les SAC à base de métaux de transition sont très prometteurs pour la production de CO et de gaz de synthèse dans ECO_2RR. Par conséquent, nous avons choisi la fabrication de catalyseurs de SAC à base de métaux de transition via la méthode du modèle ZIF qui a été largement étudiée dans la littérature ainsi que la technique avancée de dépôt de couche atomique (ALD) pour mener ce travail afin d'étudier la relation entre la modification subtile du SAC et la catalyse. performance.

Dans le premier travail, nous avons préparé les SAC dérivés de Co-ZIF. Combinant différents procédés de broyage tels que le broyage manuel et le broyage à billes pour créer différents degrés de Co SAC broyés (broyage manuel et broyage à billes pour les degrés de broyage modéré et intense, respectivement), les catalyseurs ont été testés dans ECO_2RR. Le Co SAC d'origine (C-Co-ZIF) qui est sans aucun processus de broyage présente un FEco d'environ 45 % et un FE_{H2} d'environ 50 % à -0,55 V par rapport à RHE et une densité de courant CO d'environ 5 mA cm^{-2} à -0,7 V par rapport à RHE. L'échantillon modérément broyé offre le FEco le plus élevé d'environ 60 % (environ 15 % supérieur à celui du C-Co-ZIF d'origine) à -0,55 V par rapport à RHE et la densité de courant de CO la plus élevée d'environ 12 mA cm^{-2} (plus de 2 fois supérieur à celui du C-Co-ZIF d'origine) à -0,7 V par rapport à RHE. En revanche, l'échantillon intensément broyé n'offre que des activités catalytiques comparables à celles du C-Co-ZIF d'origine. Cela suggère que le processus de broyage modéré favorise la production de CO à la fois dans la sélectivité et l'activité de la production. En outre, l'échantillon modérément broyé offre également une meilleure stabilité que celle du Co SAC d'origine. La spectroscopie d'absorption des rayons X (XAS) et la spectroscopie d'émission de rayons X (XES) confirment que le processus de broyage crée des variations dans la structure électronique des sites actifs Co dans les catalyseurs. Les analyses TEM et de sorption de gaz prouvent l'effet de réduction de taille et l'augmentation des structures de pores de l'échantillon modérément broyé. Les variations des structures électroniques des sites actifs et des structures de pores (micro-pores pour exposer les

sites actifs, méso- et macro-pores pour favoriser le transfert de masse) sont les clés de la performance ECO_2RR promue, qui guide la synthèse de ZIF-8 dérivé SAC pour les réactions catalytiques. À notre connaissance, ce travail est le premier à combiner le XES basé sur le synchrotron avec le XAS pour étudier les variations subtiles des états chimiques pour les effets de broyage sur les SAC.

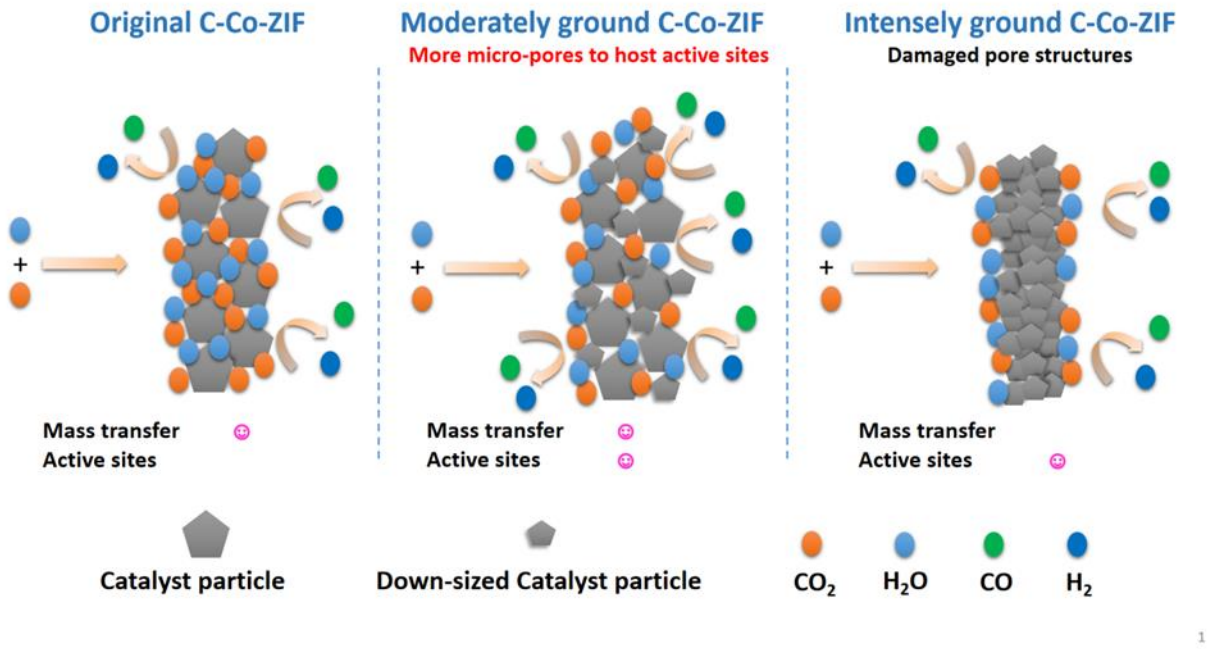

Le bref résumé du premier travail

Dans le deuxième travail, nous rapportons un catalyseur bimétallique avec des sites Co et Fe dispersés atomiquement pour l'ECO_2RR hautement efficace pour la production de gaz de synthèse, qui est notre tentative préliminaire pour comprendre l'interaction entre Co et Fe et sa contribution à la performance catalytique. Les catalyseurs bimétalliques sont fabriqués en utilisant ZIF-8 comme précurseur. Le Co-ZIF est d'abord construit sur le précurseur ZIF, suivi de l'introduction de Fe. L'introduction de Fe dans Co-ZIF (Fe-Co-ZIF) crée l'interaction entre les sites Co et Fe dans les catalyseurs carbonisés finaux (C-Fe-Co-ZIF-x, x est la quantité d'ajout de Fe (% en poids) dans le précurseur ZIF). La spectroscopie photoélectronique à rayons X (XPS) montre que l'introduction de Fe avec la quantité appropriée pourrait augmenter le nombre de sites M-N dans le catalyseur, favorisant les performances ECO_2RR. Les interactions des différents TM dans les catalyseurs bimétalliques sont indiquées par spectroscopie d'absorption des rayons X (XAS). Cela confirme que l'environnement de coordination de Co est déformé par l'ajout de Fe dans les catalyseurs bimétalliques. Des mesures électrochimiques sont effectuées pour étudier

les performances catalytiques des C-Fe-Co-ZIF. C-Fe-Co-ZIF-1.6 wt%-Fe qui présente de légères distorsions dans les sites Co-N et Fe-N présente les meilleures performances ECO_2RR vis-à-vis de la production de CO tout en maintenant le FE_{CO+H2} total élevé d'environ 93% pendant plus de 10 heures. Il est confirmé que les catalyseurs bimétalliques Cu-Co et Ni-Co (Cu carbonisé et Co-ZIF modifié au Ni) sont capables de promouvoir les performances ECO_2RR, démontrant la polyvalence de la stratégie des SAC bimétalliques. Ce travail étudie systématiquement l'interaction entre différents métaux dans des catalyseurs bimétalliques à dispersion atomique pour ECO_2RR, fournissant des informations intéressantes sur la conception du catalyseur pour la prochaine génération.

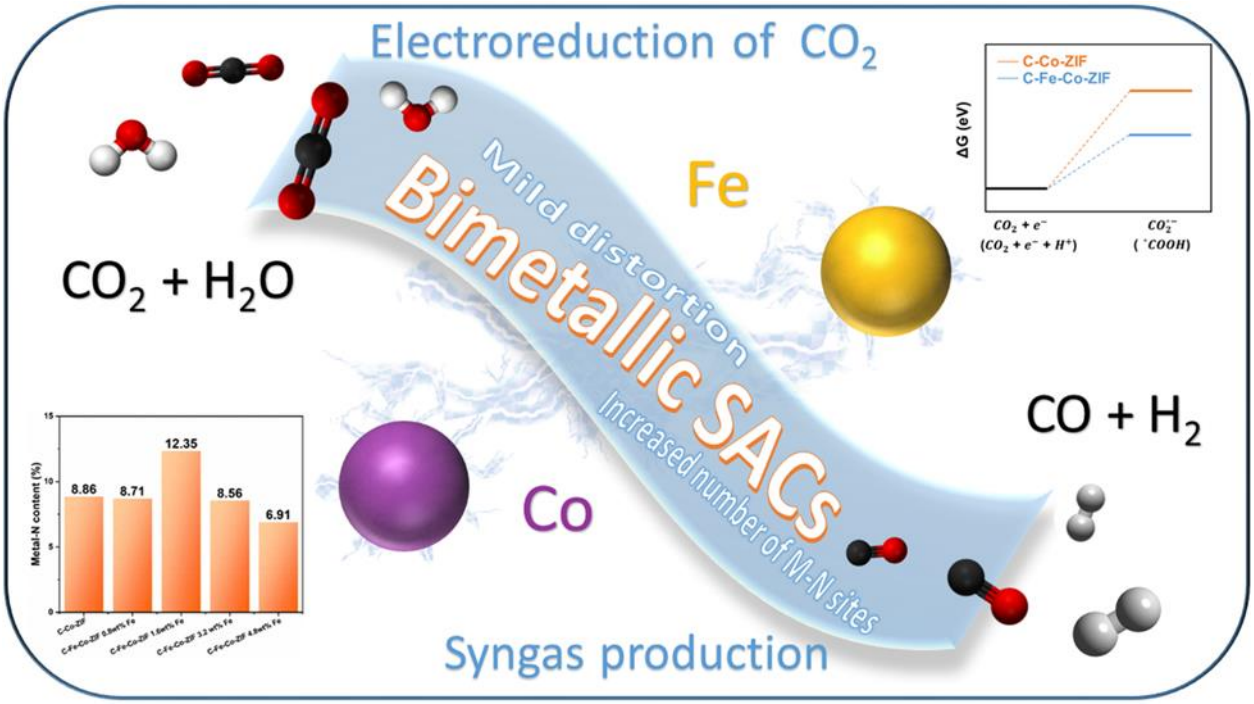

Le bref résumé du deuxième ouvrage

Dans le troisième travail, FeNC a été préparé sous forme de Fe SAC pour effectuer ECO_2RR et a atteint un FEco élevé d'environ 76 % à -0,45 V et -0,5 V par rapport à RHE. La technique ALD a été utilisée pour ajouter ALD-Al_2O_3 sur FeNC. Les 25 cycles d'ALD-Al_2O_3 peuvent légèrement améliorer le FEco de FeNC élevé d'environ 80% à -0,45 V par rapport à RHE. En plus, 25 ALD-Al_2O_3 FeNC conserve parfaitement l'activité catalytique d'ECO_2RR après le vieillissement de 10 mois. Cela signifie que l'ALD-Al_2O_3 détient un grand potentiel dans la protection des catalyseurs dans les applications industrielles.

Des mesures caractéristiques avancées telles que des caractérisations in-situ et ex-situ doivent être effectuées pour comprendre le mécanisme sous-jacent de la promotion de la production de CO par ALD-Al_2O_3 et prévenir le problème de vieillissement dans ECO_2RR de FeNC à l'avenir.

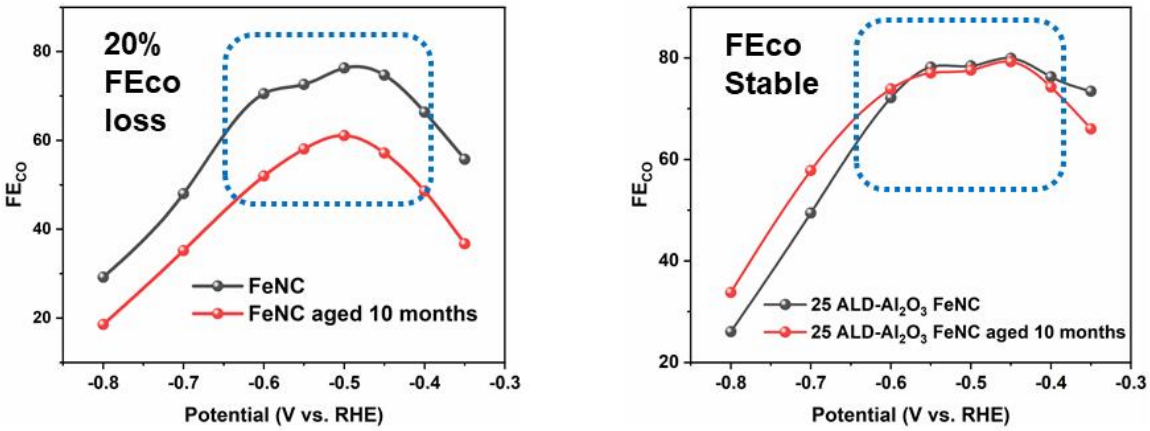

ALD-Al_2O_3 empêche la perte FEco de FeNC due au vieillissement

En outre, combiné avec les découvertes des deux travaux de recherche précédents, pour mieux utiliser la stratégie de couche ALD, nous pouvons appliquer des matériaux actifs ECO_2RR en tant que couches ALD sur FeNC pour améliorer encore la stabilité. Co et Ni sont de bons candidats de métaux de transition pour mener les expériences, dont les précurseurs ALD ont déjà signalé. Pour ALD-NiO, le bis(cyclopentadiényl)nickel(II) ($Ni(cp)_2$) est le précurseur de Ni et O_2 est le précurseur d'oxydation. Pour ALD-CoO, le bis(cyclopentadiényl)cobalt(II) ($Co(cp)_2$) est le précurseur de Co et O_2 est le précurseur d'oxydation. La structure et l'épaisseur des matériaux ALD seront contrôlées par le temps d'exposition au gaz précurseur et le nombre de cycles ALD. Dans l'intervalle, un revêtement ALD multimétallique (par exemple, un dépôt de couche bimétallique tel que le revêtement Co-Ni ALD) peut également être fabriqué pour étendre le potentiel catalytique de l'ALD dans ECO_2RR.

TABLE DES MATIÈRES

LISTE DES FIGURES

LISTE DES TABLEAUX

LISTE DES ÉQUATIONS

LISTE DES ABRÉVIATIONS

Atomic layer deposition	ALD
atomic layer epitaxy	ALE
back-scattered electrons	BSE
ball-milled	BM
ball-milled 60 mins	BM 60 mins
ball-milled 30 mins	BM 30 mins
bis(cyclopentadienyl)cobalt(II)	$Co(cp)_2$
bis(cyclopentadienyl)nickel(II)	$Ni(cp)_2$
Brunauer, Emmett, and Teller theory	BET
Canadian Light Source	CLS
carbon capture and storage	CCS
carbon dioxide	CO_2
carbon nanotube	CNT
carbonized Co-based ZIF-8	C-Co-ZIF
carbonized Cu-Co-ZIF	C-Cu-Co-ZIF
carbonized Fe introduced Co-ZIF	C-Fe-Co-ZIF
carbonized Ni-Co-ZIF	C-Ni-Co-ZIF
cathodoluminescence	CL
chemical vapor deposition	CVD

CO_2 reduction reactions	CO_2RR
Co-based ZIF-8	Co-ZIF
Co-zeolitic-imidazolate-framework	C-Fe-Co-ZIF
cyclic voltammetry	CV
electrochemical impedance spectroscopy	EIS
electrochemical reduction reaction of CO_2	ECO_2RR
electrochemical surface area	ECSA
electron binding energy	$E_{binding}$
elliptically polarized undulators	EPUs
Energy Dispersive X-Ray Spectroscopy	EDS
extended x-ray absorption fine structure	EXAFS
Faradaic efficiency	FE
Fe introduced Co-ZIF	Fe-Co-ZIF
gas chromatography	GC
gas diffusion electrode	GDE
hand-milled	HM
hand-millED 15 mins	HM 15 mins
Hard X-ray MicroAnalysis	HXMA
high-angle annular dark-field scanning transmission electron microscopy	HAADF-STEM

High-Resolution Spherical Grating Monochromator	SGM
high-resolution transmission electron micrograph	HRTEM
hydrogen evolution reaction	HER
Inductively coupled plasma-optical emission spectrometry	ICP-OES
Intergovernmental Panel on Climate Change	IPCC
ion chromatography	IC
kinetic energy	$E_{kinetic}$
linear sweeping voltammetry	LSV
metal-organic frameworks	MOFs
methyl	Me
methylene blue	MB
mol / L	M
multi-walled carbon nanotubes	MWCNTs
Normal Hydrogen Electrode	NHE
nuclear magnetic resonance	NMR
open circuit potential	OCP
oxygen evolution reaction	OER
oxygen reduction reaction	ORR
palladium	Pd

partial fluorescence yield	PFY
parts per million	ppm
photoelectrocatalytic	PEC
photon energy	hv
platinum	Pt
rate-determining step	RDS
Resonant Elastic and Inelastic X-ray Scattering	REIXS
Resonant Inelastic X-ray Scattering	RIXS
reversible hydrogen electrode	RHE
scanning electron microscopy	SEM
scanning TEM imaging	STEM
secondary electrons	SE
selected-area electron-diffraction	SAED
single-atom catalysts	SACs
standard cubic centimeters per minute	SCCM
The current densities of CO	j_{co}
The current densities of H_2	j_{H2}
thermal conductivity detector	TCD
total current	A
total electron yield	TEY

transmission electron microscopy	TEM
transition metal	TM
trimethylaluminum	$AlMe_3$
trimethylaluminum	TMA
turnover frequency	TOF
Turnover number	TON
versus	vs.
wavelength	λ
wet impregnation	WI
x-ray absorption near edge spectra	XANES
X-ray absorption spectroscopy	XAS
X-ray Diffraction	XRD
X-ray emission spectroscopy	XES
X-ray photoelectron spectroscopy	XPS
zeolitic imidazolate framework-8	ZIF-8

LISTE DES PUBLICATIONS

21 Peer-reviewed articles published (6 first-author articles):

[1] **Zhangsen Chen**, G. Zhang, S. Cao, G. Chen, C. Li, R. Izquierdo, S. Sun, Advanced semiconductor catalyst designs for the photocatalytic reduction of CO_2, *Materials Reports: Energy*, 2023, 100193.

[2] **Zhangsen Chen**, G. Zhang, Q. Hu, Y. Zheng, S. Cao, G. Chen, C. Li, T. Boyko, N. Chen, W. Chen, T. Regier, J. Dynes, J. Wang, H. Wang, J. Zhou, S. Sun. The Deep Understanding into the Promoted Carbon Dioxide Electroreduction of ZIF-8-Derived Single-Atom Catalysts by the Simple Grinding Process. *Small Structures*, 2022, 3: 2200031.

[3] **Zhangsen Chen**, Gaixia Zhang, H. Chen, J. Prakash, Y. Zheng, S. Sun. Multi-metallic catalysts for the electroreduction of CO_2: Recent advances and perspectives*. Renewable & Sustainable Energy Reviews*, 2022, 155, 111922.

[4] **Zhangsen Chen**, G. Zhang, Y. Wen, N. Chen, W. Chen, T. Regier, J. Dynes, Y. Zheng, S. Sun. Atomically dispersed Fe-Co bimetallic catalysts for the promoted electroreduction of carbon dioxide. *Nano-Micro Letters*, 2021, 14, 25.

[5] **Zhangsen Chen**, G. Zhang, L. Du, Y. Zheng, L. Sun, S. Sun. Nanostructured cobalt-based electrocatalysts for CO_2 reduction: Recent progress, challenges, and perspectives. *Small*, 2020, 16, e2004158.

[6] **Zhangsen Chen**, G. Zhang, J. Prakash, Y. Zheng, S. Sun. Rational Design of Novel Catalysts with Atomic Layer Deposition for the Reduction of Carbon Dioxide. *Advanced Energy Materials*, 2019, 9, 1900889.

[7] C. Li, W. Zhao, X. Lu, **Zhangsen Chen**, B. Han, X. Zhang, J. Chen, Y. Shao, J. Huo, Y. Zhu, Y. Deng, S. Sun, S. Liao. PtCoNi ternary intermetallic compounds anchored on Co, Ni and N co-doped mesoporous carbon: Synergetic effect between PtCoNi nanoparticles and doped mesoporous carbon promotes the catalytic activity. *Journal of Energy Chemistry*, 2023, 78, 340-349.

[8] Y. Luo, P. Wang, G. Zhang, S. Wu, **Zhangsen Chen**, H. Ranganathan, S. Sun, Z. Shi. Mn-Doped Nickel-Iron Phosphide Heterointerface Nanoflowers for Efficient Alkaline Freshwater/Seawater Splitting at High Current Densities. *Chemical Engineering Journal,* 2023, 454, 140061.

[9] J. Prakash, P. Kumar, N. Saxena, Z. Pu, **Zhangsen Chen**, A. Tyagi, G. Zhang and S. Sun. CdS based 3D nano/micro-architectures: formation mechanism, tailoring of visible light activities and emerging applications in photocatalytic H_2 production, CO_2 reduction and organic pollutant degradation. *Journal of Materials Chemistry A*, 2023,11, 10015-10064.

[10] Z. Pu, T. Liu, G. Zhang, **Zhangsen Chen**, D. Li, N. Chen, W. Chen, Z. Chen, S. Sun. General Synthesis of Transition-Metal-Based Carbon-Group Intermetallic Catalysts for Efficient Electrocatalytic Hydrogen Evolution in Wide pH Range. *Advanced Energy Materials*, 2022, 12, 2200293.

[11] P. Wang, Y. Luo, G. Zhang, **Zhangsen Chen**, H. Ranganathan, S. Sun, Z. Shi. Interface Engineering of NixSy@MnOxHy Nanorods to Efficiently Enhance Overall-Water-Splitting Activity and Stability. *Nano-Micro Lett.,* 2022, 14, 120.

[12] P. Wang, Y. Luo, G. Zhang, M. Wu, **Zhangsen Chen**, S. Sun, Z. Shi. MnOx-Decorated Nickel-Iron Phosphides Nanosheets: Interface Modifications for Robust Overall Water Splitting at Ultra-High Current Densities. *Small*, 2022, 18, 7, 2105803.

[13] X. Zhan, X. Tong, M. Gu, J. Tian, Z. Gao, L. Ma, Y. Xie, **Zhangsen Chen**, H. Ranganathan, G. Zhang and S. Sun. Phosphorus-Doped Graphene Electrocatalysts for Oxygen Reduction Reaction. *Nanomaterials,* 2022, 12, 7, 1141.

[14] Samriti, Manisha, **Zhangsen Chen**, S. Sun and J. Prakash. Design and engineering of graphene nanostructures as independent solar-driven photocatalysts for emerging applications in field of energy and environment. *Mol. Syst. Des. Eng.*, 2022, 7, 213-238.

[15] F. Dong, M. Wu, **Zhangsen Chen**, X. Liu, G. Zhang, J. Qiao, S. Sun. Atomically Dispersed Transition Metal-Nitrogen-Carbon Bifunctional Oxygen Electrocatalysts for Zinc-air Batteries: Recent Advances and Future Perspectives. *Nano-micro Letters*. 2021, 14, 36.

[16] H. Zhang, L.V. Besteiro, J. Liu, C. Wang, G.S. Selopal, **Zhangsen Chen**, D. Barba, Z.M. Wang, H. Zhao, G.P. Lopinski, S. Sun, F. Rosei, Efficient and stable photoelectrochemical hydrogen generation using optimized colloidal heterostructured quantum dots, *Nano Energy*, 2021, 79, 105416.

[17] S. Vallières, M. Salvadori, A. Permogorov, G. Cantono, K. Svendsen, **Zhangsen Chen**, S. Sun, F. Consoli, E. d'Humières, C.-G. Wahlström & P. Antici. Enhanced laser-driven proton acceleration using nanowire targets. *Scientific Reports*, 2021, 11, 2226.

[18] K. Burdonov, A. Fazzini, V. Lelasseux, J. Albrecht, P. Antici, Y. Ayoul, D. Cavanna, T. Ceccotti, M. Chabanis, S.N. Chen, **Zhangsen Chen**, S. Sun, J. Fuchs, et al. Characterization and performance of the Apollon Short-Focal-Area facility following its commissioning at 1 PW level. *Matter and Radiation at Extremes*., 2021, 6, 064402.

[19] J. Zhang, G. Zhang, **Zhangsen Chen**, H. Dai, Q. Hu, S. Liao, S. Sun. Emerging applications of atomic layer deposition for lithium-sulfur and sodium-sulfur batteries. *Energy Storage Materials*, 2020, 26, 513.

[20] X. Tong, X. Zhan, D. Rawach, **Zhangsen Chen**, G. Zhang, S. Sun, Low-dimensional catalysts for oxygen reduction reaction, *Progress in Natural Science: Materials International*, 2020, 30, 787.

[21] X. Yang, G. Zhang, J. Prakash, **Zhangsen Chen**, M. Gauthier, S. Sun, Chemical vapour deposition of graphene: layer control, the transfer process, characterisation, and related applications. *International Reviews in Physical Chemistry.* 2019, 38, 149.

Manuscript in preparation:

[1] **Zhangsen Chen**, G. Zhang, H. Lei, S. Sun. The iron single-atom catalysts with the atomic layer deposition modification for the enhanced carbon dioxide electroreduction (To be submitted).

Book chapter:

[1]. **Zhangsen Chen**, S. Sun, G. Zhang. “Hybrid semiconductor photocatalyst nanomaterials in CO_2 reduction and storage applications“ in the book of Multifunctional hybrid semiconductor photocatalyst nanomaterials in health, energy, and environment. Prakash J, Cho J, Janegitz BC, Sun S. Springer, 2023.

1 Chapter 1 Introduction

1.1 The motivation and the CO_2 reduction reaction

The continuous release of CO_2 from anthropogenic activities, predominantly from fossil fuels consumption, has led to the mixed ratio of CO_2 in the atmosphere over 410 parts per million (ppm), which is approximately 50 % higher than that of the pre-industrial level (280 ppm). The increase rate of anthropogenic CO_2 emission rocketed in the last two decades from 1.1 % to 2.5-2.7 % per annum. (Lewis, 2016) The rapid increase of CO_2 emissions and energy shortage crisis caused by the considerable consumption of fossil fuels are great concerns for the environment. The consequent climate change (the average temperature increase of 0.8 ℃ above the pre-industrial level) causes global warming, one of the top environmental concerns.(Panzone *et al.*, 2020) It leads to numerous natural catastrophes that jeopardize human society. Terrestrial ecosystems remove only around 30 % of the anthropogenic CO_2 each year, which is not sufficient to keep the carbon balance.(Terrer *et al.*, 2021) To maintain the sustainable development of society, the Intergovernmental Panel on Climate Change (IPCC) recently recommended the warming limit to 1.5 ℃ rather than 2.0 ℃ to reduce catastrophic climate change issues, requiring the commitment to take action to control global carbon emissions. (Zhang *et al.*, 2020b) Under the Paris Agreement, many countries endeavor to reduce greenhouse gas emissions gradually by 2030. (McNutt, 2015) Therefore, the apparent incongruity between the rocketing consumption of fossil fuels and the sustainable development of our society has stimulated considerable research impetus to alleviate the current energy and environmental stress. (Yuan *et al.*, 2015) The methods of the reduction of CO_2, including carbon capture and storage (CCS) and CO_2 conversion, have attracted tremendous interest. CCS has been considered a feasible strategy to lower CO_2 emissions substantially from the consumption of fossil fuels. However, the lack of economic incentives and the long-term-storage issues related to the leakage of CO_2 restrain the development. (Chen *et al.*, 2018) The CO_2 conversion reactions which could convert CO_2 into other value-added carbon products could provide a well alternative to meet the requirements, which not only contributes to the mitigation of CO_2 emission, but also provides useful products that can be applied as fuels such as CO, CH_4, and CH_3OH.(He *et al.*, 2015; Varghese *et al.*, 2009; Wei *et al.*, 2017) Even though large thermodynamic and kinetic barriers exist for the reduction of the stable CO_2 molecules into other carbon products,(Schneider *et al.*, 2012) when suitable techniques are applied, for instance, by the development of new catalytic approaches or the

design of the new catalyst nanomaterials, both the environmental and energy issues could be solved simultaneously.

In the CO_2 reduction reactions, single electron reduction of CO_2 to $CO_2^{\bullet-}$ is extremely unfavorable due to a large reorganizational energy between the linear molecule CO_2 and the bent radical anion $CO_2^{\bullet-}$. However, the steps of the proton-assisted multi-electron reduction are much more favorable as shown in **Equations 1.1-1.5, 1.7-1.13** (at pH 7 in aqueous solution vs. Normal Hydrogen Electrode (NHE)).(Benson *et al.*, 2009; Fujita, 1999; Schneider *et al.*, 2012) Besides, there are various reduction products of CO_2RR, which demand complex reaction paths (**Figure 1.1a**). (Chen *et al.*, 2019) Aqueous media with H_2O molecules become promising for providing proton into the CO_2RR system. Theoretically, any provided potential that is more negative than the redox potentials of the CO_2 reduction reactions can drive the reaction. The reduction potential of HER (**Equation 1.13**) is close to that of CO_2RR. It makes HER a competitive reaction against CO_2RR during the reduction progress because of its relative facility compared with CO_2RR, significantly decreasing the FE of the target product.

$$CO_2 + e^- \rightarrow CO_2^{\bullet-} \qquad E = -1.90V \qquad 1.1$$

$$2CO_2 + 2H^+ + 2e^- \rightarrow H_2C_2O_4 \qquad E = -0.91\,V \qquad 1.2$$

$$CO_2 + 2H^+ + 2e^- \rightarrow HCO_2H \qquad E = -0.61V \qquad 1.3$$

$$CO_2 + 2H^+ + 2e^- \rightarrow CO + H_2O \qquad E = -0.53V \qquad 1.4$$

$$CO_2 + 4H^+ + 4e^- \rightarrow HCHO + H_2O \qquad E = -0.48V \qquad 1.5$$

$$2H^+ + 2e^- \rightarrow H_2 \qquad E = -0.42\,V \qquad 1.6$$

$$CO_2 + 6H^+ + 6e^- \rightarrow CH_3OH + H_2O \qquad E = -0.38V \qquad 1.7$$

$$2CO_2 + 12H^+ + 12e^- \rightarrow C_2H_4 + 4H_2O \qquad E = -0.35\,V \qquad 1.8$$

$$2CO_2 + 12H^+ + 12e^- \rightarrow C_2H_5OH + 3H_2O \qquad E = -0.33\,V \qquad 1.9$$

$$3CO_2 + 18H^+ + 18e^- \rightarrow C_3H_7OH + 5H_2O \qquad E = -0.31\,V \qquad 1.10$$

$$2CO_2 + 14H^+ + 14e^- \rightarrow C_2H_6 + 4H_2O \qquad E = -0.27\,V \qquad 1.11$$

$$CO_2 + 8H^+ + 8e^- \rightarrow CH_4 + 2H_2O \qquad E = -0.24V \qquad 1.12$$

$$CO_2 + 4H^+ + 4e^- \rightarrow C + 2H_2O \qquad E = -0.20V \qquad 1.13$$

To reduce CO_2 to the value-added products successfully as shown in **Equation 1.2-1.7**, the technique of catalysis that can accelerate the rate of the chemical reactions would be promising

and economically suitable. Several methods, including the traditional thermochemical reduction,(Bhosale *et al.*, 2016) the photocatalytic reduction,(Fang *et al.*, 2014; Liu *et al.*, 2015; Pan *et al.*, 2017) the electrochemical reduction,(Dai *et al.*, 2017; Hod *et al.*, 2015; Liu *et al.*, 2016) and the photoelectrocatalytic (PEC) reduction,(Inoue *et al.*, 1979; Magesh *et al.*, 2014) methods have been reported for the reduction of CO_2. However, the high performance of the CO_2 reduction reaction has not been reached. The key to the catalytic process is the highly efficient and stable catalyst materials for CO_2 reduction. Considerable research has been carried out to develop catalyst materials for the reduction of CO_2.(Dinh *et al.*, 2018; Guo *et al.*, 2017; Meng *et al.*, 2014; Niu *et al.*, 2017; Stiebritz *et al.*, 2018) For example, Meng et al. prepared Rh/Al_2O_3 as the catalyst for the photo-thermal hydrogenation of CO_2 into CH_4. (Meng *et al.*, 2014) Niu et al. synthesized a spongy nickel-organic heterogeneous photocatalyst for the conversion of CO_2 to CO.(Niu *et al.*, 2017) Kang et al. introduced a Co_3O_4-CDots-C_3N_4 three-component electrocatalyst to achieve an efficient, stable, cheap and selective route for the syngas production. (Guo *et al.*, 2017) Dinh et al. designed a copper-assisted electrode that had great toleration towards the base. By optimizing the diffusion of CO_2 to the catalytic sites, the design of the copper catalyst was able to reduce CO_2 into ethylene. (Dinh *et al.*, 2018) Nevertheless, the challenges remain to the development of suitable technology and the design of highly efficient catalyst materials to catalyze the CO_2 reduction reactions in a mild condition with high-performance activity, selectivity, and long-term stability.

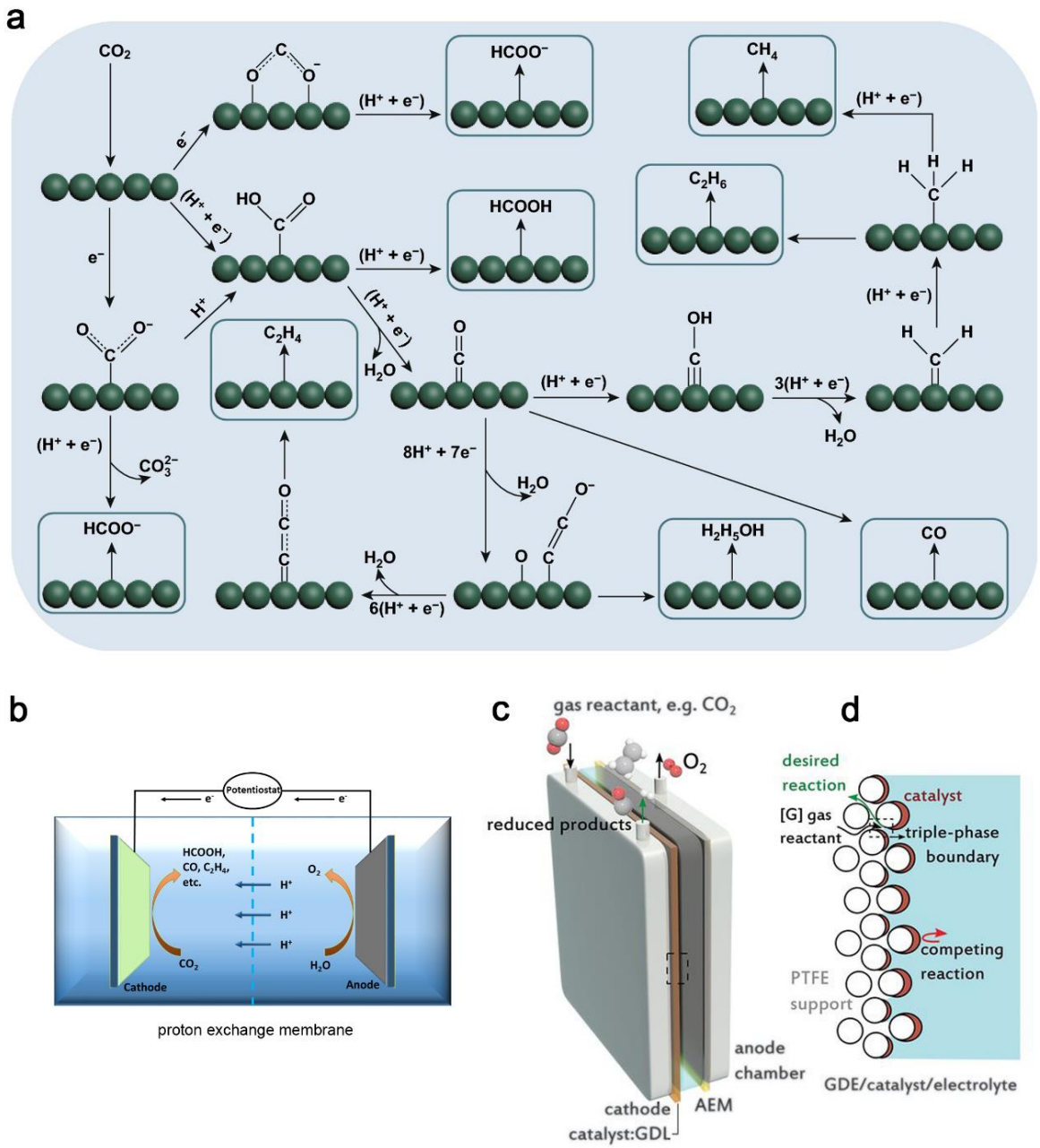

Figure 1.1 (a) Potential CO_2RR pathways to produce HCOOH, CO, CH_4, C_2H_6, C_2H_4, and C_2H_5OH. (b) The schematic of ECO_2RR. (c) The schematic of the flow cell. (d) The illustration of a gas diffusion electrode (GDE). Reprinted with permission from ref. (Chen et al., 2022)

1.2 The electroreduction of CO_2

ECO_2RR is more efficient because it can apply external cathodic overpotential under relatively mild conditions. There are several advantages of the CO_2 reduction by the approach of electrochemical catalysis: (1) the reduction process is controllable by electrode potentials; (2) the overall chemical consumption could be minimized to only water because the supporting

electrolytes could be fully recycled; (3) renewable energy sources such as solar, wind, hydroelectric, geothermal, tidal, and thermoelectric processes could provide the electricity to drive the electrocatalytic process. In addition, these energy sources can be tailored not to produce any extra CO_2; (4) the electrochemical reaction systems are compact, modular, on-demand, and feasible for scale-up applications. (Agarwal *et al.*, 2011; Jhong *et al.*, 2013; Qiao *et al.*, 2014) In the schematic for the electrocatalytic reduction of CO_2 (**Figure 1.1b**), an external voltage is supplied to the cathode and the anode for the reduction of CO_2 and the oxidation of water (OER), respectively. A proton exchange membrane that separates the sides of the cathode and the anode avoids the mixture of the products from the reduction and the oxidation reactions. Two compartments could be individually optimized and combined to reach a better overall performance. The major side reaction of the electrochemical reduction of CO_2 is the HER which competes with the reduction of CO_2 and produces H_2 as the byproduct.

To get a desirable outcome of the electrochemical reduction of CO_2, the preparation of efficient electrocatalysts that can accelerate the reaction rate and improve the selectivity of the products is required. (Wu *et al.*, 2017) The main efforts of improving the electrocatalytic performance of the reduction of CO_2 have been put on several aspects, including the increase of the current density, the selectivity, and the long-term stability, and the lowering of the overpotentials of the reduction products.(Han *et al.*, 2018; Wen *et al.*, 2018; Zhang *et al.*, 2018a; Zhang *et al.*, 2018b; Zhang *et al.*, 2018d; Zhao *et al.*, 2018a)

1.3 CO and syngas (CO + H_2) production from ECO_2RR

When it comes to the commercial viability of CO_2RR products, it turns out that two-electron products of CO and HCOOH are more desirable than C_{2+} products like ethanol, ethylene, n-propanol, and acetate. Although C_{2+} products are intuitively more valuable than CO and HCOOH, they have a considerably lower added value per kWh of electrical energy input, making CO and HCOOH the most economically viable for ECO_2RR (**Figure 1.2a**, normalized price). (Han *et al.*, 2019) In CO_2RR, formate is usually the reduction product that is mixed in the reaction solution. The subsequent separation and purification procedures are required to produce the final product HCOOH, which is not cost-efficient and time-consuming. On the contrary, gaseous product CO is already separated from the aqueous reaction solution during the CO_2RR process. Besides, it could be the reagent to produce hydrocarbons by industrial approaches. (Lu *et al.*, 2015; Park *et al.*, 2017; Sun *et al.*, 2017) As aforementioned, H_2 is a common by-product in CO_2RR. Mixed with

CO, the syngas (gas mixture of CO and H_2) that is widely employed in Fischer−Tropsch applications has attracted considerable attention in CO_2RR (Chen *et al.*, 2020c).

CO or syngas produced from ECO_2RR can be applied as feedstock in established industrial processes (e.g. Fischer−Tropsch synthesis) for the production of various important chemicals, such as long-chain hydrocarbons, methanol, higher alcohols, and fuels (Andrei *et al.*, 2019; Kang *et al.*, 2020; Zhang *et al.*, 2020a). CO and syngas production from ECO_2RR could contribute to the conception of completing the carbon loop, which could benefit the sustainable development of human society. The direct ECO_2RR production of syngas with different H_2/CO ratios could be highly desirable for various downstream products in Fischer−Tropsch synthesis and other thermochemical processes, compared to the traditional industrial methods (e.g. reforming of natural gas and coal, the water gas shift reaction), which demand relatively harsh reaction conditions at high-cost (Wang *et al.*, 2020b; Zhou *et al.*, 2019b). Under this circumstance, syngas produced from ECO_2RR requires mild reaction condition appeals. Besides, by tuning the applied potential, the ratio of CO/H_2 can also be adjusted in ECO_2RR. (He *et al.*, 2019). The CO/H_2 ratio decides the final downstream product from Fischer−Tropsch synthesis. (Ross *et al.*, 2019) It increases the competency of ECO_2RR in the syngas production industry.

1.4 Practical apparatus of ECO_2RR

1.4.1 H-cell

H-cell (**Figure 1.1b**) is the most commonly used electrolysis reactor for ECO_2RR, consisting of two electrode compartments. An ion exchange membrane separates the cathode and anode to avoid the crossover of products on each side and facilitate the separation. This type of reactor requires the dissolution of CO_2 gas in the electrolyte. Low solubility and slow diffusion restrain the current density of ECO_2RR at a low level (usually < 50 mA cm^{-2}).

1.4.2 Flow-cell

Inspired by the configurations of fuel cells that can successfully manage gaseous reactants, an analogous flow cell system **(Figure 1.1c)** is an alternative to enhance the reaction rate and productivity. (Dinh *et al.*, 2018; Zhang *et al.*, 2019b) The most significant difference between the flow cell and H-cell is that the CO_2 can supply the flow cell without dissolving in the electrolyte. By using the gas diffusion electrode (GDE, **Figure 1.1d**), the catalyst can directly react with the gaseous CO_2 molecule. It allows the flow cell system to suffer less mass-transport issues

compared with the bath type system (H-cell), providing higher current densities to the industrial relevant level (up to ampere level) in ECO_2RR.(Ma *et al.*, 2020; Zheng *et al.*, 2018)

1.4.3 Products characterization by GC, IC, and NMR

CO_2RR has a variety of reduction products with a competitive reduction product of H_2. It is significant to evaluate the real yield of the products during the catalysis accurately by advanced analytical techniques. Gas chromatography (GC) can analyze gas products, while ion chromatography (IC) and nuclear magnetic resonance (NMR) merit liquid product analysis. All these analytic techniques provide the accurate quantification and qualification of the reduction products that are essential for analyzing the catalytic performance of ECO_2RR.

1.5 Performance merits of ECO_2RR

1.5.1 Onset potential and overpotential

As illustrated in **Equation 1.1-1.13**, different reduction potentials are required to obtain different reduction products for CO_2RR. Experimentally, researchers tend to define the onset potential as the potential where the products of ECO_2RR can be firstly detectable. (Lou, 2019; Zu *et al.*, 2019) The overpotential is the difference between the actual reduction potential applied to the electrode and the thermodynamic equilibrium electrode potential. Although the target product starts to generate at the onset potential, the product yield might be meager. It requires a more negative potential than the onset potential to reach a higher product yield which refers to the current density in ECO_2RR. A desirable catalyst should have an onset potential that is close to the thermodynamic equilibrium potential and a low overpotential to produce a relatively high current density.

1.5.2 Current density

Current density reflects the number of charges that are concerning the reactions during the electrochemical catalysis, indicating the rate of the reaction.(Kibria *et al.*, 2019) Different standards such as the geometric area, the electrochemical surface area (ECSA) of the electrode, and the mass loading of the catalyst can normalize the current density. When performing the electrochemical experiments, the electrochemical workstation initially provides the data of the total current density. The total current density consists of the contribution of all the reduction reactions. In ECO_2RR, combined with FE, one can measure the partial current density corresponding to the specific reduction product.

1.5.3 Faradaic efficiency

During CO_2RR, there are many possible products, along with the competitive reaction of HER. The proportion of the target reduction products in the final products is always the top concern. In ECO_2RR, FE is the parameter to determine the product selectivity of the catalysts. While reaching a high current density, a high FE of the target reduction product is necessary as well. To calculate the FE, we follow a basic **equation 1.14**:

$$FE_i = \frac{Q_i}{Q_{total}} \qquad 1.14$$

Where i represents the target reduction products (such as CO, HCOOH, H_2); Q_i represents the charges used to produce specific reduction products; Q_{total} represents the total charges that the whole process consumed.

1.5.4 Turnover number and turnover frequency

Turnover number (TON) and turnover frequency (TOF) can evaluate the reaction rate at a specific applied potential concerning the real catalyst and the number of active sites, respectively. **Equation 1.15** calculates TON:

$$\mathrm{TON} = \frac{Q_{total} \times FE_i}{nF \times t} \qquad 1.15$$

Where n is the number of electrons needed for the reaction pathway; F is the Faraday constant (96485.3 C mol^{-1}); t is the reaction time; Unit is t^{-1}.

TOF can be calculated based on **equation 1.16**: (Yang *et al.*, 2018)

$$\mathrm{TOF} = \frac{TON\ for\ the\ specific\ reduction\ product}{Number\ of\ the\ active\ sites} \qquad 1.16$$

TOF and TON share the same unit. However, when calculating the number of active sites for the electrode, it is usually a fuzzy estimation. Researchers tend to estimate the number of active sites approximately by assuming that all the surficial atoms of an active material contribute to the target reaction, which leads to inaccuracy. Although there are difficulties in evaluating the real active site number, TOF can still be used to reflect the actual kinetics of the reactions, providing insights into the relationship between the active sites and the reaction rate.

1.5.5 Stability

After the high Faradaic efficiency and current density have been achieved, long-term stability is another critical factor to evaluate the catalysts for the commercially relevant electrolysis. So far, the catalytic stabilities for the two-electron path products (CO and HCOOH) are the highest among all the ECO_2RR products. The best stability known that produces CO with FE over 90% at current densities of 200 mA cm^{-2} is 1000 hours. (Kutz *et al.*, 2017) For the HCOOH production, the stability for the high activity (FE of around 97%, current densities of about 450 mA cm^{-2}) is 100 hours.(Fan *et al.*, 2020; Xia *et al.*, 2019) For the Cu-based catalysts producing multiple C^{2+} products, the stabilities for a specific product with FE of around 60% are from dozens of hours to 100 hours. (Garcia de Arquer *et al.*, 2020; Leow *et al.*, 2020) Most of the catalysts have long-term stability with high Faradaic efficiency of around dozens of hours, which is inadequate for industrial application.(Cheng *et al.*, 2020; Jiang *et al.*, 2020)

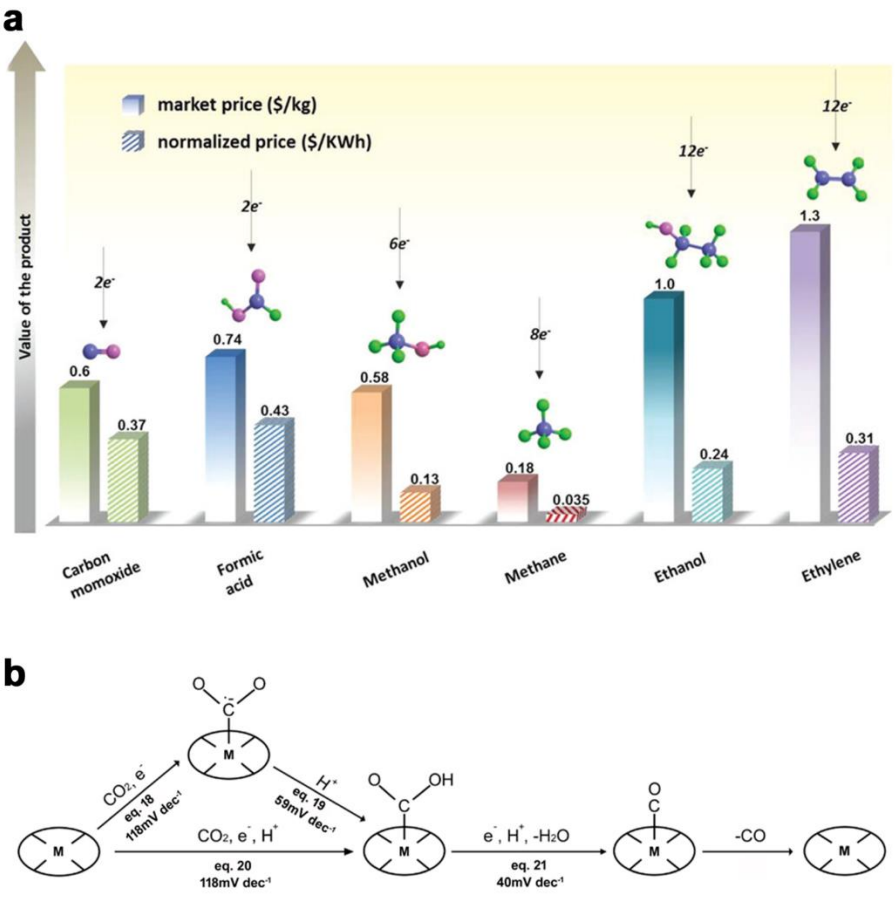

Figure 1.2 (a) Comparison of the values of different CO_2RR products in terms of their market prices ($ kg−1) and added values per kWh electrical energy input ($ kWh−1) estimated based on ideal full cells. (b) Proposed reaction pathways of CO_2 electroreduction to CO on the metal site. Reprinted with permission from ref. (Chen et al., 2020c)

1.5.6 Tafel slope

Tafel slope is usually involved in the kinetic and mechanistic analysis for electrochemical reactions. **Equation 1.17** shows the Tafel equation: (Burstein, 2005)

$$\mathrm{E} = \mathrm{a} + \mathrm{b}\log j \qquad 1.17$$

Where *E* is the potential (overpotential), and *j* is the absolute value of the current density.

With the proper correction, the Tafel slope (b) can be obtained from the plot of E versus $\log j$. A smaller Tafel slope indicates a similar potential change could drive a more considerable current increase, which is one of the parameters to identify a suitable catalyst through a simple comparison of Tafel slope values between catalysts. (Zhou *et al.*, 2019a)

Most importantly, the Tafel slope can elaborate on the reaction pathways for the mechanistic analysis of ECO_2RR.(Wuttig *et al.*, 2017) For example, *COOH is usually considered as the intermediate to form CO during ECO_2RR. **Figure 1.2b** shows the proposed reaction pathways of CO_2 electroreduction to CO on the metal site. The formation of *COOH intermediate can go through either decoupled (**Equation 1.18** + **Equation 1.19**) or coupled (**Equation 1.20**) electron-proton transfer pathway.

$$CO_2 + e^- \rightarrow CO_2^{\cdot -} \qquad 1.18$$

$$CO_2^{\cdot -} + H^+ \rightarrow *COOH \qquad 1.19$$

$$CO_2 + e^- + H^+ \rightarrow *COOH \qquad 1.20$$

$$*COOH + e^- + H^+ - H_2O \rightarrow *CO \qquad 1.21$$

In this case, a Tafel slope value of around 118 mV dec^{-1} indicates the rate-determining step is either the first step of the proton-decoupled electron transfer (**Equation 1.18**, **Figure 1.2b**) or the direct-coupled electron-proton transfer (**Equation 1.20**, **Figure 1.2b**). A Tafel slope value of around 59 mV dec^{-1} would suggest the rate-determining step is the second step of the proton-decoupled electron transfer (**Equation 1.19**) for *COOH formation. A Tafel slope value of around 40 mV dec^{-1} suggests that the rate-determining step is the formation of *CO (**Equation 1.21**, **Figure 1.2b**) that is following the *COOH formation during ECO_2RR to CO. (Gu *et al.*, 2019)

Briefly, merits like onset potential, current density, FE, and turnover number are meant to determine the catalytic activity of the catalyst materials. Stability is an essential parameter for future industrial applications. Tafel slope can be used to compare the excellence within a series

of catalysts and analyze the reaction mechanism of ECO_2RR. Among them, FE, current density, and stability are of the most interest in the ECO_2RR catalyst design.

1.6 Metal catalysts for the efficient ECO_2RR

To obtain a ECO_2RR catalyst with desirable FE, current density, and stability, the rational design of catalysts is required. Current ECO_2RR catalysts cover various materials, and metal-based has attracted significant attentions. Precious metals such as Ag, Au, and Pd demonstrate outstanding ECO_2RR activity for CO production.(Chen *et al.*, 2020a; Shi *et al.*, 2020; Sun *et al.*, 2020) The rare-earth metal materials such as Er, Sc, and Y also show promising catalytic performance towards ECO_2RR because of their unique electronic properties. Due to the vulnerability of the supply markets, current strategies of CO_2RR catalyst design for precious and rare-earth metal materials mainly focus on the improvement of metal-utilization.(Cheng *et al.*, 2015; Ji *et al.*, 2020; Liu *et al.*, 2020a) While the rarity limits the application of precious and rare-earth metal materials, the exploration of earth-abundant metal materials in ECO_2RR is booming. For example, main-group metals such as Bi, In, Sb, and Sn are efficient for ECO_2RR towards formate production. (Jiang *et al.*, 2020) Transition metals such as Fe, Co, Ni, Cu, and Zn become the most popular elements studied in ECO_2RR for the high FE, current density, and selectivity of numerous products. (Geng *et al.*, 2018; Sun, 2019; Wang *et al.*, 2019b; Yang *et al.*, 2020a; Yang *et al.*, 2020b) Cu is the only monometallic element that has been confirmed to be able to produce various C_{2+} products (e.g. hydrocarbons and alcohols) in CO_2RR by tuning the valence of Cu, catalyst structures, and exposed facets, etc. (De Gregorio *et al.*, 2020; Gao *et al.*, 2020; Ma *et al.*, 2020; Vasileff *et al.*, 2018; Wang *et al.*, 2019b) And non-Cu transition metals (e.g. Ni, Fe, Co) mostly promote the production of CO.

1.6.1 Co-based catalysts for the CO production in ECO_2RR

Among metal electrocatalysts, Co-based catalysts are strikingly efficient for the production of CO and HCOOH in ECO_2RR. Ren et al. utilized the old fashion CoPc in the new flow cell system, achieving a reaction rate comparable to the industrial level of CO by the ECO_2RR. (Ren *et al.*, 2019a) Xie's group synthesized the Co_3O_4 nanosheet catalysts with the thickness at the atomic level, which were very active for the formate production.(Gao *et al.*, 2016a; Gao *et al.*, 2016b) Although rarely reported, Co-based electrocatalysts could also produce other CO_2RR products. For example, Wu et al. immobilized the CoPc on CNT to drive a distinct domino process of ECO_2RR that could produce methanol. (Wu *et al.*, 2019) The ability to produce CO and HCOOH

from ECO_2RR makes Co-based catalysts very competitive in future industrial applications. According to the statistic **(Figure 1.3)**, CO is the most typical reduction product using Co-based catalysts for ECO_2RR. As aforementioned, CO is one of the most cost-effective products from CO_2RR because it holds high commercial viability for industrial production, and it could be the reagent to produce hydrocarbons by industrial approaches such as the Fisher-Tropsch method.(Lu *et al.*, 2015; Park *et al.*, 2017; Sun *et al.*, 2017) Zhang et al. chose MPcs (M = Mn, Fe, Co, Ni, and Cu) as the model catalysts for systematic DFT calculations to investigate the reaction pathways of CO_2RR and found out that the moderate *CO binding energy at the Co site promoted the overall reaction thermodynamics by compromising the critical reaction steps of the *COOH formation and the *CO desorption. (Zhang *et al.*, 2018e) It demonstrates that Co-based catalysts are great candidates for CO production from CO_2RR.

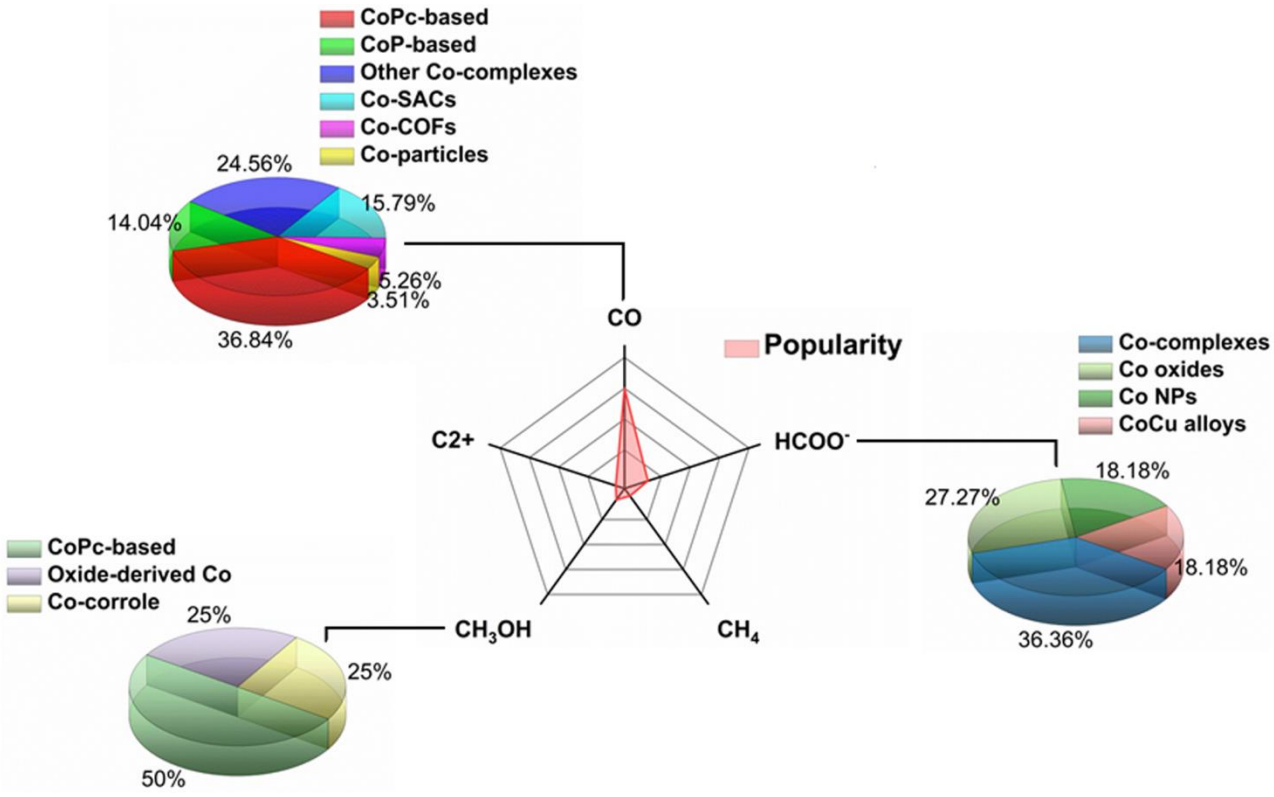

Figure 1.3 The product distribution and catalyst types of Co-based catalysts for ECO_2RR. Reprinted with permission from ref. (Chen et al., 2020c)

1.6.2 Single-atom catalysts for the highly efficient active sites in ECO_2RR

Traditional heterogeneous catalysts with a broad size distribution of metal particles suffer from a low metal utilization efficiency and poor selectivity. Recently, catalyst materials with atomic-level

precision (e.g. SACs and atomically-dispersed catalysts) have attracted significant attention because of the maximized utilization of active catalytic sites and the promising performance of catalytic reactions. (Hulva *et al.*, 2021; Vijay *et al.*, 2020) SACs are usually metal-supported catalysts where isolated monometallic moieties (single-metal-atom and the neighboring atoms of the support) are evenly dispersed on the surface, which provides well-defined active sites during catalysis. (Jeong *et al.*, 2020) As illustrated in **Figure 1.4**, the size reduction causes the increase of the surface free energy of the metal species. In the extreme case of single-atom catalysts, the surface free energy of metal species reaches a maximum due to the highly active valence electrons, the quantum confinement of electrons, and the sparse quantum level of metal atoms. (Yang *et al.*, 2013) The flexibility in modifying the local environment of the active sites in SACs offers the possibility to improve the catalytic performance of the ECO_2RR. (Ni *et al.*, 2021) Atomically dispersed metal ions can be easily introduced in the metal nodes, organic ligands, or pores of MOFs because of their unique characteristics, including organic-inorganic hybrid nature, large surface area, well-defined porosity, tunable chemical composition, and adjustable functionality. (Liu *et al.*, 2017) In the meantime, the high metal utilization ratio of SACs would attribute to the design of cost-efficient catalysts for future industrialization. (Zuo *et al.*, 2021)

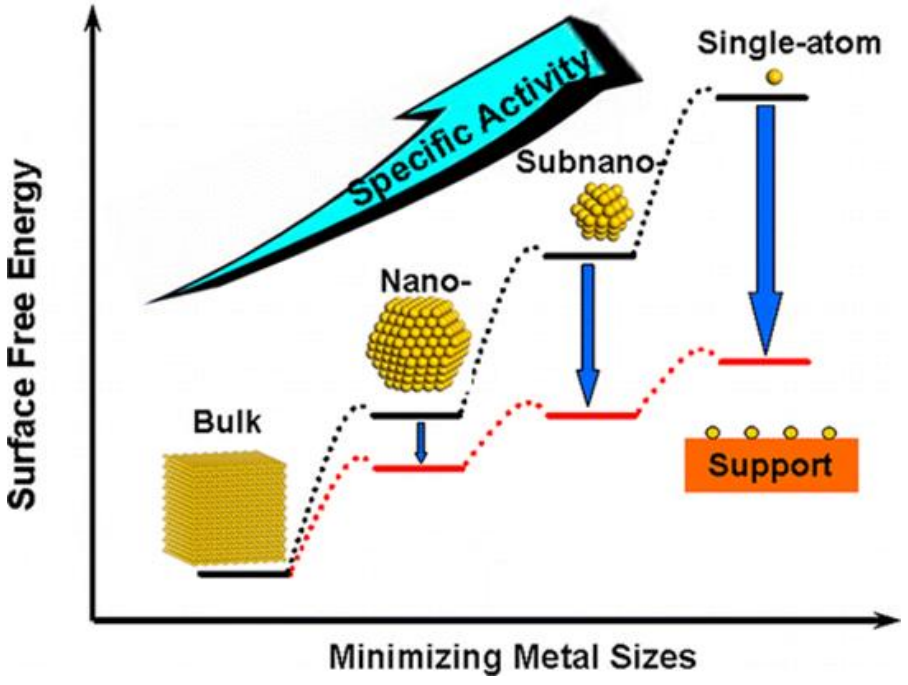

Figure 1.4 Schematic illustration of the changes of surface free energy and specific activity (catalytic activity corresponding to the specific reactions) per metal atom with metal particle size, and the support effects on stabilizing single atoms. Reprinted with permission from ref. (Yang et al., 2013)

Metal-organic frameworks (MOFs) are polymers with highly ordered crystalline coordination that is tunable for chemical modifications, which are desired for the construction of SACs. MOF-supported or MOF-derived catalysts usually provide well-defined active sites and the porous matrix. With efficient synthetic and modification strategies, MOF-supported or MOF-derived SACs could ensure high ECO_2RR performance and provide a fundamental understanding of the underlying mechanism. Besides, the Co-based SACs synthesis through the MOF-template approach has already been widely explored, which offers solid references for catalyst fabrication and active site structure prediction. (Wang *et al.*, 2018a)

1.6.3 Multi-metallic catalysts for the synergistic promotion in ECO_2RR

The integration of different metal atoms in one catalyst material (multi-metallic catalyst) sometimes renders better catalytic performance than that of the single metal element-based materials, which has been verified in many electrochemical catalytic reactions, e.g. ORR, (Luo *et al.*, 2019; Ricciardulli *et al.*, 2021; Zamora Zeledon *et al.*, 2021; Zhang *et al.*, 2019a) OER, (Liu *et al.*, 2021; Meng *et al.*, 2019; Qiao *et al.*, 2021; Wang *et al.*, 2018b) HER, (Zhao *et al.*, 2018b), etc. (Lv *et al.*, 2021; Ouyang *et al.*, 2021; Wu *et al.*, 2018; Zhu *et al.*, 2018) Multi-metallic catalysts have multiple active sites that could function in different directions during the ECO_2RR process promoting the specific product formations individually, thus improving the catalytic performance. (Shen *et al.*, 2020) The co-adsorption of the reaction intermediates (e.g. bridge-bonded *CO) on the adjacent active sites would facilitate the certain reaction pathway of the specific product formation. (Chang *et al.*, 2020; Zhang *et al.*, 2021b) For example, Wen et al. fabricated a 3D ordered mesoporous (3DOM) $Sn_{0.3}Ti_{0.7}O_2$ for ECO_2RR to CO and found out that the added Ti atoms not only tuned the orbital band center of Sn but also preferably adsorbed the oxygen atom in the intermediate of COOH*, favoring the selective production of CO. (Wen *et al.*, 2020) An Ag-Cu catalyst showed enhanced adsorption for bridge-bonded CO_2, which facilitated the formation of HCOOH from ECO_2RR. (Shan *et al.*, 2020) Besides, the binding energy of the reaction intermediates on the primary metal sites could be tuned by the introduction of the secondary metal, resulting in synergistic catalysis effects for ECO_2RR. (Lin *et al.*, 2019)

Benefiting from the advantages of SACs, atomically dispersed active sites in the multi-metallic catalysts, such as isolated diatomic site catalysts, stand out for their enhanced electronic and chemical properties. (Han *et al.*, 2021; Zhang *et al.*, 2021c; Zhou *et al.*, 2020a)

1.7 ALD for the CO_2RR catalyst modification

Many synthetic methods can fulfill the synthesis of the materials with atomic-level precision, including the wet impregnation (WI) method, modular synthetic approach, metal-organic complexes derived method, high-temperature atom trapping approach, and ALD method. (Zhang *et al.*, 2018c) ALD is one of the emerging and promising techniques with wide applications in the fields of energy and the environment such as catalysis, metal ion batteries, solar cells, and fuel cells.(Chao *et al.*, 2012; Jung *et al.*, 2013; Kot *et al.*, 2018; Lim *et al.*, 2003; Prakash *et al.*, 2018; Prakash *et al.*, 2014; Sun *et al.*, 2013; Switzer, 2012; Timm *et al.*, 2018; Zhang *et al.*, 2013a)

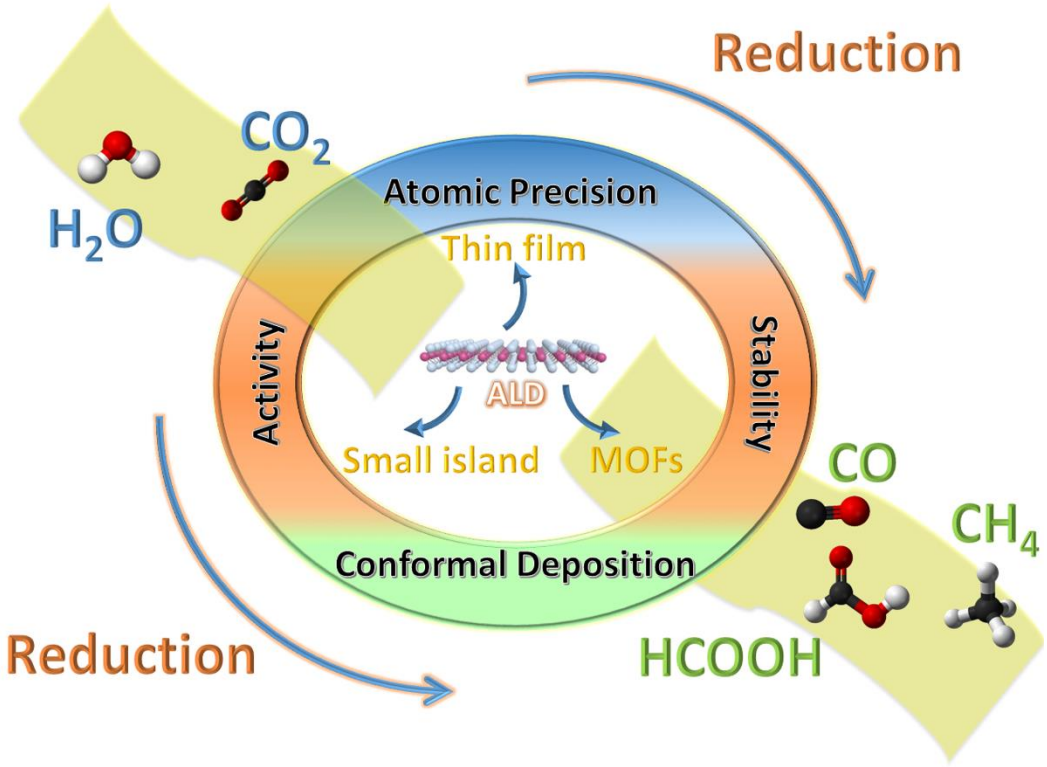

Figure 1.5 The overview of the ALD technique applied in the reduction of CO_2. Reprinted with permission from ref. (Chen et al., 2019)

ALD offers a unique deposition technology in nanomaterials synthesis with various advantages, including uniform and conformal deposition over the substrates and the accurate thickness control of the deposited material with atomic-level precision.(Meng *et al.*, 2011; Pan *et al.*, 2018a; Ritala, 2000) These advantages facilitate ALD to design subtle and complicated catalyst nanomaterials, such as ultrathin films, small islands, and nanoparticles, with efficient catalytic activities.(Meng *et*

al., 2010; Xie *et al.*, 2017) The ultra-thin coating layer deposited by ALD on the active catalyst nanomaterials provides additional strength, stability, and corrosion prevention to the nanomaterials while keeping their functionality. (Nardi *et al.*, 2015) Moreover, the ALD coating creates enough passivation on the surface states and allows the charge transferring through the coating layers to react with the reactants on the surface of the catalysts without affecting the reaction mechanism and the process of the catalysis.(Hwang *et al.*, 2012; Li *et al.*, 2009)

For the reduction of CO_2, the ALD-based nanomaterial catalyst design is also very promising (Kim *et al.*, 2016). ALD can design efficient catalysts in a highly controllable manner, which could be applicable to address the aforementioned key issues in the reduction of CO_2 **(Figure 1.5)**.

1.7.1 The fundamentals of ALD

ALD is a cyclic process that relies on the sequential self-terminated surface reactions between the gas-phase precursor molecules and the solid substrate surface. It provides the conformal deposition of atomic layers with precise control of the thickness and the high aspect ratio.(Detavernier *et al.*, 2011; George, 2010) Generally, ALD is appropriate for the synthesis of binary compound films because the deposition reactions of the binary compounds can be easily divided into two half-reactions. (George *et al.*, 1996) For the ALD synthesis of the binary compound, the reagents of the two half-reactions are defined as precursor A and B, respectively. A simplified schematic for the ABAB type of the surface sequential self-terminating reaction by the ALD process is shown in **Figure 1.6**. While repeating the dosing and purging steps, each of the half-reactions takes place on the surface of the substrate. Before the following reaction starts, the residuals and the byproducts from the previous reaction are purged away by the carrier gas flow. Because the number of reactive sites on the substrate surface is finite, the reaction could limit itself once all the reactive sites on the surface are occupied, yielding a conformal monolayer on the surface for every cycle at the suitable synthetic condition. (Suntola, 1989) Hence, ALD can produce nanomaterials with atomic control of the layer growth, high aspect ratio, step coverage, and conformal deposition.

The ALD synthesis of Al_2O_3 by trimethylaluminum ($AlMe_3$) and water is a typical example to clarify the self-terminating reactions. (Puurunen, 2005) The synthesis of ALD-Al_2O_3 follows the $AlMe_3/H_2O$ process as shown in **Equation 1.22** (Me = methyl = CH_3).

$$Al(CH_3)_3(g) + \frac{3}{2}H_2O(g) \rightarrow \frac{1}{2}Al_2O_3(s) + 3CH_4(g) \quad 1.22$$

The chemistry of the $AlMe_3/H_2O$ process is often divided into two successive "half-reactions" as presented in **Equations 1.23 and 1.24**.

$$||Al - OH + Al(CH_3)_3(g) \rightarrow ||Al - O - Al(CH_3)_2 + CH_4(g) \quad 1.23$$

$$||Al - O - Al(CH_3)_2 + H_2O(g) \rightarrow ||Al - O - Al(OH)_2 + 2CH_4(g) \quad 1.24$$

The successive half reactions start with a hydroxyl group terminated substrate. While introducing the gaseous $AlMe_3$ molecules into the ALD reaction chamber in the first dosing step, $AlMe_3$ reacts with the hydrogen atoms of the OH groups on the substrate surface through the ligand exchange, forming O–Al bonds and releasing the gaseous methane as the byproduct **(Equation 1.23)**. Practically, for the OH groups on the silica and the alumina substrates, the matrix temperature should be at least between 80 and 300℃ for the ligand exchange reaction.(Puurunen *et al.*, 2001; Puurunen *et al.*, 2000) It is proposed that the oxygen atom of the hydroxyl group on the substrate surface first reacts with the $AlMe_3$ molecule by interacting with the empty p-orbital of the aluminum atom, followed by a sigma-bond metathesis to release the methane molecule. This ligand exchange reaction will automatically stop once the $AlMe_3$ molecules occupy all the active hydroxyl sites on the substrate surface. Because the groups of $–CH_3$ on the current surface will not react with the residual $AlMe_3$ molecules in the gas phase further, leaving a monolayer of the $AlMe_3$ molecules which are chemically adsorbed on the substrate surface. (Wang *et al.*, 2014) In the following purging step, the purging gas (inert gas) will purge the byproduct (methane) and the excessive precursor ($AlMe_3$) out of the reaction chamber. Then the dosing step of the oxidant follows. At this time, H_2O is introduced into the reaction chamber, hydrolyzing the groups of $–CH_3$ on the substrate surface, transforming the $–CH_3$ terminated surface back to the hydroxyl group terminated surface again on the substrate **(Equation 1.24)**. Following another purging step that purges away the excessive H_2O molecules and the byproduct, one monolayer of Al_2O_3 remains on the surface of the substrate, which completes one entire ALD cycle. By repeating a certain number of times of the ALD cycles, the thickness of the Al_2O_3 film can be controlled.

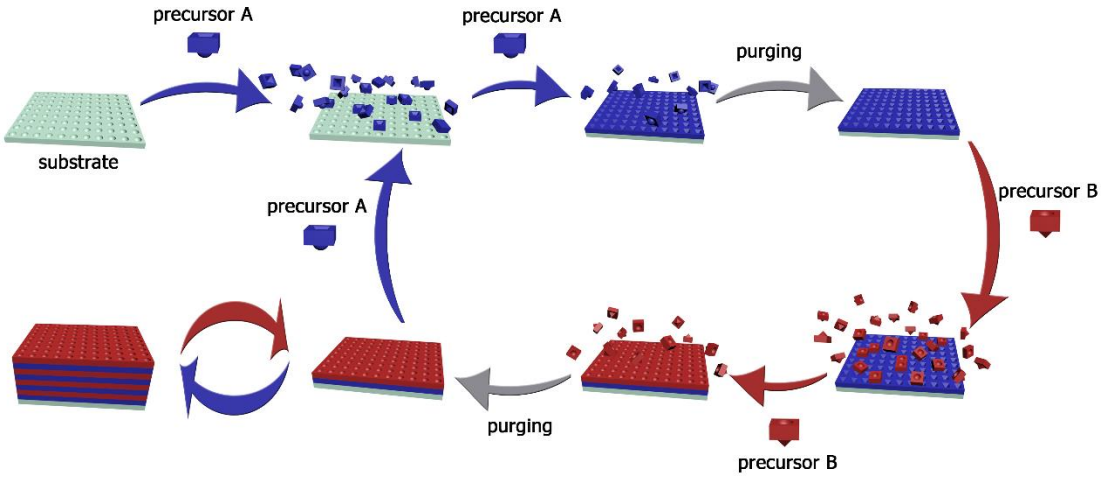

Figure 1.6 The schematic of the self-terminating surface mechanism of ALD by AB binary reaction sequence. Reprinted with permission from ref. (Chen et al., 2019)

The first experiment of ALD was reported in Finland in 1974 by Tuomo Suntola.(Suntola *et al.*, 1985) ZnS was selected as the target material for the production of electroluminescent devices, in which the ALD process was described as atomic layer epitaxy (ALE). In the 1990s, ALD was applied in the design of microelectronic nano-devices and successful commercial development started.(Detavernier *et al.*, 2011) Today ALD has emerged as a powerful tool in nanotechnology in various applications such as high-k transistors, solid oxide fuel cells, and solar cell devices. (Johnson *et al.*, 2014) Research of ALD in the catalytic process with inspiring results has been reported. Weimer et al. deposited platinum (Pt) on the TiO_2 surface by ALD which resulted in a significant improvement in the photocatalytic activity for the oxidation of methylene blue (MB). (Zhou *et al.*, 2010) Rikkinen et al. prepared palladium (Pd) nanoparticles on porous carbon support by ALD, which showed about 50 mV lower onset potential and 2.5 times higher mass activity than that of the commercial catalyst Pd/C for the electrochemical oxidation of alcohol.(Rikkinen *et al.*, 2011) Lewis et al. deposited the ALD-TiO_2 layers on a Si electrode, in conjunction with the Ni oxide electrocatalyst. (Hu *et al.*, 2014) The Si photoanode modified with the ALD-TiO_2 exhibited a catalytic stability of the oxidation of the KOH aqueous to O_2 for more than 100 hours and an almost 100% Faradaic efficiency. Sun et al. isolated the single platinum clusters and atoms by ALD which could hold the 37 times enhanced catalytic activity and a high stability compared to the commercial Pt/C catalyst for HER.(Cheng *et al.*, 2016) The catalytic reactions of water split for nanomaterials designed by ALD technique could be referred to previous reviews.(Bae *et al.*, 2017; Wang *et al.*, 2014) The reports of the application of the ALD technique

in the catalytic reduction of CO_2 are relatively few, which indicates the possibilities for the further exploration.

1.7.2 The ALD catalyst materials for enhanced CO_2RR performance

The ALD-prepared materials can participate in the design of the catalysts in different ways such as the main catalysts, the stabilizers, and the connections in between. To achieve the performance improvement of the reduction of CO_2, the selection of the catalyst materials is pivotal. However, the ALD technique with gas-phase chemicals as the precursors could well restrain the range of materials. (Puurunen, 2005) **Table 1.1** lists the overview comparison of the ALD-based catalysts for the electroreduction of CO_2. ALD technique brings fresh blood to the material design and the catalytic performance boost in ECO_2RR. The MOF material fabricated ALD reveals an high selectivity for CO production above 76% and stability over 7 h with a per-site turnover number (TON) of 1400 in the ECO_2RR.(Kornienko *et al.*, 2015) Sargent et al. achieved homogeneously dispersed sulfur elements into the Sn metal by the ALD of SnS_x followed by an in situ reduction process to make the sulfur-modulated tin (Sn(S)) catalysts towards the electrochemical reduction of CO_2 into formate. (Zheng *et al.*, 2017) The ALD-SnO_2 modified CuO nanowire electrode shows high performance towards the electrochemical reduction of CO_2 to CO, reaching a selectivity as high as 97% of all the reduction products. (Schreier *et al.*, 2017) ALD-TiO_2 multi-layer CNT catalyst achieves the H_2/CO syngas production at −1.06 V vs NHE with TONs of 308 for CO, and 597 for H_2 within a 15 min electrolysis period. (Wang *et al.*, 2017) The ALD-ZnO coated Cu exhibits a larger current density than that of the normal Cu cathode, while ALD-ZnO thin film on the Cu particles lowers the reaction overpotentials for the deoxygenation steps. (Zhang *et al.*, 2013b) The ALD-Al_2O_3 layers on the Ni electrode act as a dense barrier layer on the Ni anode surface, preventing the corrosion of Ni into the electrolyte, which leads to the poison of the cathode. It demonstrates the capability of ALD in designing the electrode with the controlled catalyst's composition and the current density to directly grow the highly crystalline multi-walled carbon nanotubes (MWCNTs) from the ambient CO_2. (Douglas *et al.*, 2017) ALD-TiO_2 and Al_2O_3 are commonly used as the over coatings on the active catalysts.

Table 1.1 The overview comparison of ALD-based catalysts for CO_2 reduction or capture.

ALD-prepared material	Synthetic conditions for ALD	Substrate	Main reduction product	The ECO_2RR efficiency	Ref.

Al_2O_3	Al_2O_3: Trimethylalumane and H_2O	Ni wires	Carbon nanotube (CNT)	Yield $_{CNT\sim33\ to\ \sim23\ nm}$: 99%	(Douglas *et al.*, 2018; Douglas *et al.*, 2017)
TiO_2	TiO_2: Tetrakis (dimethylamido) titanium and H_2O, 150℃	CNT and Ru(II) polypyridyl carbene complex	CO	$FE_{CO/H2}$ = 70%, TON_{CO} = 308, at −1.06 V vs. NHE	(Wang *et al.*, 2017)
SnO_2	SnO_2: Tetrakis(dimethylamido)-tin (IV) and O_3, 118℃	CuO nanowires	CO	FE_{CO} = 81% at −0.55V vs. RHE, η_{CO} = 440 mV [e]	(Schreier *et al.*, 2017)
Sn(S)	SnS_x: tetrakis(dimethylamino)-tin (IV) and H_2S, 90℃	Au needles	Formate	$FE_{Formate}$ = 93%, J = 55 $mA{\cdot}cm^{-2}$ at -0.75V vs. RHE	(Zheng *et al.*, 2017)
$[Al_2(OH)_2TCPP\text{-}M']$[j]	Al_2O_3 precursor: H_2O and Trimethylaluminium, 60℃	Carbon disk	CO	FE_{CO} = 75.95%, TON_{CO} = 1400 at −0.7 V vs. RHE	(Kornienko *et al.*, 2015)

2 Chapter 2 Key Performance Characterization Techniques

2.1 Overview

In this work, the ECO_2RR catalysts mentioned in Chapters 3-5 were synthesized in different methods, including ball-milling, high-temperature pyrolysis, and atomic layer deposition. The detailed experimental procedures and characterization of each synthesized material are described within the proceeding chapters. In this chapter, some key performance measurement techniques and characterization techniques related to the evaluation and study of the structure, morphology, and composition of ECO_2RR electrocatalysts are briefly discussed.

2.2 Physical Characterization Methods

Some key physical characterization methods employed in this thesis include X-ray Diffraction (XRD), X-ray photoelectron spectroscopy (XPS), scanning electron microscopy (SEM), transmission electron microscopy (TEM), and X-ray absorption spectroscopy (XAS).

2.2.1 Powder X-ray diffraction (XRD)

XRD is a common characterization technique for nanoscale materials. Analysis of a sample by powder XRD provides important information that is complementary to various microscopic and spectroscopic methods, such as phase identification, sample purity, crystallite size, and, in some cases, morphology. (Holder *et al.*, 2019) XRD techniques are used for the identification of crystalline phases of various materials and quantitative phase analysis.(Bunaciu *et al.*, 2015) Crystal atoms scatter incident X-rays, primarily through interaction with the atoms' electrons. This phenomenon is known as elastic scattering. In the majority of directions, these waves cancel each other out through destructive interference, however, they add constructively in a few specific directions, as determined by Bragg's law:

$$\mathrm{n}\lambda = 2\mathrm{d}\sin\theta \qquad 2.1$$

where n is an integer, λ is the characteristic wavelength of the X-rays impinging on the crystalline sample, d is the interplanar spacing between rows of atoms, and θ is the angle of the X-ray beam concerning these planes. **Figure 2.1a** depicts the principle behind the diffraction techniques of Bragg's law. The path difference between two incident beams 1 and 2 reflected at two adjacent atomic planes is $2\mathrm{d}\sin\theta$. Constructive interference occurs when the path difference is equal to the integer multiple of the X-ray wavelength $(\mathrm{n}\lambda)$. (Shao *et al.*, 2022) When Bragg's law is

satisfied, X-rays scattered by the atoms in the plane of a periodic structure are in phase and diffraction occurs in the direction defined by the angle θ. **Figure 2.1b** shows an XRD pattern example of CdS. The inset illustrates the crystal structure of wurtzite CdS with the (002), (100), and (101) planes. This diffraction pattern can be thought of as a chemical fingerprint, and chemical identification can be performed by comparing this diffraction pattern to a database of known patterns.

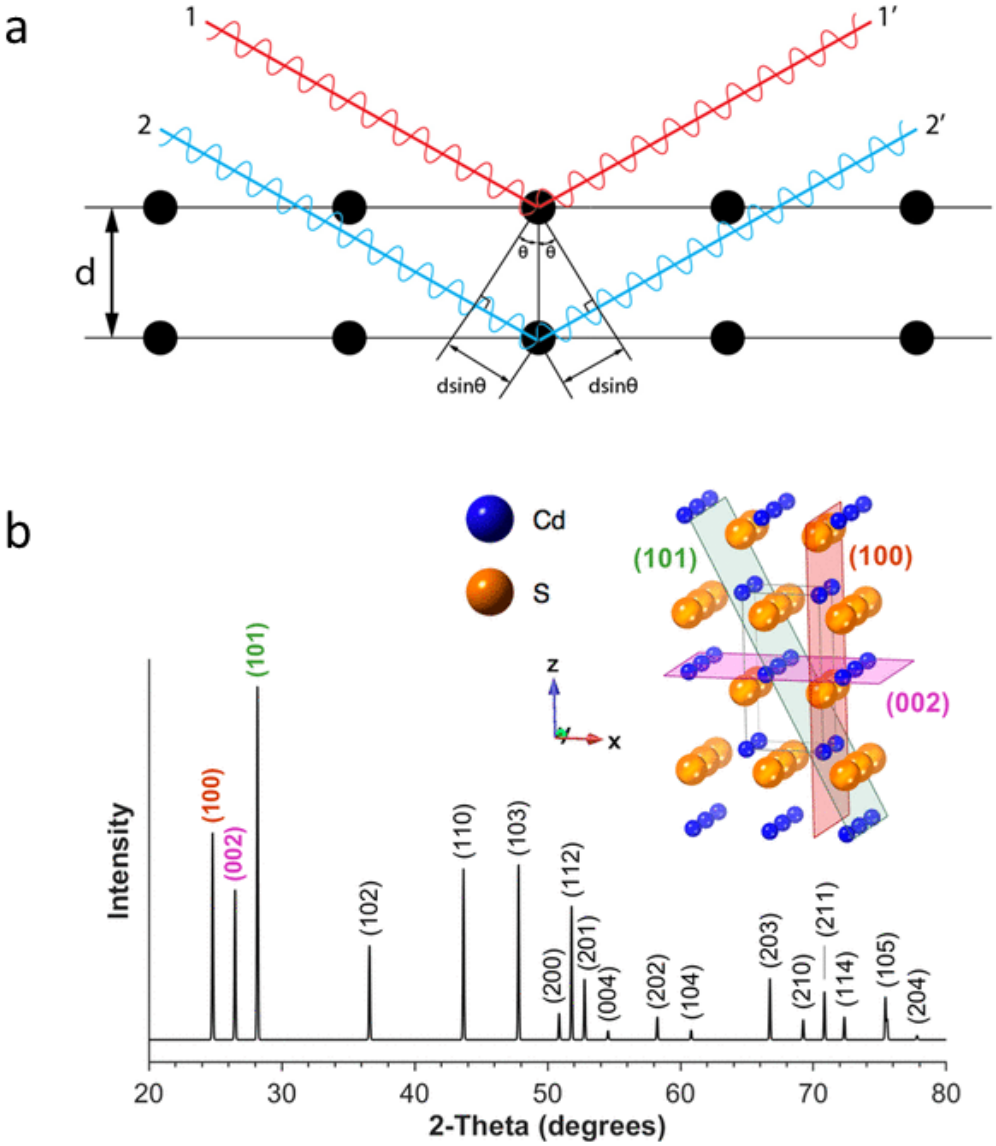

Figure 2.1 (a) Simple diagram of an XRD. Reprinted with permission from ref. (Shao et al., 2022) (b) The example of simulated and indexed powder XRD pattern for bulk (1 μm) wurtzite CdS. Reprinted with permission from ref. (Holder et al., 2019)

2.2.2 X-ray Photoelectron Spectroscopy (XPS)

XPS is a surface-sensitive quantitative analysis method to accurately obtain the elemental composition of solid materials. (Andrade, 1985; CHUANG *et al.*, 1976; Konno, 2016) This technique is the most extended tool for chemical characterization due to: 1) the non-destructive; 2) the broad analysis window that covers all the elements other than H and He; and 3) the high sensitivity. Considering the low escape depth of the photoelectrons inspection (≈ 2-10 nm), this technique is the most suitable for thin-film and surface applications and processes. Its working principle is based on the photoelectric effect shown in **Figure 2.2**. The photon energy can be absorbed completely by the electronic cloud of the atoms. According to the Einstein equation: $E_{kinetic} = hv - E_{binding}$, if the photon energy (hv) is high enough, this can cause the ejection of the photoelectrons with kinetic energy ($E_{kinetic}$). The photon energy and electron binding energy ($E_{binding}$) of the ejected electron determine the kinetic energy of photoelectrons. It provides a total elemental analysis (except for hydrogen and helium) as well as chemical bonding information. (Andrade, 1985) In this work, the XPS is carried out to detect the component on the surface of prepared catalysts.

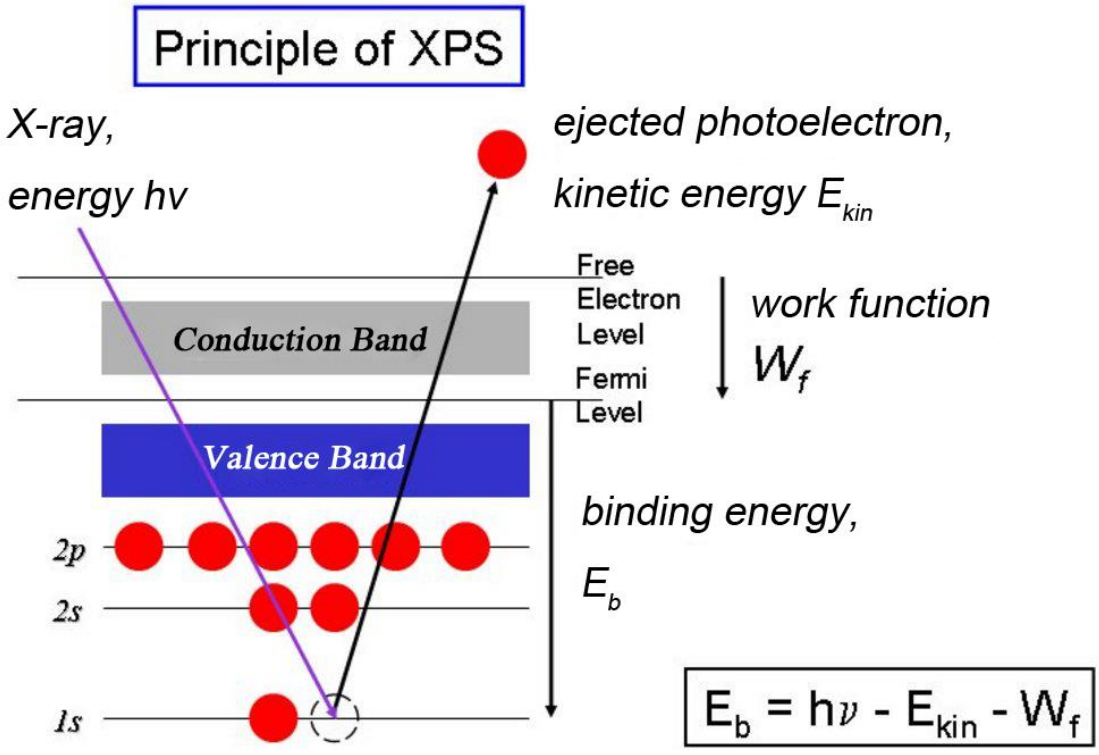

Figure 2.2 XPS working principle. (refer to IFW-Dresden, https://www.ifw-dresden.de/ifw-institutes/ikm/micronano-structures/methods/xps)

2.2.3 Scanning electron microscopy (SEM)

SEM is an electron microscope technique that forms images in the range of micro space or nano space of a sample by scanning its surface with a focused beam of electrons. (Vernon-Parry, 2000) As demonstrated in **Figure 2.3**, when the electrons interact with the sample, it will produce various signals that contain information about the surface topography and composition of the sample. These signals produced include secondary electrons (SE), back-scattered electrons (BSE), characteristic X-rays and light (cathodoluminescence) (CL), etc. Both SE and BSE are used in SEM image production. The SEs with low energy less than 50 eV only escape from the surface (few nanometers) of a sample, which makes them useful for the examination of surface morphology. The SE mode has the highest resolution among SEM signals. In contrast, BSE is a high-energy electron re-emitted from the sample due to elastic scattering. BSEs are most used to reveal chemical compositional differences (atomic number contrast). Compared with SE, BSE originating from deeper locations within the specimen shows poor resolution of images.

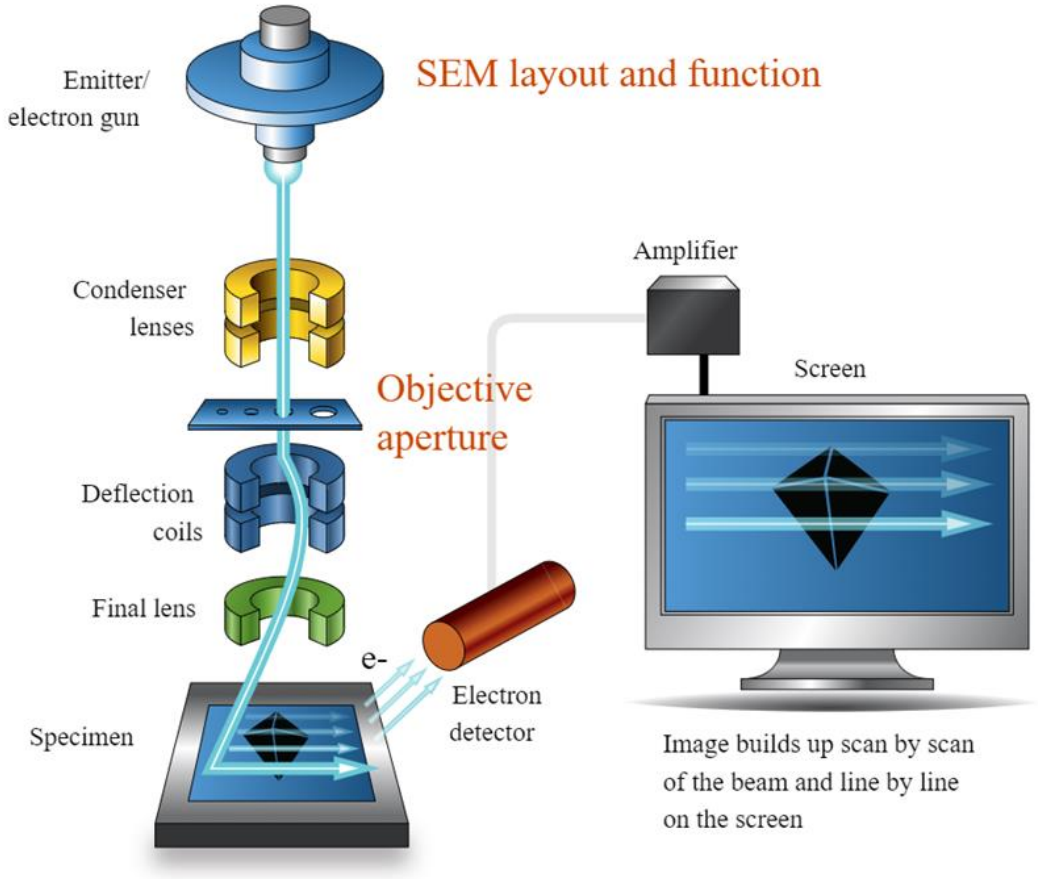

Figure 2.3 Simple diagram of a typical SEM. (refer to Microscopy Australia, https://myscope.training/#/SEMlevel_2_3)

2.2.4 Transmission electron microscopy (TEM)

TEM is a microscopy technique in which a beam of electrons is transmitted through a specimen to form an image as shown in **Figure 2.4**. While SEM provides the resolution in micro and nano space, TEM can offer the image resolution at the angstrom level. With the booming of nanotechnology in the material design domain, TEM becomes indispensable in catalyst material characterization to examine ultra-small particles. Same as SEM, it operates on the same basic principles as the light microscope but uses electrons instead of light. The specimen is most often an ultrathin section less than 100 nm thick or a suspension on a grid. An image is formed from the interaction of the electrons with the sample as the beam is transmitted through the specimen. The higher resolution of TEM than light microscopes is owing to the smaller de Broglie wavelength of electrons, which enables TEM to capture the fine detail of materials, such as particle size, shape, interparticle interaction, crystallinity, number of layers, and morphology. In addition, different types of diffraction patterns obtained from TEM suggest different crystallization structures. For instance, dotted, center-circled, and diffuse-circled diffraction patterns correspond to mono-crystalline, polycrystalline, and amorphous structures, respectively. This type of characterization of materials is essential on a length scale from atoms to hundreds of nanometers. TEM instruments can be performed with many operating modes, including conventional imaging, scanning TEM imaging (STEM), diffraction, etc. For conventional imaging, contrast may be due to differences in the thickness or density, atomic number, crystal structure or orientation, etc. **Figure 2.4** depicts the schematics of imaging and diffraction modes in TEM. In addition, bright-field and dark-field images of TEM are used to discover the size, morphology, and crystal lattice of the sample. A bright-field image is a most commonly used image. In the bright-field mode, the transmitted or unscattered electron beam is selected with the aperture, and the scattered electrons are blocked. Therefore, areas with crystalline or high-mass materials will appear dark. In the dark-field mode, the scattered electrons are selected, and the unscattered electron beam is excluded. Hence, the areas with materials will appear bright, and the areas with no samples will be black. This technique can be used to enhance contrast when the bright-field image is not clear enough, especially when imaging crystalline features that are too small or are drowned out of view. (Wang, 2003)

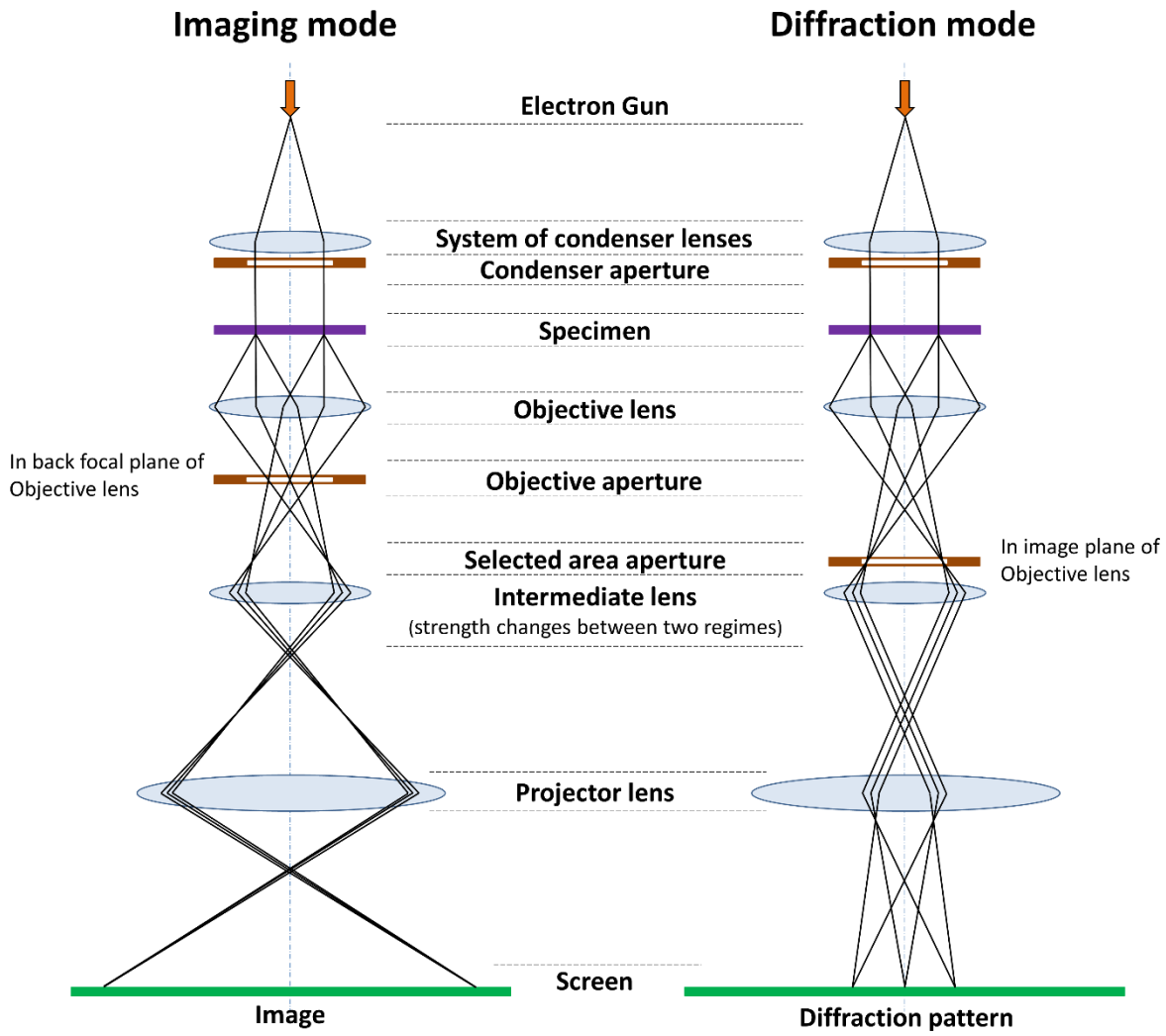

Figure 2.4 Schematic view of imaging and diffraction modes in TEM. (By Eric Kvaalen - Own work, CC BY-SA 4.0, https://commons.wikimedia.org/w/index.php?curid=85779398)

2.2.5 Energy Dispersive X-Ray Spectroscopy (EDS)

EDS is a technique supplement to SEM and TEM to visualize the chemical composition map of the target material. X-ray generates when the electron beam emitted from the gun penetrates and interacts with the volume beneath the surface of the sample. The principle is defined very well in physics. When electrons enter the coulomb field of a specimen it will decelerate and the loss of electron energy emits as a photon, which can be detected in SEM and TEM analyses. Those photons have energies particular to specimen elements, which provides the SEM and TEM the capabilities of distinguishing the various element in the material. (Mohammed *et al.*, 2018) It allows the visualization of the chemical composition distribution on the sample.

2.2.6 X-ray absorption spectroscopy (XAS)

XAS is a technique for determining the local geometric and/or electronic structure of the target element. Unlike XPS detecting the kinetic energy of the emitted photoelectron, XAS probes the adsorption of a monochromatic X-ray beam with high brilliance. In XAS, a core electron is excited into unoccupied atomic/molecular orbitals above the Fermi level by the monochromatic X-ray. The total intensity of the spectrum is given by the number of unoccupied states in the initial state, while the spectral shape reflects the density of states for the core hole state. XAS could provide element-specific information on the density states of the atom, and comprehensive information on the unoccupied electronic states of the system. (de Groot, 2001) XAS data is obtained by tuning the photon energy, using a crystalline monochromator, to a range where core electrons can be excited (0.1-100 keV). The edges are, in part, named by which the core electron is excited: the principal quantum numbers n = 1, 2, and 3, correspond to the K-, L-, and M-edges, respectively **(Figure 2.5a)**. The operation is usually performed at synchrotron radiation facilities, which provide intense and tunable X-ray beams. The most intense features are due to electric-dipole-allowed transitions to unoccupied final states. For example, the most intense features of a K-edge are due to core transitions from 1s→p-like final states, while the most intense features of the L_3-edge are due to 2p→d-like final states **(Figure 2.5b)**. There are four main regions found on an x-ray absorption spectrum: 1) pre-edge ($E < E_0$); 2) x-ray absorption near edge structure (XANES) ($E_0 - 10 < E < E_0 + 50$ eV); and 3) extended x-ray absorption fine structure (EXAFS), ($E_0 + 50 < E < E_0 + 1000$ eV). In the pre-edge region, the electron transitions from the core level to the higher unfilled or half-filled orbitals occur. In the XANES region, transitions of core electrons to non-bound levels with close energy happen. Because of the high probability of such a transition, a sudden raise in absorption is observed. In the EXAFS region, due to the high kinetic energy ($E-E_0$) of the photoelectrons, single scattering by the nearest neighboring atoms normally dominates. Hard X-ray (metal K-edge) could not only provide information on the metal oxidation states but also give insights into the local coordination environments (from EXAFS), which is essential for SAC characterization. Soft X-ray (covering 3d metal L-edge) is based on direct electron excitations to the valence 3d states from inner 2p states, thus is likely to provide a more sensitive and direct probe of the metal oxidation states than that of K-edge XAS. Recently, the inclusive Resonant Inelastic X-ray Scattering (RIXS) features of XES emerges to investigate the electronic structure of materials. RIXS signals can monitor the energy distribution of emitted photons at each excitation photon energy. If the incident photon energy is not equal to the scattered photon energy that is dependent on the incident photon energy (that is to say, the energy loss or energy transfer takes place), RIXS will be achieved. Benefiting from the fast development of the high flux-density

synchrotron light sources, RIXS can sometimes provide extra features and information with subtle changes in electronic structures to supplement the results from normal XANES and EXAFS.

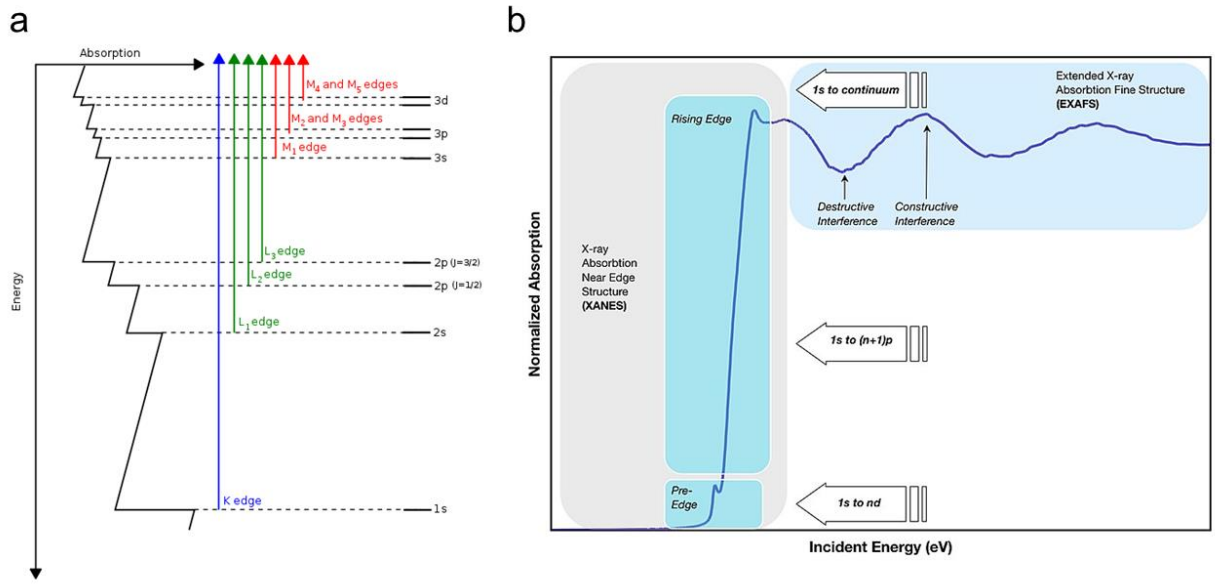

Figure 2.5 (a) Transitions that contribute to XAS edges. (By Atenderholt at English Wikipedia, CC BY-SA 3.0 <https://creativecommons.org/licenses/by-sa/3.0>, via Wikimedia Commons) (b) Three regions of XAS data for the K-edge. (By Munzarin at English Wikipedia, CC BY-SA 3.0, https://commons.wikimedia.org/w/index.php?curid=38941359)

2.2.7 Gas sorption analysis

Gas adsorption analysis is a useful tool to investigate the surface area and pore structure of solid materials. N_2 gas sorption is the most commonly used method for the BET surface area analysis, pore size distribution, and pore volume distribution. It can compare the total surface area between different samples and provide detailed information on micro-, meso-, and macro-pore structure of the material, which are essential to the catalytic activity of catalysts. (Cychosz *et al.*, 2018) In this thesis, we employed N_2 sorption analysis to characterize the surface area and the fine pore structure of catalyst materials.

2.3 Electrochemical characterizations

2.3.1 The making of the catalyst electrode

Catalyst electrodes were prepared by dropping the catalyst ink onto the carbon paper (Sigracet 25 BC) with a fixed area of 1 cm^2. The catalyst ink was prepared by mixing 0.5 mg of the catalyst powder, 120 µL of DI water, 120 µL of ethanol, and 2 µL of Nafion® perfluorinated resin solution

(5 wt%, Sigma). The mixture was treated with ultrasound for 30 min and dropped onto the carbon paper on an 80℃ hot plate. The electrode was finally dried under 70℃ in an oven for further experiments.

2.3.2 The electrochemical performance evaluation of ECO_2RR

Cyclic voltammetry (CV, performed at the scan rate of 20 mV s^{-1}), linear sweeping voltammetry (LSV, performed at the scan rate of 5 mV s^{-1}), the chronoamperometry test, double-layer capacitance, and the electrochemical impedance spectroscopy (EIS, performed at open circuit potential with a high frequency of 100000 and low frequency of 0.01) were carried out in a custom-made two-chamber H-type cell on a CHI 760D electrochemical workstation with the catalyst electrode as the working electrode. Working and reference electrodes were fixed in one chamber and the counter electrode was fixed in the other chamber. A proton exchange membrane (Nafion™ N115) separated the two chambers of the H-cell. The reference electrode was an Ag/AgCl electrode with a saturated KCl filling solution. The counter electrode was a Pt wire. Potential versus RHE was calculated as E vs. RHE = E vs. Ag/AgCl + 0.197 V + 0.0592 V × pH. The pH values of CO_2 and N_2-saturated 0.5 M $KHCO_3$ electrolytes used in this work are 7.23 and 8.36, respectively. Unless notified elsewhere, the automatic iR compensation (80%) was applied to all the measurements.

2.3.3 The ECO_2RR set up

During the electrochemical tests, each chamber of the H-cell was filled with 40 ml 0.5 M $KHCO_3$ electrolyte. CO_2 (Praxair, 99.99%) (or N_2 (Praxair, 99.999%) for the blank experiments) was bubbled through the electrolyte in the working electrode chamber with a flow rate of 20 standard cubic centimeters per minute (SCCM) for at least 30 minutes before the tests. The gas outlet was introduced into a gas-sampling loop of the GC (9790Ⅱ, Fuli) for the quantification of CO and H_2.

The GC was equipped with a packed HaySep A column, a packed MolSieve 5 A column, and a packed Porapak N column with argon (Praxair, 99.999%) as the carrier gas. A thermal conductivity detector (TCD) was used to qualify and quantify H_2. A flame ionization detector coupled with a Ni reformer was used to qualify and quantify CO. For the FE tests, the product gas was tested in GC after 15 minutes of the reaction at each set potential.

The product gas was introduced into GC to test the FE of CO and H_2. **Figure 2.6** illustrates the ECO_2RR set up employed in this thesis.

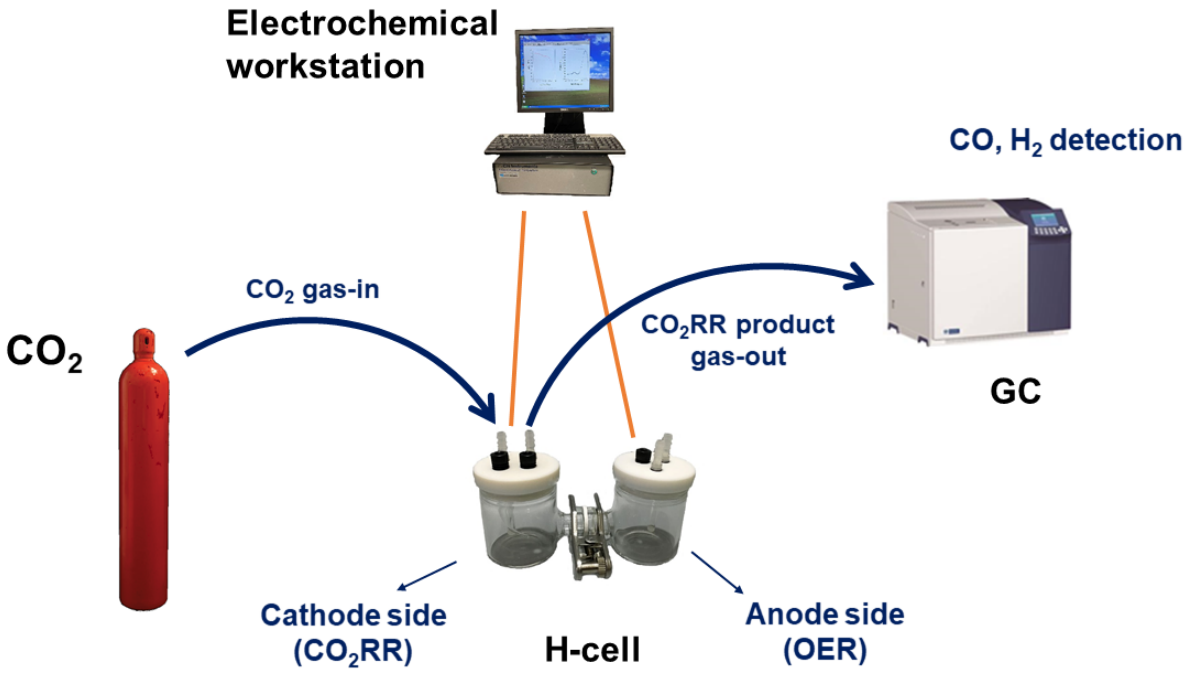

Figure 2.6 The ECO_2RR set up.

2.3.4 The calculations of FE, TOF, and Tafel slope

The calculation of FE follows **Equation 2.2**:

$$\mathrm{FE} = \frac{nFC_i vP}{jRT} \qquad 2.2$$

where n is the number of electrons involved; F as the Faradaic constant (96485.33289 C mol^{-1}); C_i as the volume fraction of a certain product determined by online GC; v = 20 sccm ($3.3*10^{-7}$ m^3 s^{-1}); P = 101300 Pa; j = Total current (A); R as the gas constant of 8.314 J mol^{-1} K^{-1}; T = 293 K.

The current densities of CO (j_{co}) and H_2 (j_{H2}) were calculated based on **Equation 2.3**:

$$j_{co(H2)} = j_{total} \times FE_{co(H2)} \qquad 2.3$$

The TOF for CO and H_2 was calculated by assuming all the active sites were M-N_4 sites and based on **Equation 2.4**:

$$\mathrm{TOF} = \frac{j_{co(H2)} \times A_{electrode}/2 \times 1.6 * 10^{-19}}{M_{sample} N_{\%} M N_{\%} N_A / 4 \times M_N} \quad 2.4$$

where $j_{co(H2)}$ is the current density of CO (j_{co}) or H_2 (j_{H2}), $A_{electrode}$= 1 cm^{-2} is the electrode geometric area, M_{sample}= $5 * 10^{-4} g$ is the mass of the catalyst on the electrode, $N_{\%}$ is the mass ratio of Nitrogen in the catalyst obtained from XPS, $MN_{\%}$ is the metal-N content ratio obtained from the XPS deconvolution results of N 1s, N_A = $6.02 * 10^{23}$ is Avogadro constant, M_N is the atomic mass of Nitrogen.

The Tafel slope was calculated based on the Tafel equation **(Equation 2.5)**:

$$\eta = \mathrm{a} + \mathrm{b} \log j_{CO} \quad 2.5$$

where η is the overpotential, b is the Tafel slope, and j_{CO} is the current density for CO formation.

3 Chapter 3 The deep understanding of the promoted carbon dioxide electroreduction of ZIF-8 derived Cobalt single-atom catalysts by the simple grinding process

Motivation

The over-emitted CO_2 in the atmosphere has been one of the top concerns of human society. (Anonyme, 2021) In the meantime, CO_2 can serve as the feedstock for many chemical productions. (Pan *et al.*, 2021) If we can reduce CO_2 into value-added products through mild catalytic conditions such as ECO_2RR that utilizes the electricity from renewable energies, it would be desirable to consume the over-emitted CO_2 and produce extra fuel chemicals for the energy crisis. (Chen *et al.*, 2019) In recent years, SACs are extremely popular in the ECO_2RR field because of their highly efficient active sites and the ability to maximize the utilization of metal atoms.(Jing *et al.*, 2022; Ma *et al.*, 2021; Yang *et al.*, 2020c) MOFs based catalysts are commonly applied in the field.(Yao *et al.*, 2021) Among them, ZIF-8 is widely studied as the template for the SAC synthesis for the easy fabrication and tunability of metal nodes in the structure for the enhanced catalytic performance in many reactions such as HER,(Mu *et al.*, 2022; Pu *et al.*, 2020) ORR,(Zhang *et al.*, 2016; Zhang *et al.*, 2019b; Zhang *et al.*, 2017) and CO_2RR.(Chen *et al.*, 2020c; Lin *et al.*, 2021; Liu *et al.*, 2020a)

As presented in Chapter 1, Co-based catalysts show great promise toward CO and syngas production in ECO_2RR. The construction of a Co-based SAC is a practical strategy to promote the ECO_2RR performance. Hence, we chose the catalyst fabrication routine for Co-SAC through the ZIF-template method that has been widely studied in literature to conduct this work to investigate the relation between subtle SAC modification and catalytic performance.

3.1 Introduction

Studies focus on the chemical modifications of the ZIF-8-derived SACs. For example, adjusting the metal-N structure in the SACs such as Fe-N,(Gu *et al.*, 2019; Mohd Adli *et al.*, 2021; Wang *et al.*, 2020a; Ye *et al.*, 2017) Ni-N,(Li *et al.*, 2020; Lu *et al.*, 2019; Yan *et al.*, 2018; Zhang *et al.*, 2021d; Zhao *et al.*, 2017) Cu-N(Yang *et al.*, 2019), and Co-N.(Wang *et al.*, 2018a) The combination of two different transition metals forms bimetallic SACs such as Fe-Ni-N-C.(Jiao *et al.*, 2021; Ren *et al.*, 2019b) Modifying the SACs with heteroatom dopants such as P,(Sun *et al.*, 2021) and F.(Ni *et al.*, 2021) These chemical variations in the catalysts prove to significantly improve the FE of the CO_2RR products in ECO_2RR.(Chen *et al.*, 2022; Zhou *et al.*, 2022) Besides

the modification in the chemical state of the ZIF-8-derived SACs, the physical properties can also be altered through chemical modifications. (Zhou *et al.*, 2021) Hu et al. used SiO_2 as a protective coating on the ZIF-8-derived Fe-N SACs, which resulted in the high porosity of the catalyst, significantly improving the current density for CO production in ECO_2RR. (Hu *et al.*, 2019) A high current density of the target product during ECO_2RR represents a big yield, which is essential for industrial applications. Therefore, the modification in the porosity aspect is promising. The chemical approach (e.g. adding a SiO_2 coating) requires multi-steps during the synthesis of the catalyst, (Yang *et al.*, 2020d) which is time-consuming and not cost-efficient. The physical and mechanical approaches are also proved efficient in the modification of the catalyst materials. For example, the fast pyrolysis method facilitates the formation of atomically dispersed Ni and the porous structures of the Ni SAC. (Guo *et al.*, 2022) The synthetic procedure of SACs usually involves a grinding-assisted procedure that is easy to handle. (Zhou *et al.*, 2020b) The grinding procedure has been proved efficient to improve the catalytic performance of the nanomaterial catalysts. (Peng *et al.*, 2013) Most of the works claimed that the grinding process during the synthesis decreased the particle size and increased the specific surface area of the catalyst, which largely contributes to the enhancement of the catalytic performance. (Ratso *et al.*, 2019) However, the deep investigation of the electronic structure evolution of metal active sites and variations of the material structure in the grinding procedure affecting the catalytic performance is rarely reported, especially for ZIF-8-derived SACs in ECO_2RR. Hence, we choose ZIF-8-derived Co SACs to conduct the investigation of the impact of the grinding process in the synthesis of ZIF-8 derived SACs for ECO_2RR.

In this work, we prepared the Co-ZIF-derived SACs. Combining different grinding processes such as hand-milling and ball-milling to create different degrees of the ground Co SACs (hand-milling and ball-milling for the moderate and intense grinding degrees, respectively), the catalysts were tested in ECO_2RR. The original Co SAC (C-Co-ZIF) that is without any grinding process exhibits a FEco of around 45% and a FE_{H2} of around 50% at -0.55 V vs. RHE and a CO current density of around 5 mA cm^{-2} at -0.7 V vs. RHE. The moderately ground sample affords the highest FEco of around 60% (about 15 % higher than that of the original C-Co-ZIF) at -0.55 V vs. RHE and the highest CO current density of around 12 mA cm^{-2} (more than 2 times higher than that of the original C-Co-ZIF) at -0.7 V vs. RHE. In contrast, the intensely ground sample only affords comparable catalytic activities to those of the original C-Co-ZIF. It suggests that the moderate grinding process promotes CO production in both production selectivity and activity. Besides, the moderately ground sample also affords better stability than that of the original Co SAC. XAS and XES confirm that the grinding process creates variations in the electronic structure of the Co

active sites in the catalysts. TEM and gas sorption analyses prove the down-sizing effect and the increased pore structures of the moderately ground sample. The variations in electronic structures of the active sites and pore structures (micro-pores for exposing active sites, meso- and macro-pores for promoting mass transfer) are the keys to the promoted ECO_2RR performance, which guides the synthesis of ZIF-8 derived SACs for catalytic reactions. To the best of our knowledge, this work is the first to combine synchrotron-based XES with XAS to investigate the subtle variations of chemical states for the grinding effects on the SACs.

3.2 Experimental section

3.2.1 Synthesis of Co-ZIF:

Typically, $Zn(NO_3)_2 \cdot 6H_2O$ (1.116 g) and $Co(NO_3)_2 \cdot 6H_2O$ (0.546 g) were dissolved in 40 mL of methanol. Then, 2-methylimidazole methanol solution (1.116 g in 40 mL) was slowly poured into the mixture solution under vigorous stirring, followed by subsequent stirring for 24 hours at room temperature. The as-synthesized powders were collected by centrifugation, washed three times with methanol, at 7000 rpm for 5 minutes, and finally dried in the oven at 80℃ overnight.

3.2.2 Synthesis of Co-ZIF with different grinding processes:

For the hand-milled sample (HM 15 mins), the powder of as-prepared Co-ZIF was placed in an agate mortar and manually ground for 15 minutes. For the ball-milled (BM) samples, the powder of as-prepared Co-ZIF was placed in ball mill tanks with PTFE balls. The ball/powder mass ratio is around 20. Then, the filled ball mill tanks were installed in a grinder (Planetary Micro Mill Pulverisette 7, FRITSCH, Germany). The ball-milling program was set at 400 rpm for 30 minutes and 60 minutes for C-Co-ZIF BM 30 mins and C-Co-ZIF BM 60 mins, respectively.

3.2.3 Synthesis of C-Co-ZIF with different milling procedures:

The powder of as-prepared Co-ZIFs with different grinding processes was placed in the tube furnace, maintained at three temperature plateaus (800 ℃, 900 ℃, and 1000 ℃, 1 hour for each) with a heating rate of 25 ℃ min^{-1} under flowing argon gas, and then naturally cooled to room temperature. All the as-prepared samples were directly used without any post-treatment.

3.2.4 Material characterizations:

Characterization instruments: XRD patterns were collected on an X-ray diffractometer (Bruker D8 Advance) with a CuKα X-ray source (λ = 1.542 Å) and a scintillator detector. The as-synthesized samples in powder form were directly used for XRD analysis. TEM and high-resolution TEM (HRTEM) were performed on a JEOL-2100F microscope (JEOL, Tokyo, Japan) operated at 200 kV. XPS experiments were undertaken on a VG Escalab 220i XL using monochromatic 1486.6 eV Al Kα radiation. The peak energies were calibrated by placing the graphite C1s peak at 284.8 eV. The spectra were fitted with mixed Gaussian-Lorentzian component profiles after a Shirley background subtraction by CasaXPS software. XANES and EXAFS at Co K-edge were collected in total-fluorescence-yield mode using a 32-element Ge detector at ambient condition on the 06ID-1 Hard X-ray MicroAnalysis (HXMA) beamline at the Canadian Light Source (CLS). During the data collection, the CLS storage ring (2.9 GeV) was operated under 250 mA mode and the HXMA superconducting wiggler was run at 1.9 T. The scan range was kept in an energy range of 7510-8350 eV for Co K-edge. Data collection configuration was using metal Co foils as energy calibrations by in-step calibration for every data set. The baseline of the pre-edge was subtracted and the post-edge was normalized in the spectra. EXAFS analysis was conducted using Fourier transform on k^3-weighted EXAFS oscillations to evaluate the contribution of each bond pair to the Fourier transform peak. The in-situ Co K-edge XANES experiments were carried out in fluorescence mode with a commercialized electrochemical operando cell (EC-FXAS-H, fluorescence mode window size: φ15 mm; 45-degree angle with X-ray incident light). The working electrode, counter electrode, and reference electrode are the catalyst electrode (same as the one described in the section on electrochemical measurements below), Pt wire, and saturated Ag/AgCl electrode, respectively. The electrolyte is 0.5 M $KHCO_3$. The gases of Ar or CO_2 were pre-bubbled into the operando cell for 30 minutes before the *in-situ* XAS experiments. The *in-situ* XAS was collected under chronoamperometry with a constant potential applied on the working electrode by a CHI 760D electrochemical workstation. On the other hand, the XANES of N K-edge and Co L-edge were measured in total X-ray electron yield mode at room temperature on the 11ID-1 High-Resolution Spherical Grating Monochromator (SGM) beamline at the CLS. The XES of Co L-edge was measured in partial fluorescence yield (PFY) mode on the 10ID-2 Resonant Elastic and Inelastic X-ray Scattering (REIXS) Beamline at the CLS. In the REIXS beamline, the X-rays are generated with elliptically polarized undulators (EPUs) made of permanent magnets with 1.6 m long and 75 mm of periodicity, and a spherical grating monochromator is used to select the X-ray energy. The REIXS beamline uses two separate gold-coated sagittal cylindrical mirrors to collect and collimate the X-rays from the EPUs. It uses three

different interchangeable gratings corresponding to low, medium, and high to cover an energy range of 95–2000 eV. On the low energy grating at 100 eV with 25 μm exit slits, the beamline delivers 10^{12} photons/s of flux. Depending on the desired energy range, four selectable mirror coatings on the plane mirrors (Ni, Si, C, and Au) are used to suppress the high-order harmonics. REIXS has a large spherical grating spectrometer, using a Rowland circle geometry to measure high-resolution XES spectra. The samples were subjected to an ultrahigh vacuum chamber. Pure metals and chemicals such as Co and CoO were used as the reference to calibrate the energy for every data set. N_2 adsorption and desorption analysis were performed on a gas sorption system (autosorb iQ, Quantachrome Instruments, Anton Paar) at 77K. “N2 at 77K on carbon (slit/cylindr. pores, QSDFT adsorption branch model)” was used as the calculation model for the analysis of pore size distribution for the samples in the ASiQWin software.

3.2.5 Electrochemical measurements:

Catalyst electrodes were prepared by dropping the catalyst ink onto the carbon paper (Sigracet 25 BC) with a fixed area of 1 cm^2. The catalyst ink was prepared by mixing 0.5 mg of the catalyst powder, 120 μL of DI water, 120 μL of ethanol, and 2 μL of Nafion® perfluorinated resin solution (5 wt%, Sigma). The mixture was then treated with ultrasound for 30 min and was dropped onto the carbon paper on an 80℃ hot plate. The electrode was finally dried under 70 ℃ in an oven for further experiments. CV was performed at the scan rate of 20 mV s^{-1}), LSV was performed at the scan rate of 5 mV s^{-1}), the chronoamperometry test, double-layer capacitance, and EIS (performed at open circuit potential with a high frequency of 100000 and low frequency of 0.01) were carried out in a customized two-chamber H-type cell on a CHI 760D electrochemical workstation with the catalyst electrode as the working electrode. Working and reference electrodes were fixed in one chamber and the counter electrode was fixed in the other chamber. A proton exchange membrane (Nafion™ N115) separated the two chambers of the H-cell. The reference electrode was an Ag/AgCl electrode with a saturated KCl filling solution. The counter electrode was a Pt wire. Potential versus RHE was calculated as E vs. RHE = E vs. Ag/AgCl + 0.197 V + 0.0592 V × pH. The pH values of CO_2 and N_2-saturated 0.5 M $KHCO_3$ electrolytes used in this work are 7.23 and 8.36, respectively. Unless notified elsewhere, the automatic iR compensation (80%) was applied to all the measurements. During the electrochemical tests, each chamber of the H-cell was filled with 40 ml 0.5 M $KHCO_3$ electrolyte. CO_2 (Praxair, 99.99%) (or N_2 (Praxair, 99.999%) for the blank experiments) was bubbled through the electrolyte in the working electrode chamber with a flow rate of 20 SCCM for at least 30 minutes before the tests.

The gas outlet was introduced into a gas-sampling loop of the GC (9790 Ⅱ, Fuli) for the quantification of CO and H_2. The GC was equipped with a packed HaySep A column, a packed MolSieve 5 A column, and a packed Porapak N column with argon (Praxair, 99.999%) as the carrier gas. A TCD was used to qualify and quantify H_2. A flame ionization detector coupled with a Ni reformer was used to qualify and quantify CO. For the FE tests, the product gas was tested in GC after 15 minutes of the reaction at each set voltage.

3.3 Results and discussion

3.3.1 Preparation and characterization of catalysts:

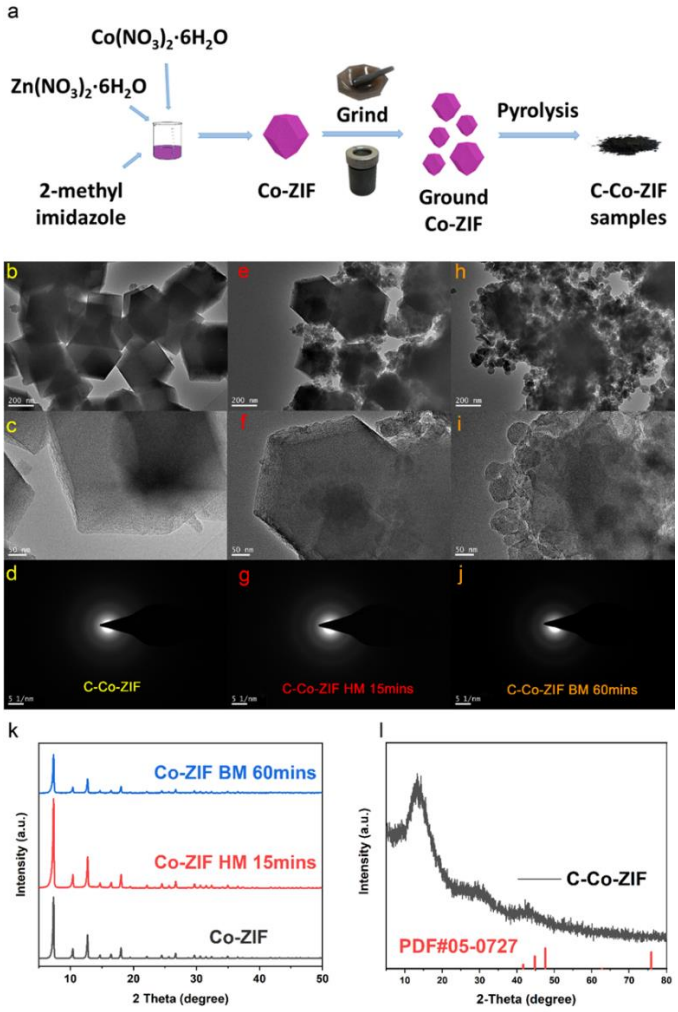

Figure 3.1 (a) The schematic of the synthetic procedure of C-Co-ZIF samples with the grinding process. (b, c) TEM images, and (d) SAED of C-Co-ZIF. (e, f) TEM images, and (g) SAED of C-Co-ZIF HM 15mins. (h, i) TEM images and (j) SAED of C-Co-ZIF BM 60mins. (k) XRD patterns of Co-ZIF, Co-ZIF HM 15mins, and Co-ZIF BM 60mins and (l) C-Co-ZIF and standard Co crystal PDF card.

A one-pot synthesis was employed to fabricate the Co-ZIF. Followed by different grinding processes (hand-milled 15 mins (HM 15 mins), ball-milled 30 mins (BM 30 mins), and ball-milled 60mins (BM 60 mins)) and pyrolysis, the final C-Co-ZIF samples were prepared **(Figure 3.1a)**. TEM images demonstrate that the original C-Co-ZIF has a particle size of around 300 nm **(Figures 3.1b and c)**. The grinding process breaks the C-Co-ZIF structure into small particles. The longer grinding time results in a larger number of small particles in the final sample. The sample with the moderate grinding process (C-Co-ZIF HM 15 mins) possesses a few small particles while most of the particles retain the original morphology **(Figures 3.1e and f)**. On the contrary, most of the particles in C-Co-ZIF BM 60 mins are broken into smaller ones due to the intense grinding process **(Figures 3.1h and i)**. Selected-area electron-diffraction (SAED) images display the ring shape pattern, indicating the poor crystallinity of the C-Co-ZIF samples **(Figures 3.1d, g, and j)**, which accords with the results of XRD measurements. This demonstrates that the different grinding processes did not change the crystal phase of Co-ZIF, though C-Co-ZIF BM 60 mins exhibits relatively lower peak intensities than those of the original Co-ZIF **(Figure 3.1k)**, which implies the worse crystallinity in the sample. Such a conclusion is also confirmed by the TEM results aforementioned that the particles are damaged in the C-Co-ZIF 60 mins sample, explaining its worse crystallinity than that of the original Co-ZIF. There is no obvious characteristic peak assigned to Co crystals observed for grinding-processed Co-ZIF and C-Co-ZIF samples **(Figures 3.1k and l)**, which is due to the low content of Co and coincides with the properties of SACs.

3.3.2 Electrochemical performance of the C-Co-ZIFs for ECO_2RR:

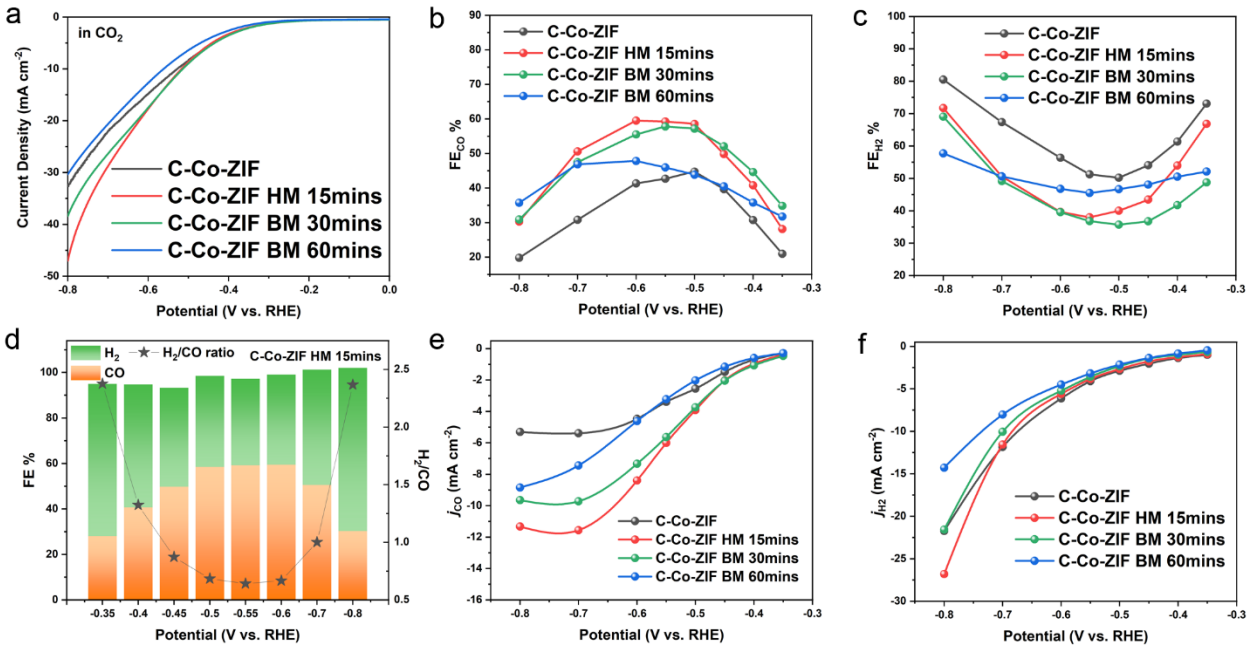

Figure 3.2 (a) The LSV curves in CO_2 atmosphere, (b) The FE_{CO}, and (c) The FE_{H2} of C-Co-ZIF, C-Co-ZIF HM 15 mins, C-Co-ZIF BM 30 mins, and C-Co-ZIF BM 60 mins. (d) The FE_{CO+H2} and H_2/CO ratio of C-Co-ZIF HM 15 mins. (e) The CO current density, and (f) The H_2 current density of C-Co-ZIF, C-Co-ZIF HM 15 mins, C-Co-ZIF BM 30 mins, and C-Co-ZIF BM 60 mins in 0.5 M $KHCO_3$.

The catalyst electrodes were applied in a customized H-cell to evaluate the catalytic performance of ECO_2RR (details in the experimental section). Several pre-run segments of CV were performed to stabilize the catalyst electrodes before the test. The LSV (**Figure 3.2a**) curves in the CO_2 atmosphere show that C-Co-ZIF HM 15 mins and C-Co-ZIF BM 30 mins have better current responses while C-Co-ZIF BM 60 mins has a worse current response than that of the original C-Co-ZIF, especially in the mass transfer region (the very negative potential range, < -0.7 V vs. RHE).

All the C-Co-ZIF samples exhibit high product selectivity towards syngas, with FE_{CO+H2} over 90% **(Figures 3.2b and c)**. Among them, C-Co-ZIF HM 15 mins affords a CO production boost of around 15%, compared with the original C-Co-ZIF. The H_2/CO ratio in the final products of C-Co-ZIF HM 15 mins can be tuned from 0.7 to 2.4 in the potential range from -0.35 to -0.8 V vs. RHE **(Figure 3.2d)**.

C-Co-ZIF HM 15 mins also affords the highest CO current density of 11.5 mA cm^{-2} at -0.7 V vs. RHE among all the samples, which is over two times higher than that of the original C-Co-ZIF **(Figure 3.2e)**. Besides, in the on-set potential region (the relatively positive potential range, > -0.45 V vs. RHE), C-Co-ZIF HM 15 mins and BM 30 mins also demonstrate higher current densities than that of the original C-Co-ZIF. In the meantime, the H_2 current densities of the catalyst

electrodes are close in the on-set potential range, demonstrating that the grinding process can promote the selective production of CO for the catalysts. C-Co-ZIF HM 15 mins stands out in the more negative potential range that is controlled by mass transfer (Figure 3.2f) in H_2 production, the same as in CO production. It indicates that the moderate grinding process also promotes the mass transfer in ECO_2RR of C-Co-ZIF. To understand the underlying impact of the grinding process on the catalytic performance, we investigate the properties of the samples through different characterization measurements.

3.3.3 Mechanism investigation:

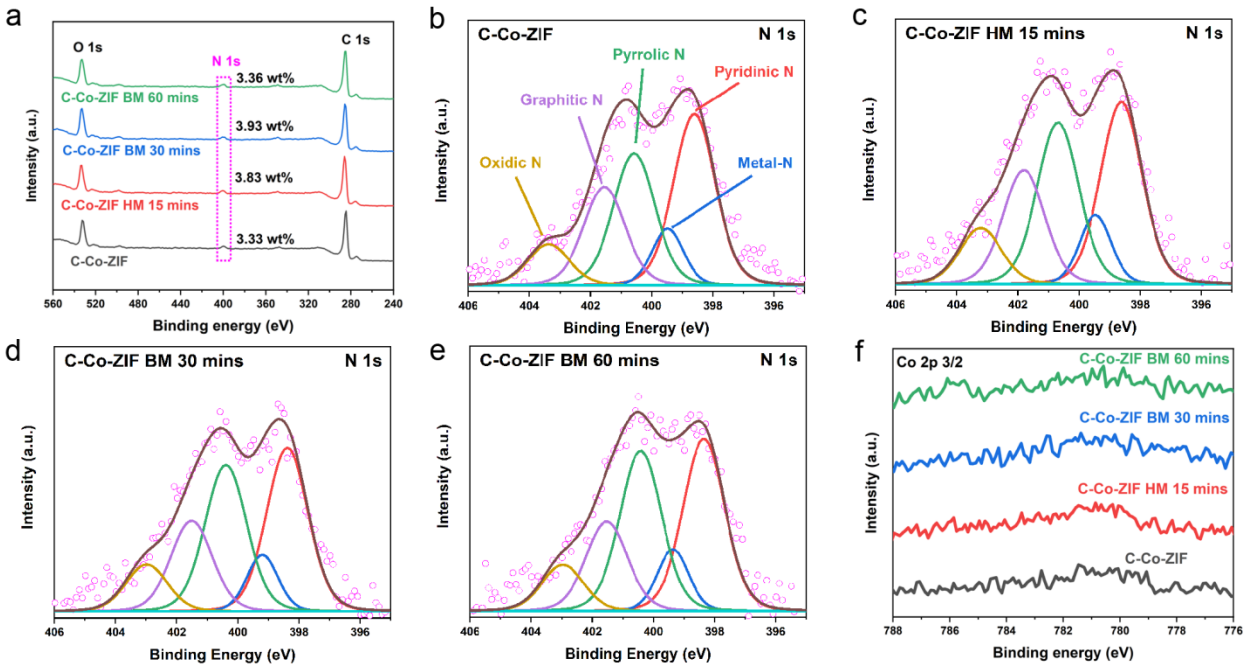

Figure 3.3 (a) Enlarged XPS survey spectra of N 1s region. N 1s XPS of (b) C-Co-ZIF. (c) C-Co-ZIF HM 15 mins. (d) C-Co-ZIF BM 30 mins. (e) C-Co-ZIF BM 60 mins. (f) Co 2p 3/2 XPS of the C-Co-ZIFs with different grinding processes.

XPS is a surface-sensitive technique that could identify and quantify specific species of material. We employed XPS to analyze the surface composition of our samples (**Figure 8.1**). The absolute N content can be obtained from the survey of XPS **(Figure 3.3a and Table 8.1)**. The N 1s XPS results illustrate that C-Co-ZIF contains different types of N species, such as pyridinic N, metal-N, pyrrolic N, and graphitic N **(Figure 3.3b)**. Samples with different grinding processes exhibit the same N components **(Figures 3.3c-e)**. Among these N species, the metal-N binding represents the Co-N content in the catalyst, which is essential for SACs.(Lin *et al.*, 2019; Zhang *et al.*, 2019a) The contents of metal-N binding for all the C-Co-ZIF samples with different grinding processes

are close (around 9%). Combined with the absolute N content obtained from the XPS surveys, the absolute M-N content can be calculated as well **(Table 8.2)**. Co, as the metal center of the active site of Co-N, needs to be thoroughly investigated. The signals of Co 2p XPS are too noisy to make an accurate deconvolution analysis **(Figure 3.3f)**. Hence, we further characterized the samples with synchrotron-based XAS that is sensitive and could provide chemical information for low-content elements in the materials. *In-situ* Co K-edge XANES of C-Co-ZIF are displayed in **Figure 3.4a**. Compared with that in Ar-saturated 0.5 M $KHCO_3$ solution, shown in the figure inset, a spectral shift towards higher energy occurs in the CO_2-saturated condition under open circuit potential (OCP), implying a higher Co oxidation state. This is due to the delocalization of the unpaired electrons in the 3d orbital transferring from Co to the C 2p orbital of CO_2,(Yang *et al.*, 2018) which suggests the adsorption of CO_2 on Co atoms in C-Co-ZIF. Under the ECO_2RR condition, the Co K-edge XANES shifts back towards the lower energy **(Figure 3.4a, inset)**. It reflects the response of Co atoms to the applied potential, confirming that Co atoms act as the active center during ECO_2RR.

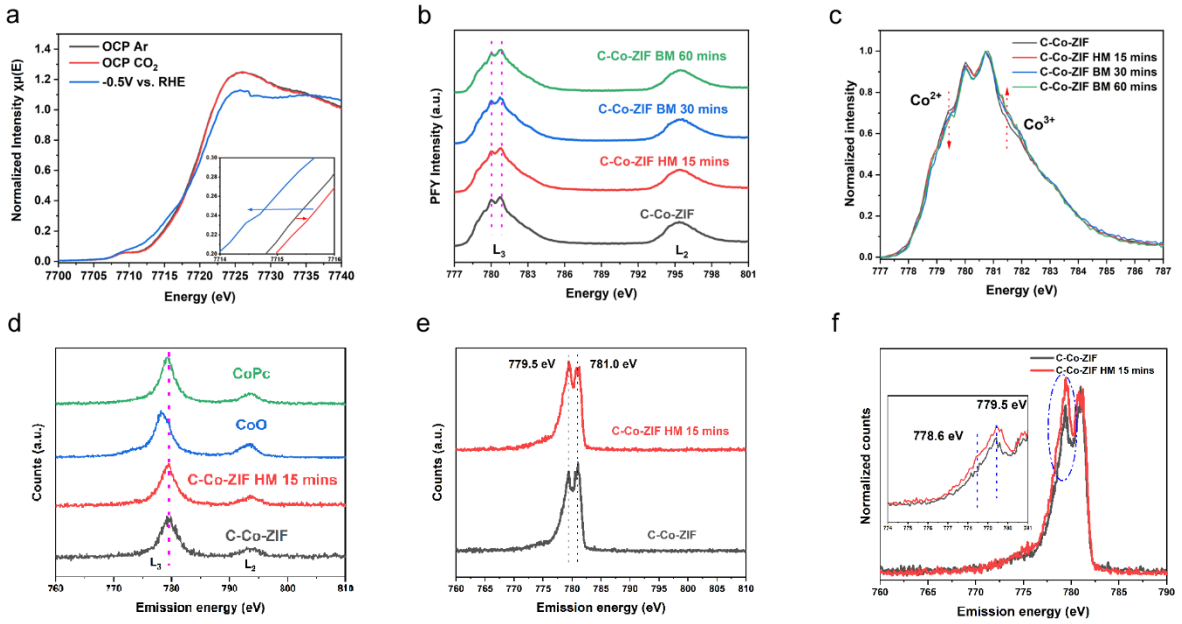

Figure 3.4 (a) Normalized in-situ Co K-edge XANES spectra for C-Co-ZIF at various potentials in 0.5 M $KHCO_3$ aqueous solution at room temperature at ambient pressure of Ar or CO_2 atmospheres. The inset is the enlarged Co K-edge XANES spectra. (b) Co L-edge XAS in partial fluorescence yield (PFY) mode of C-Co-ZIF samples with different grinding processes. (c) Enlarged Co L-edge XAS in the L_3 region. (d) XES spectra of C-Co-ZIF samples with different grinding processes, excited at 813.0 eV. (e) XES spectra of C-Co-ZIF and C-Co-ZIF HM 15 mins, excited at 781.0 eV. (f) Enlarged XES spectra of C-Co-ZIF and C-Co-ZIF HM 15 mins, excited at 781.0 eV.

Further investigation into the variation of the chemical states of Co in the samples is necessary. Soft X-ray (covering 3d metal L-edge) is based on direct electron excitations to the valence 3d states from inner 2p states, thus is likely to provide a more sensitive and direct probe of the metal oxidation states. Therefore, the soft X-ray spectra of the 3d metal L-edge were measured. The Co L-edge XAS **(Figure 3.4b)** spectra show that all the C-Co-ZIF samples with different grinding processes exhibit a similar pattern with two main peaks in the region of 780.0 eV (marked in pink dot lines). It indicates that C-Co-ZIF retains a similar 3d electronic structure despite the grinding processes. After spectral normalization, it reveals that there is an intensity decrease in the shoulder at ca. 779.5 eV and an intensity increase in the shoulder at ca. 781.5 eV **(Figure 3.4c)**. These two shoulders refer to the Co^{2+} and Co^{3+} features, respectively. (Hibberd *et al.*, 2015) It implies that the ground samples are slightly oxidized to a higher oxidation state. XES can be performed at the excitation energy that is higher than the resonant energy of the orbital electrons, which offers filled electron states information in the region. We applied XES to further investigate the details of the chemical states of Co in the samples. The XES spectra of C-Co-ZIF and C-Co-ZIF HM 15 mins under the excitation energy of 813.0 eV are displayed in **Figure 3.4d**, offering the normal emission of L_α and L_β of Co. The emission peaks at ca. 779 eV of our samples are closer to that of CoPc rather than that of CoO. It indicates that the chemical state of Co in our samples is similar to the Co-N_4 in CoPc. The XES at the excitation energy of 781.0 eV (resonant region) depicts two features at ca. 781.0 eV and ca. 779.5 eV for the original C-Co-ZIF and C-Co-ZIF HM 15 mins **(Figure 3.4e)**. The peaks at 781.0 eV are the elastic scattering peaks in which the photon is emitted at the same energy as the incoming energy. The peak at 779.5 eV also appears for the XES spectra at the excitation energy of 813.0 eV **(**non-resonant region, **Figure 8.2)**, suggesting it is the fluorescent feature of Lα whose position is independent of the excitation energy, which corresponds to the de-excitations from 3d orbitals. A slight difference can be witnessed between these two samples after normalized to the peak intensity of the 781.0 eV peak **(Figure 3.4f)**. For C-Co-ZIF, the intensity of the 779.5 eV peak is relatively lower than that of the 781.0 eV peak. On the contrary, for C-Co-ZIF HM 15 mins, the intensity of the 779.5 eV peak is relatively higher than that of the 781.0 eV peak, along with a shoulder peak at ca. 778.6 eV **(inset in Figure 3.4f)**. A relatively stronger intensity of the left 779.5 eV and 778.6 eV peaks corresponds to the de-excitations from the filled 3d orbitals to the core holes located in 2p states. (Niwa *et al.*, 2017) This is due to the more oxidized Co in the sample. Besides, the tail region at ca. 775 eV could be contributed by charge transfer between metal-ligand or ligand-metal (such as Co-N).(Shelke *et al.*, 2022) The higher intensity of C-Co-ZIF HM 15 mins in this tail region than that of the original C-Co-ZIF supports the XAS results (the high ratio of the intensity at Co^{3+}/ Co^{2+} of

C-Co-ZIF HM 15 mins). The XAS and XES spectra of Co L-edge demonstrate that the grinding process indeed affects the 3d electronic structure of C-Co-ZIF slightly. The metal K-edge of hard X-ray can provide information on the local coordination environments. The EXAFS of Co K-edge shows a peak located at ca. 1.5 Å that can be ascribed to Co-N/C/O bonds appearing for all the C-Co-ZIF samples with different grinding processes **(Figure 3.5a)**. Combined with the obtained results from XPS and XAS, and the reports of the literature, we believe this peak belongs to Co-N in this work, which represents the Co single-atom active sites. (Wang *et al.*, 2018a) As the degree of the grinding process becomes more intense, the intensity of the Co-N peak decreases. It indicates the distortion of the Co-N coordination environment for the ground C-Co-ZIF samples. All these XAS results confirm that the grinding process affects the local chemical environments of the Co atoms of C-Co-ZIF samples, which can contribute to the enhancement of the ECO_2RR performance. (Chen *et al.*, 2021a)

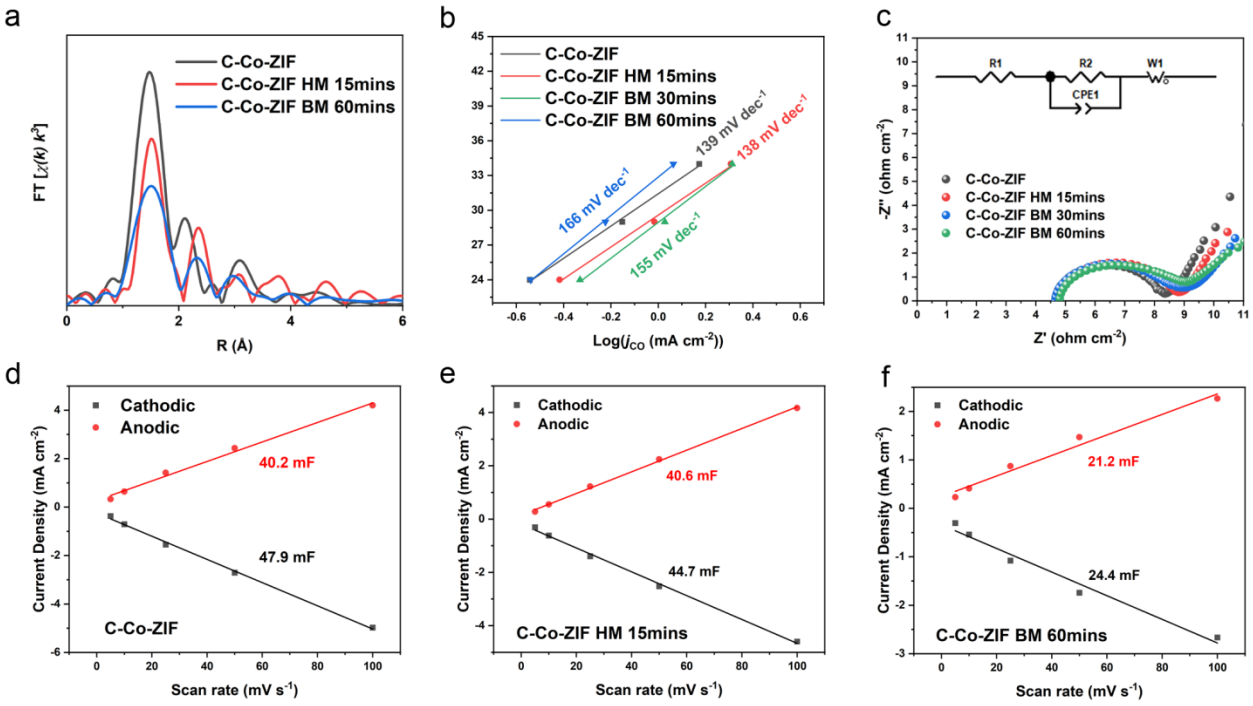

Figure 3.5 (a) Co K-edge EXAFS R space spectra. (b) Tafel slopes of j_{co}. (c) EIS results of C- Co-ZIF catalyst electrodes with different grinding processes. Double-layer capacitance tests for evaluating the electrochemically active surface area of the catalysts (d) C-Co-ZIF. (e) C-Co-ZIF HM 15 mins. (f) C-Co-ZIF BM 60 mins.

If $Co\text{-}N_4$ is assumed to be the active site in the catalysts, the number of the total active sites can be calculated to evaluate the TOF of the catalysts. The TOF results of CO production calculated at -0.7 V vs. RHE demonstrate that C-Co-ZIF HM 15 mins affords the highest TOF values of 1.91

site^{-1} s^{-1}, which is almost two times that of the original C-Co-ZIF (1.08 site^{-1} s^{-1}). C-Co-ZIF BM 30 mins and C-Co-ZIF BM 60 mins reveal close TOF values of around 1.4 site^{-1} s^{-}1 **(Table 8.2)**. They show a similar trend to that of the catalytic performance, illustrating that Co-ZIF HM 15 mins has the most effective active sites among the samples. We also evaluated the Tafel slope values of the C-Co-ZIF samples with the different grinding processes to investigate their reaction mechanism and kinetics for CO production in ECO_2RR **(Figure 3.5b)**.

C-Co-ZIF possesses a Tafel slope value of 139 mV dec^{-1}, which is close to a theoretical value of 118 m dec^{-1}, suggesting the first electron transfer step is the rate-determining step (RDS).(Gu *et al.*, 2019) A Tafel slope value of 59 mV dec^{-1} will suggest another RDS for CO production. The variations in the electronic structure of the transition metal active sites usually influence the reaction pathway of CO_2RR.(Yan *et al.*, 2018) Moreover, a higher value will also indicate more sluggish reaction kinetics. C-Co-ZIF HM 15 mins has a close value to the original C-Co-ZIF, while the BM 30 mins and BM 60 mins samples have higher values, which means the grinding process does not change the RDS but the reaction kinetics. The Tafel slope values indicate that the variations in the electronic structures of the ground samples indeed affect CO production. Although the Tafel slope values are similar for the original C-Co-ZIF and C-Co-ZIF HM 15 mins, the moderate grinding process affords the sample (C-Co-ZIF HM 15 mins) a right shift to that of the original C-CoZIF. It demonstrates that C-Co-ZIF HM 15 mins produces more CO molecules than C-Co-ZIF at the same applied potential. On the opposite, the intense grinding process makes the sample (C-Co-ZIF BM 60 mins) more sluggish and less productive in the formation of CO. The promotion in the kinetics aspect could come from the variation in the physical properties of the samples. Therefore, EIS was conducted to evaluate the charge transfer and mass transfer abilities of the catalyst electrodes (**Figure 3.5c**, inset: the equivalent circuit model for the fitting). It turns out that all the ground C-Co-ZIF samples exhibit close charge transfer resistance values (**Table 8.3**), implying there is no apparent difference in the charge transfer of the catalyst electrode. Notably, the linear parts in the low-frequency region of EIS are controlled by mass transfer.(Xie *et al.*, 2018) The slopes of the straight lines gradually change from the original C-Co-ZIF to C-Co-ZIF BM 60 mins in the mass transfer control region, which represents the mass transfer resistances (Warburg resistance, R_w) in the samples. The R_ws are 2.81 Ω, 4.88 Ω, and 29.08 Ω for C-Co-ZIF HM 15 mins, BM 30 mins, and BM 60 mins, respectively **(Table 8.3)**. The mass transfer resistance increases as the grinding process becomes more intense. For C-Co-ZIF BM 60 mins, it elevates to ten times that of C-Co-ZIF HM 15 mins, explaining the low current densities in the mass transfer range in **Figures 3.2a, e, and f** for the sample. It indicates that the intense grinding process affects the mass transfer of the samples, which can contribute to the

ECO_2RR performance as well. We further tested the double-layer capacitance of different catalyst electrodes to estimate their ECSA (**Figure 3.5d-f**). C-Co-ZIF and C-Co-ZIF HM 15 mins have close ECSA values. However, C-Co-ZIF BM 60 mins has a dramatic decrease in ECSA value. It indicates the less exposed active area of C-Co-ZIF BM 60 mins during ECO_2RR than that of the other samples, which explains its worst catalytic performance. Both EIS and ECSA results suggest variations in the physical structures of the ground samples. To discover more about this aspect, we conducted gas sorption analysis on the C-Co-ZIF samples with different grinding processes. The original C-Co-ZIF has a typical type I isotherm, meaning it has a primary micro-pore structure.(Yang *et al.*, 2020d) The isotherm pattern for all the ground samples is a combination of type I and type II isotherms **(Figure 3.6a)**. It illustrates that all the ground samples contain a similar pore structure of micro-pores and macro-pores, which implies the grinding process creates some macro-pores in the material.(Cychosz *et al.*, 2018) The cumulative surface area analyses confirm that the total surface areas are mainly attributed to the micro-and meso-pores structures in the samples **(Figure 3.6b)**. **Table 3.1** lists the BET (Brunauer, Emmett, and Teller theory) surface area, cumulative surface areas, and pore volumes of different pore structures for the samples. The BET surface area varies for different samples. The moderate grinding process increases the BET surface area while the intense grinding process decreases the BET surface area. The hysteresis loop for the HM 15 mins sample is the most obvious among all the samples, which means the increase of the micro-and meso-pores in the C-Co-ZIF HM 15 mins **(Figure 3.6a)**. (Cychosz *et al.*, 2018) The analysis of pore size distribution shows that the pore structure of C-Co-ZIF samples is dominated by the micro-and meso-pores **(Figure 3.6c)**. The original C-Co-ZIF has primarily micro-pores of the size of 0.5 nm, accompanied by a few micro-pores of the size of 0.75-1 nm and meso-pores of the size of 2-5 nm (**Figure 8.3**). The moderate grinding process (HM 15 mins) does not damage the 0.5 nm micro-pore structure much but increases the micro-pores of the size of 0.75-1 nm **(Figure 3.6e-h)**, affording a higher BET surface area than that of the original C-Co-ZIF. The intense grinding processes greatly damage the structure of the meso-pores in the material, leading to a decreased BET surface area (**Figure 8.4**). As shown in the TEM results above, the down-sized particles are significantly agglomerated together for C-Co-ZIF BM 60 mins, which might block the pores in the bulk structure. It accords with the results of the pore distribution analysis for C-Co-ZIF BM 60 mins. The micro-pores with the size of 0.7-1 nm are essential to the catalytic reactions as the micro-pores host the active sites for the reaction while this range of pore size allows the entering of the reagent molecules for the catalytic reaction to take place. It agrees with the catalytic performance and Tafel slope results that C-Co-ZIF HM 15 mins that has the most micro-pores and exhibits the best current densities

for CO production. In addition, the meso-pores and big volume pores (macro-pores) in the catalyst material could promote the mass transport of the reagent molecules.(Chenitz *et al.*, 2018) The comparison of the meso-pore distribution (**Figure 8.5**) of the samples shows that the grinding process would decrease the meso-pore structures in C-Co-ZIFs while the moderate grinding process maintains the comparable meso-pore structures to those of the original C-Co-ZIF. From the isotherm (**Figure 3.6a**, referring to the isotherm type I and type II discussion above), we can find out that the ground samples also have macro-pores. The existence of macro-pores in the ground samples is also confirmed by the visible stacked pores in the TEM results aforementioned. The moderate grinding process affords C-Co-ZIF HM 15 mins and BM 30 mins comparable meso-pores **(Table 3.1)** and increased macro-pores to those of the original C-Co-ZIF, which promotes the mass transfer. It is the reason why C-Co-ZIF HM 15 mins and BM 30 mins exhibit high current densities in the mass transfer region along with the relatively low R_w values in EIS. With fewer meso-pore structures in the catalysts, it is believed that the mass transfer of the reagent molecules in the catalyst electrodes is weakened during the ECO_2RR process, which explains the worst results in the mass transfer region of EIS and electrochemical performance tests for C-Co-ZIF BM 60 mins. Considering all the results from the characterizations and electrochemical measurements, we propose that the grinding process modifies the electronic structure of the Co-N active sites in C-Co-ZIFs to promote CO production while the increased micro-pore structures of C-Co-ZIF HM 15 mins are key to hosting the active sites in ECO_2RR. The grinding process down-sized the particle and creates more macro-pores in the material. C-Co-ZIF HM 15 mins maintains the meso-pore structures for mass transfer, accompanying the increased macro-pore structures, and benefiting the ECO_2RR process. However, the intense grinding process agglomerates the downsized particles. It significantly damages the pore structures in the catalysts, leading to the decreased active surface area and bad mass transfer, which explains the higher Tafel slope and R_w values for C-Co-ZIF BM 60 mins. Compared to the downsizing effect, the increased pore structures promote more ECO_2RR performance (**Figure 3.7**).

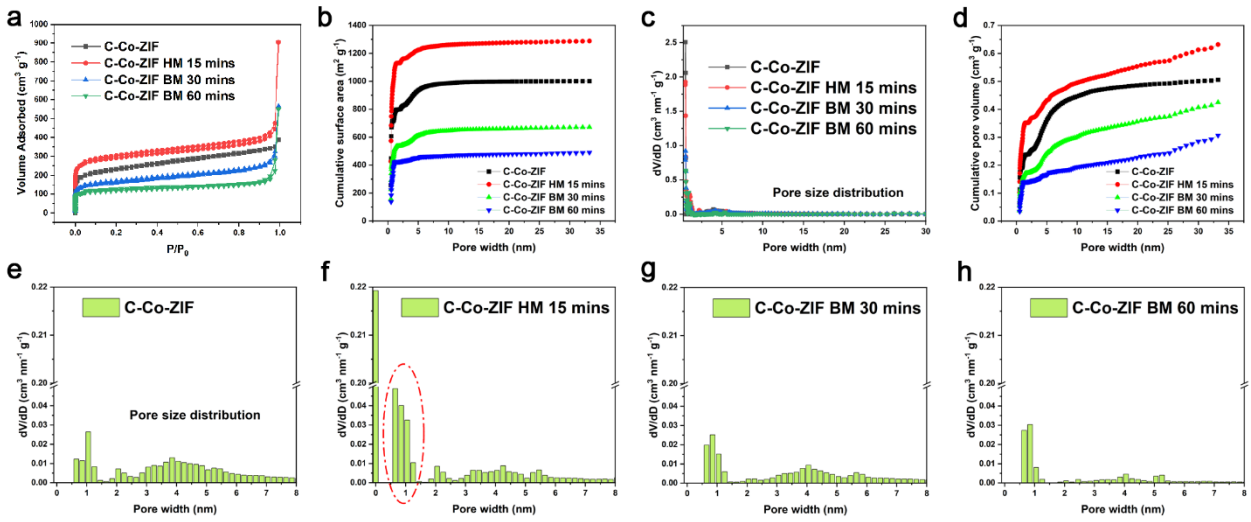

Figure 3.6 (a) The N_2 adsorption/desorption isotherm plots. (b) The cumulative surface area. (c) The pore size distribution analysis. (d) The cumulative pore volume. (e-f)The pore size distribution (0-8 nm) analysis of C-Co-ZIF samples with different grinding processes.

Table 3.1 The BET surface areas, cumulative surface areas, and pore volumes of different pore structures of the C-Co-ZIF samples with different grinding processes.

	Surface area			Pore volume	
	BET surface area (m^2 g^{-1})	Micro-pore surface area (m^2 g^{-1})	Meso-pore surface area (m^2 g^{-1})	Micro-pore volume (cm^3 g^{-1})	Meso-pore volume (cm^3 g^{-1})
C-Co-ZIF	1001.10	801.47	199.55	0.24	0.27
C-Co-ZIF HM 15 mins	1288.03	1133.61	154.17	0.35	0.28
C-Co-ZIF BM 30 mins	672.1	536.97	134.91	0.17	0.25
C-Co-ZIF BM 60 mins	489.67	426.18	63.22	0.14	0.16

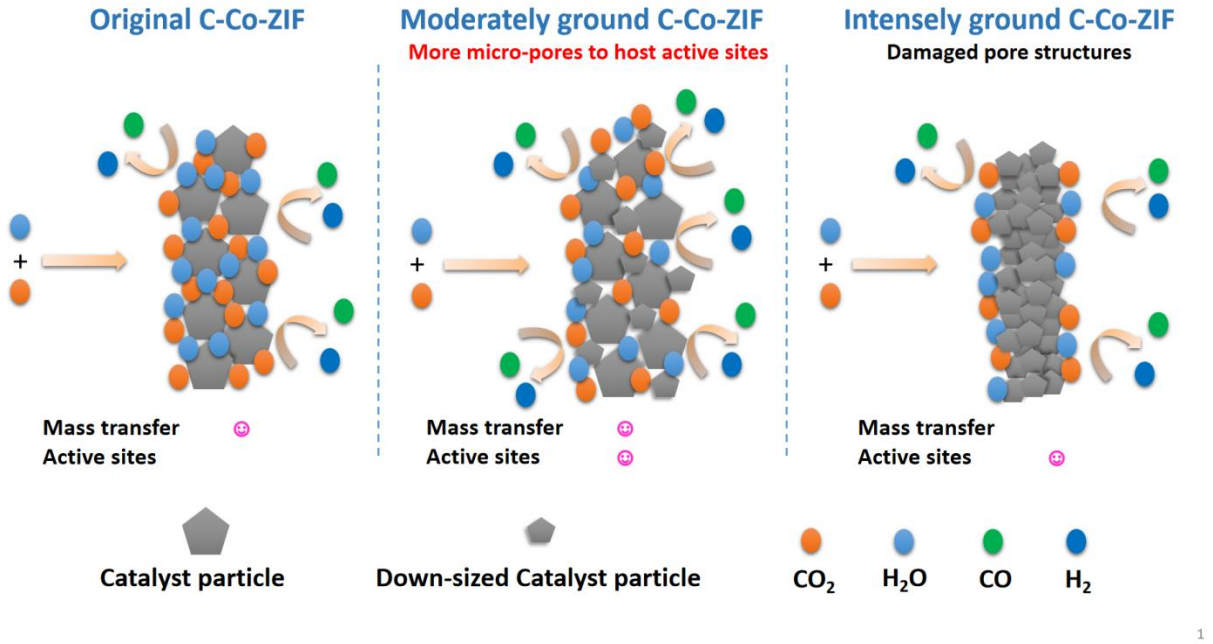

Figure 3.7 The illustration of the impacts of big and small particles on the ECO_2RR performance.

The duration tests were also performed to compare the stability of the original C-Co-ZIF and ground HM 15 mins samples **(Figure 3.8a-c)**. For the current density, the original C-Co-ZIF shows an apparent decay while C-Co-ZIF HM 15 mins demonstrates a much-alleviated decay within 10 hours. For the product selectivity, the FEco drops by 10 percent with the accordingly increased FE_{H2}, showing the quick loss of CO production ability of the original C-Co-ZIF in 10 hours. The FE_{CO} loss also appears for C-Co-ZIF HM 15 mins but only for 5 percent in 10 hours, which is half of that of the original C-Co-ZIF. The duration tests show that the moderate grinding process can promote the stability of C-Co-ZIF as well. The moderate grinding process provides mild distortion in the Co-N coordination environment for the more effective active sites for CO production. It also promotes the micro-pores to host the active sites and meso- and macro-pores for the mass transfer during ECO_2RR. The synergy of these benefits enhances CO production in both electrochemical activities and stability.

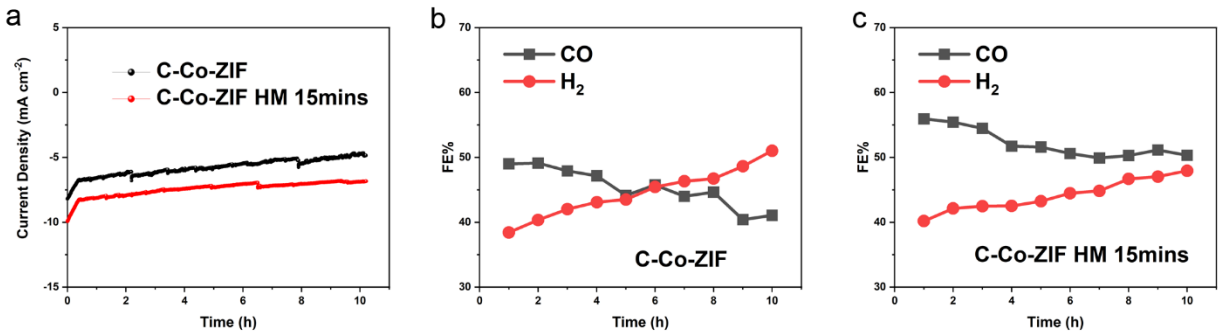

Figure 3.8 The chronoamperometry test of (a) Total current density of C-Co-ZIF and C-Co-ZIF HM 15 mins. (b) FE_{CO} and FE_{H2} of C- Co-ZIF. (c) FE_{CO} and FE_{H2} of C- Co-ZIF HM 15 mins.

3.4 Conclusion

ZIF-8-derived Co SACs with different grinding processes are synthesized through hand-milling and ball-milling methods. The moderate grinding process of HM 15 mins affords the catalyst the highest FEco (around 15 % higher than that of the original C-Co-ZIF) and current densities of CO and H_2 among all the other samples. XAS and XES results confirm the slight variations in the electronic structure of the Co active sites in the ground samples, which are caused by the grinding process. The electrochemical tests suggest that the variations in the electronic structure promote CO production in the ECO_2RR performance. From TEM and gas sorption analyses, it is believed that, instead of the down-sizing effect, the moderate grinding process increases the exposed active surface area through the augmented micro-pores while maintaining the meso-pore structure, increasing the macro-pore structures of the catalyst material, which benefits the mass transfer. The intense grinding process results in seriously damaged pore structures in the catalyst material, which leads to the decreased exposed surface area and the prohibited mass transfer of ECO_2RR. Besides, the catalyst with the moderate grinding process also affords better stability than that of the original one. The present work illustrates that the simple grinding procedure can affect the ZIF-8-derived SACs in both electronic structures and physical pore structures, which would result in the promoted catalytic performance of ECO_2RR. It might also apply to other catalytic reactions and should be considered during the synthesis and evaluation of this kind of catalyst material.

4 Chapter 4 Atomically dispersed Fe-Co bimetallic catalysts for the augmented electroreduction of carbon dioxide

Motivation

Based on the promising results from Chapter 3, we discover that physical modification like ball-milling can modify the porosity of SACs and even subtly modify the local environment of the Co active site in Co-SAC. The optimized porosity can contribute to the promoted mass transfer. The modified local environment of active sites has an impact on the CO_2RR product selectivity, which is of significant interest in ECO_2RR.

To further investigate the enhancement that the active site modification can offer to ECO_2RR, we continued our research with the modification of the active sites of Co-SAC in the following work. Contrary to the physical method applied in Chapter 3, this work concentrates on the chemical modification method to alter the local environment of Co active sites in Co-SAC.

4.1 Introduction

To fulfill the industrialization of ECO_2RR, it requires noble-metal-free-based catalysts to cut the cost while maintaining high catalytic efficiency. The state-of-art ECO_2RR catalyst design focuses on metal-based catalysts. For example, Cu-based catalysts are exclusively effective for the production of alcohols/hydrocarbons; Ag, Au, and Zn, or most recently the atomically dispersed M-N-C catalysts are efficient for CO production (Zhang *et al.*, 2021a; Zhu *et al.*, 2021). SACs are known for their efficient active sites, maximized utilization of metal atoms, and low cost. Typical SACs, such as Co-N_x (Wang *et al.*, 2018a; Zhang *et al.*, 2018e), atomically Ni or Fe-dispersed nitrogen-doped graphene (Yang *et al.*, 2018; Zhang *et al.*, 2018b), and Fe-N-C (Gu *et al.*, 2019), have revealed highly efficient CO production in ECO_2RR attributed to the unique coordination environment of single-atom sites. SACs, such as atomically dispersed Ni catalysts (Long *et al.*, 2019), and nickel@nitrogen-doped carbon nanotubes (Shen *et al.*, 2020), also demonstrate good catalytic performance on syngas production. In recent years, bimetallic catalyst materials in many mainstream reactions have been developed. The hybrid alloy structures of NiCo and FeNi benefit ORR and OER, while the synergistic effects between Pd and CoO_x promote CO oxidation (Wu *et al.*, 2018; Wu *et al.*, 2020a; Wu *et al.*, 2020b). The interaction of different metal-sites with the modification of the foreign metal could improve the intrinsic catalytic activity of ECO_2RR in bimetallic catalysts (Kou *et al.*, 2021). Pd/NbN promotes the formation of PdH during the ECO_2RR process, leading to the enhancement of syngas production (Liu *et al.*, 2020b). The combinations

of TMs Co, Ni, and Fe with noble-metal Ag create the synergism that increases the tenability of the syngas ratio in syngas production from ECO_2RR (Ross *et al.*, 2019).

The strategy of utilizing noble-metal-free catalyst materials has the advantages of the synergistic effects of different metal sites in bimetallic TM-catalysts, the augmented production rate of syngas, and tunable ratios of CO/H_2. Chen et al. fabricated bimetallic Co, Ni SACs for syngas production from ECO_2RR (He *et al.*, 2019). Benefiting from the individual selectivity towards H_2 and CO for Co and Ni, the final CoNi bimetallic catalyst exhibited the tunable H_2/CO ratios of 0.8-1.3 in the reduction product (He *et al.*, 2019). It is worthwhile for the extensive exploration, especially in the earth-abundant TM elements such as Fe, Co, Ni, and Cu for syngas production with tunable H_2/CO ratios in ECO_2RR. The classic bimetallic catalysts are alloy catalysts where two different metals are well intermixed and in close proximity/coordination to each other, thus promoting catalytic performance. The situation is very different in atomically dispersed M-N-C catalysts with different types of metals present. Further researches are ongoing to investigate whether the different M-N-C sites in the bimetallic atomically dispersed catalysts work separately or whether there is an interaction between them like the alloy catalysts (Yin *et al.*, 2020). The objectives of the present study are to design bimetallic atomically dispersed catalysts and investigate the interaction between different metal sites and their contribution to the performance of ECO_2RR.

Here, we report a bimetallic catalyst with atomically dispersed Co and Fe sites for the highly efficient ECO_2RR for syngas production, which is our preliminary attempt to understand the interaction between Co and Fe and its contribution to the catalytic performance. The bimetallic catalysts are fabricated by using ZIF-8 as the precursor, which is a MOF that is tunable in metal nodes (Wang *et al.*, 2018a). The Co-ZIF is first constructed on the ZIF precursor, followed by the introduction of Fe. The introduction of Fe into Co-ZIF (Fe-Co-ZIF) creates the interaction between Co and Fe sites in the final carbonized catalysts (C-Fe-Co-ZIF-x, x is the adding amount of Fe (wt%) in the ZIF precursor). XPS illustrates that the introduction of Fe with the proper amount could increase the number of M-N sites in the catalyst, promoting the ECO_2RR performance. The interactions of different TMs in the bimetallic catalysts are indicated by XAS. It confirms that the coordination environment of Co is distorted by the addition of Fe in the bimetallic catalysts. Electrochemical measurements are carried out to investigate the catalytic performance of C-Fe-Co-ZIFs. C-Fe-Co-ZIF-1.6 wt%-Fe that has mild distortions in Co-N and Fe-N sites exhibits the best ECO_2RR performance towards CO production while maintaining the high total FE_{CO+H2} of around 93% for more than 10 hours. Cu-Co and Ni-Co bimetallic catalysts (carbonized Cu and

Ni-modified Co-ZIF) are confirmed to be able to promote ECO_2RR performance, demonstrating the versatility of the bimetallic SACs strategy. This work systematically investigates the interaction between different metals in bimetallic atomically dispersed catalysts for ECO_2RR, providing interesting insights into the design of the catalyst for the next generation.

4.2 Experimental section

4.2.1 Synthesis of Co-ZIF:

Typically, $Co(NO_3)_2 \cdot 6H_2O$ (0.546 g) and $Zn(NO_3)_2 \cdot 6H_2O$ (1.116 g) were dissolved in 40 mL of methanol. Then, 2-methylimidazole methanol solution (1.116 g in 40 mL) was slowly poured into the above solution under vigorous stirring, followed by subsequent stirring for 24 hours at room temperature. The as-obtained powders were collected by centrifugation at 7000 rpm for 5 minutes, washed three times with methanol, and finally dried in the oven at 90℃ overnight.

4.2.1 Synthesis of Fe-Co-ZIF with different Fe loadings:

The powder of as-prepared Co-ZIF (100 mg) was dispersed in methanol (10 ml) under ultrasound for 5 min at room temperature. After forming a homogeneous solution, $Fe(NO_3)_2 \cdot 9H_2O$ methanol solution (115 mg ml^{-1}, 50 μL for 0.8 wt% Fe, 100 μL for 1.6 wt% Fe, 200 μL for 3.2 wt% Fe, and 300 μL for 4.8 wt% Fe) $Fe(NO_3)_2 \cdot 9H_2O$) was injected into the mixed solution slowly under ultrasound for 2 min at room temperature. Next, the mix solution was under vigorous stirring for 5 h at room temperature to make the salt solution be absorbed completely. Then the samples were centrifuged and dried in the oven at 90℃ overnight.

4.2.2 Synthesis of C-Co-ZIF and C-Fe-Co-ZIFs:

The powder of as-prepared Co-ZIF and Fe-Co-ZIFs were placed in the tube furnace, maintained at three temperature plateaus (800 ℃, 900 ℃, and 1000 ℃, 1 hour for each) with a heating rate of 25 ℃ min^{-1} under flowing argon gas, and then naturally cooled to room temperature. All the as-prepared samples were directly used without any post-treatment.

4.2.3 Synthesis of C-Cu-Co-ZIF and C-Ni-Co-ZIFs:

The synthesis of C-Cu-Co-ZIF and C-Ni-Co-ZIFs follows the same procedure of C-Fe-Co-ZIF while replacing the $Fe(NO_3)_2$ methanol solution into the corresponding $Cu(NO_3)_2$ and $Ni(NO_3)_2$ methanol solution, respectively, during the ZIF preparation process.

4.2.4 Material characterizations

XRD patterns were collected on an X-ray diffractometer (Bruker D8 Advance) with a CuKα X-ray source (λ = 1.542 Å) and a scintillator detector. SEM images were obtained using a Focused Ion Beam And Scanning Electron Microscope (Tescan LYRA 3 XMH) at 20 kV. TEM was performed on a JEOL ARM200F operated at 200 kV. For atomic resolution imaging, the measurements were performed under HAADF-STEM mode. Samples for TEM were prepared by drop-drying the samples from their diluted ethanol suspensions onto carbon-coated copper grids. Inductively coupled plasma-optical emission spectrometry (ICP-OES) results were obtained by an Agilent 5100 ICP-OES. XPS experiments were undertaken on a VG Escalab 220i XL using monochromatic 1486.6 eV Al Kα radiation. The peak energies were calibrated by placing the graphite C1s peak at 284.8 eV. The spectra were fitted with mixed Gaussian-Lorentzian component profiles after a Shirley background subtraction by CasaXPS software. X-ray absorption spectroscopy including XANES and EXAFS at Co-K-edge and Fe-K-edge were collected in total-fluorescence-yield mode using a 32-element Ge detector at ambient condition on the HXMA beamline at the CLS. The XANES of N K-edge, Co L-edge, and Fe L-edge were measured in total X-ray electron yield mode at room temperature on the SGM beamline at CLS.

4.2.5 Electrochemical measurements

Catalyst electrodes were prepared by dropping the catalyst ink onto the carbon paper (Sigracet 25 BC) with a fixed area of 1 cm^2. The catalyst ink was prepared by mixing 0.5 mg of the catalyst powder, 120 µL of DI water, 120 µL of ethanol, and 2 µL of Nafion® perfluorinated resin solution (5 wt%, Sigma). The mixture was treated with ultrasound for 30 min and dropped onto the carbon paper on an 80℃ hot plate. The electrode was finally dried under 70℃ in an oven for further experiments.

CV was performed at the scan rate of 20 mV s^{-1}, LSV was performed at the scan rate of 5 mV s^{-1}, the chronoamperometry test, double-layer capacitance, and the EIS (performed at open circuit potential with a high frequency of 100000 and low frequency of 0.01) were carried out in a custom-made two-chamber H-type cell on a CHI 760D electrochemical workstation with the catalyst electrode as the working electrode. Working and reference electrodes were fixed in one chamber and the counter electrode was fixed in the other chamber. A proton exchange membrane (Nafion™ N115) separated the two chambers of the H-cell. The reference electrode was an Ag/AgCl electrode with a saturated KCl filling solution. The counter electrode was a Pt wire. Potential versus RHE was calculated as E vs. RHE = E vs. Ag/AgCl + 0.197 V + 0.0592 V × pH.

The pH values of CO_2 and N_2-saturated 0.5 M $KHCO_3$ electrolytes used in this work are 7.23 and 8.36, respectively. Unless notified elsewhere, the automatic iR compensation (80%) was applied to all the measurements.

4.3 Results and discussion

4.3.1 Preparation and characterization of catalysts:

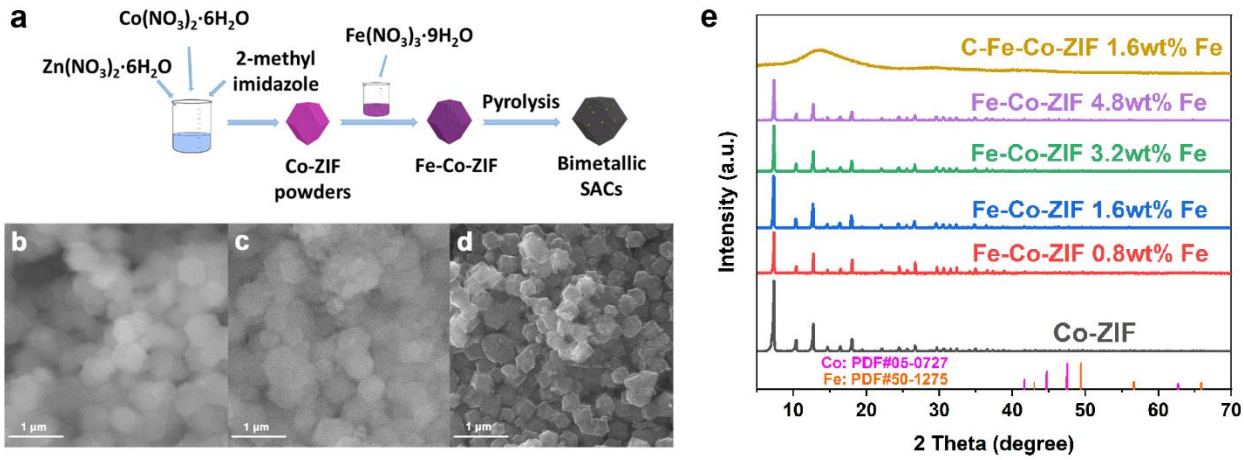

Figure 4.1 Structural characterization of C-Fe-Co-ZIF catalysts. (a) Fabrication schematic of the C-Fe-Co-ZIF catalysts; SEM images of (b) Co-ZIF. (c) Fe-Co-ZIF-1.6 wt%-Fe. (d) C-Fe-Co-ZIF-1.6 wt%-Fe at a scale bar of 1 μm. (e) XRD patterns of Fe-Co-ZIF series catalysts with different Fe adding amounts and the carbonized Fe-Co-ZIF-1.6 wt%-Fe (C-Fe-Co-ZIF).

The one-pot synthesis strategy of mixing all the ingredients led to a relatively small product yield (which could not be collected). The two-step synthesis method is employed to fabricate the atomically dispersed bimetallic catalysts. The synthetic procedure for the bimetallic Co-Fe catalysts is illustrated in **Figure 4.1a**. The Fe-Co-ZIF precursors are prepared with the impregnation method to modify ZIF-8 into Co-ZIF (Wang *et al.*, 2018a) and absorb the Fe source. Through this two-step synthesis method, the introduction of Fe does not interfere with the crystallization of Co-ZIF particles, resulting in the success of the yield of the bimetallic Fe-Co-ZIF precursors. Combined with the pyrolysis process to carbonize the ZIF particles and vaporization of Zn, atomically dispersed Co, Fe bimetallic catalysts are finally fabricated. SEM images reveal that the series of Fe-Co-ZIFs retain the morphology of the original Co-ZIFs with the various amount of Fe added in the synthesis **(Figures 4.1b, c, and Figure 9.1)**. After the pyrolysis process, the carbonized Fe-Co-ZIF (C-Fe-Co-ZIF) catalysts retain the morphology of Fe-Co-ZIFs **(Figures 4.1c and d)**. C-Fe-Co-ZIF also has better conductivity than ZIF precursors, providing

improved image quality in **Figure 4.1d** than in **Figures 4.1b, c**. XRD measurements show that Fe-Co-ZIFs keep the same crystalline structure as that of Co-ZIF, without any characteristic peak assigned to Co and Fe crystals. The absence of Co and Fe in XRD patterns can be due to the extremely low content of the metal element in the final catalysts (ICP indicates: 2.2 wt% of Co and 1.0 wt% of Fe in C-Fe-Co-ZIF-4.8 wt%-Fe). The XRD pattern of C-Fe-Co-ZIF **(Figure 4.1e)** demonstrates that the final bimetallic catalysts appear as amorphous carbon material.

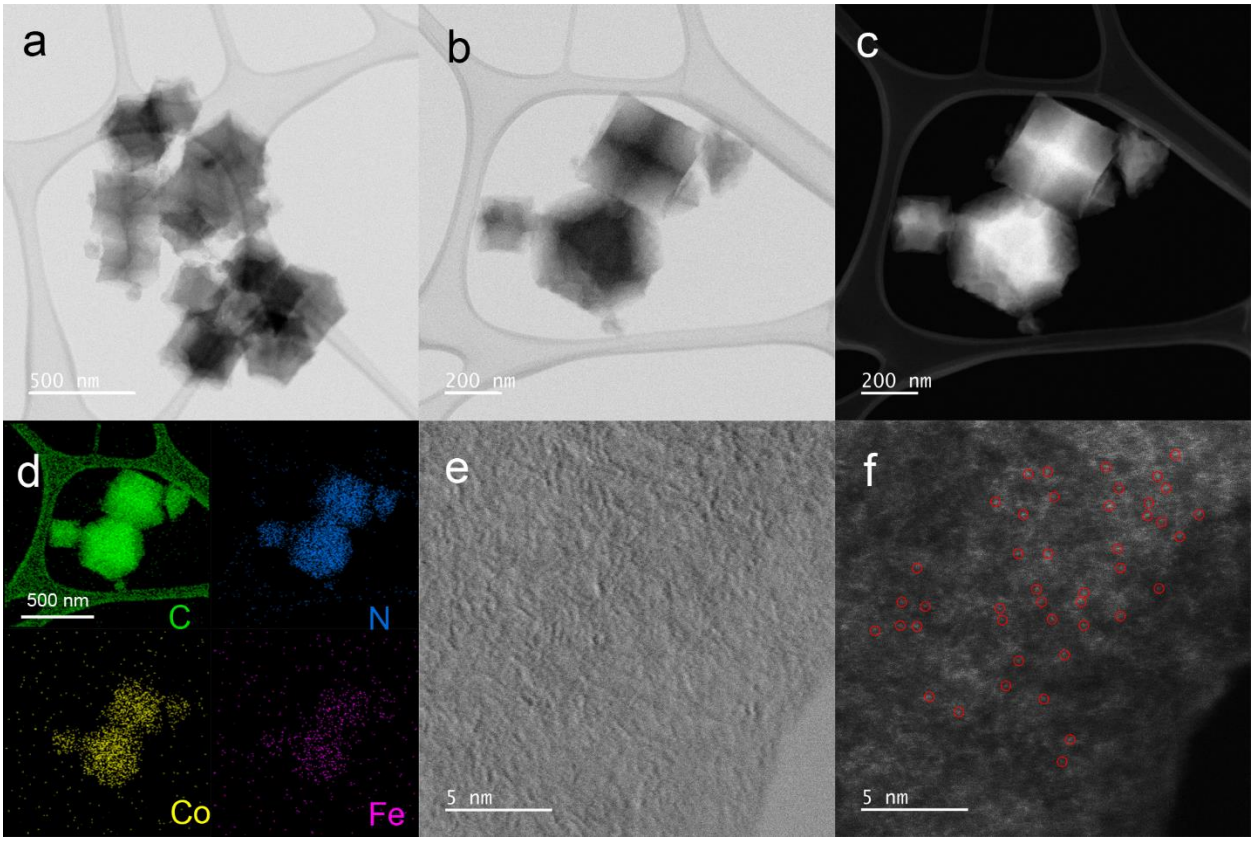

Figure 4.2 (a) and (b) TEM images. (c) HAADF-STEM images. (d) Elemental mapping images. (e) Magnified TEM images. (f) Atomic-resolution HAADF-STEM images of C-Fe-Co-ZIF-1.6 wt%-Fe powders.

TEM images show that the C-Fe-Co-ZIF particles are around 300 nm **(Figures 4.2a, b, and c)**, which agrees with the SEM results. The EDX spectroscopy elemental mappings depict the distributions of Co, Fe, C, and N, indicating that Co and Fe atoms are evenly distributed in C-Fe-Co-ZIF **(Figure 4.2d)**. Aberration-corrected high-angle annular dark-field scanning transmission electron microscopy (HAADF-STEM) with the sub-angstrom resolution is employed to directly observe the atomic dispersion of the metal atoms, benefiting from higher Z-contrast of Co and Fe than N and C **(Figures 4.2e and f)**. In **Figure 4.2f**, the single atom of Co and Fe (tiny bright spots)

are well dispersed in C-Fe-Co-ZIF 1.6 wt% Fe. To further demonstrate so, we have also conducted the X-ray absorption spectroscopy analysis, and indeed, we found the existence of the peaks for single-atom bindings in EXAFS (please see the corresponding discussion later on in this work). In short, the HAADF-TEM and EXAFS results are auxiliary to support the conception of single atoms in the catalysts. Other than atomically dispersed metal atoms, small metal clusters also are found in the bimetallic catalysts **(Figure 9.2)**. It illustrates the co-existence of the single-metal-atoms and metal clusters in the C-Fe-Co-ZIF.

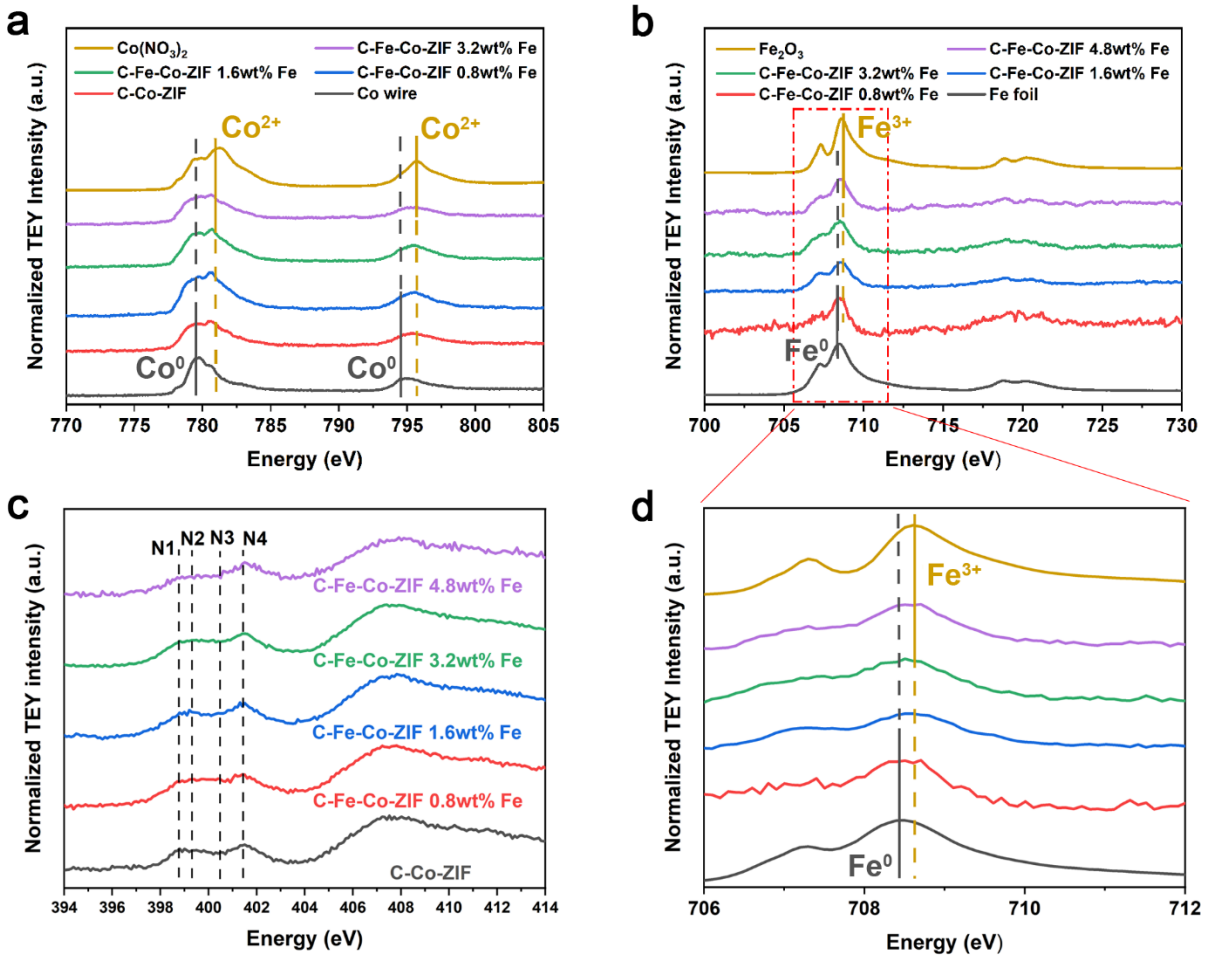

Figure 4.3 (a) Co L-edge XAS. (b) Fe L-edge XAS. (c) N K-edge XAS. (d) Enlarged Fe L-edge XAS of C-Fe-Co-ZIF samples.

Soft X-ray (metal L-edge) is attributed to the excitement of the 3d valence states. And the total electron yield mode (TEY) of metal L-edge is a surface-sensitive technique, which could be a more sensitive and direct probe for the metal oxidation states on the surface of the catalyst. The Co L-edge XAS is shown in **Figure 4.3a**. In the region at ca. 795 V, the peaks for C-Fe-Co-ZIF

are located between Co wire and $Co(NO_3)_2$. It suggests that the valences of Co atoms in C-Fe-Co-ZIF catalysts are between 0 to +2. There are two main peaks in the region from 778V to 782V. Co wire (Co^0) is dominated by the peak located before 780 V, while $Co(NO_3)_2$ (Co^{2+}) is dominated by the peak located after 780 V. All C-Fe-Co-ZIFs have relatively close intensity for these two peaks while the intensity of the peak after 780 V is slightly higher than that of the peak before 780 V, indicating the valences for the C-Fe-Co-ZIF samples are close to +2. Fe L-edge XAS in **Figure 4.3b** demonstrates that all the C-Fe-Co-ZIFs samples share the same peak pattern. The peak at ca. 707 eV and 709 eV can be ascribed to t_{2g} and e_g states, respectively (Sarveena *et al.*, 2016). The enlarged region in **Figure 4.3d** indicates that the valences of Fe atoms in C-Fe-Co-ZIF catalysts are between 0 to +3. The results agree well with previous literature that TMs in SACs are usually in an oxidation state (Pan *et al.*, 2018b; Zhang *et al.*, 2019b). Furthermore, N sites in the catalysts are investigated from N K-edge XAS **(Figure 4.3c)**. Two absorption edges at around 400 eV and 407 eV are corresponding to 1s→π* and 1s→σ* transitions, respectively (Schiros *et al.*, 2012). The wide peaks at ca. 407 eV show no obvious changes in all samples. In the 1s→π* edge, the peaks at ca. 401.5 eV (N4) appear for all the samples, which can be assigned to graphitic N. Almost all the samples reveal a plateau in the range from 398.5 eV to 400.5 eV, where peaks at ca. 398.8 eV (N1), 399.2 eV (N2), and 400.5 eV (N3) can be assigned to pyridinic N, metal-N bindings, and pyrrolic N, respectively (Gu *et al.*, 2019; Jin *et al.*, 2018). The graphitic N, pyridinic N, and pyrrolic N sometimes could facilitate the ECO_2RR process but are regarded as less effective than the metal-centered sites (Roy *et al.*, 2018; Zhang *et al.*, 2018b). The contents of metal-N binding directly reflect the property of M-Nx active sites in SACs, which are vital to catalytic reactions such as ECO_2RR (Chen *et al.*, 2021b; Lin *et al.*, 2019; Ren *et al.*, 2019b). C-Fe-Co-ZIF-1.6 wt%-Fe possesses the sharpest peak in the N2 region, which represents the optimal metal-N bindings. It implies the higher metal-N content of C-Fe-Co-ZIF-1.6 wt%-Fe than other samples.

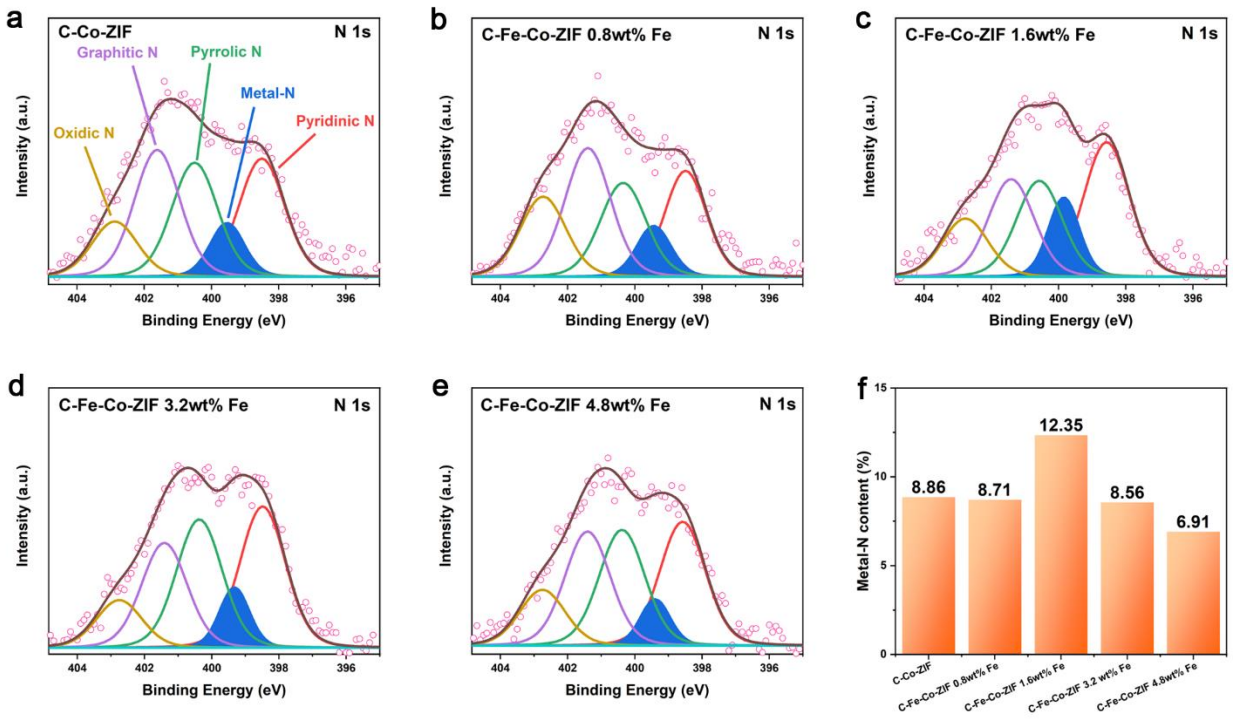

Figure 4.4 N 1s XPS of (a) C-Co-ZIF. (b) C-Fe-Co-ZIF-0.8 wt%-Fe. (c) C-Fe-Co-ZIF-1.6 wt%-Fe. (d) C-Fe-Co-ZIF-3.2 wt%-Fe. (e) C-Fe-Co-ZIF-4.8 wt%-Fe. (f) The percentage of metal-N content among N species of C-Fe-Co-ZIF samples.

XPS could characterize the specific species on the surface of the material. Although it is challenging to make accurate quantification, the combination of the two auxiliary techniques (e.g., XPS or XAS) can strongly support one opinion. Thus, we further verified the N K-edge results from XAS, by XPS. The XPS of N 1s in **Figures 4.4a-e** confirms the ascription of pyridinic N, metal-N, pyrrolic N, and graphitic N. Notably, The percentage comparison of metal-N content among all the N species for C-Fe-Co-ZIF in **Figure 4.4f** shows that the metal-N content increases significantly for C-Fe-Co-ZIF-1.6 wt%-Fe, which is consistent with the XAS results. It suggests that C-Fe-Co-ZIF-1.6 wt%-Fe could contain the maximum active sites for ECO_2RR. As the Fe content continuously increases in the catalyst precursor, however, the metal-N content decreases in the C-Fe-Co-ZIF. It is possibly due to the generation of the metal clusters when too much Fe is added, that the aggregation hinders the formation of metal-N bindings.

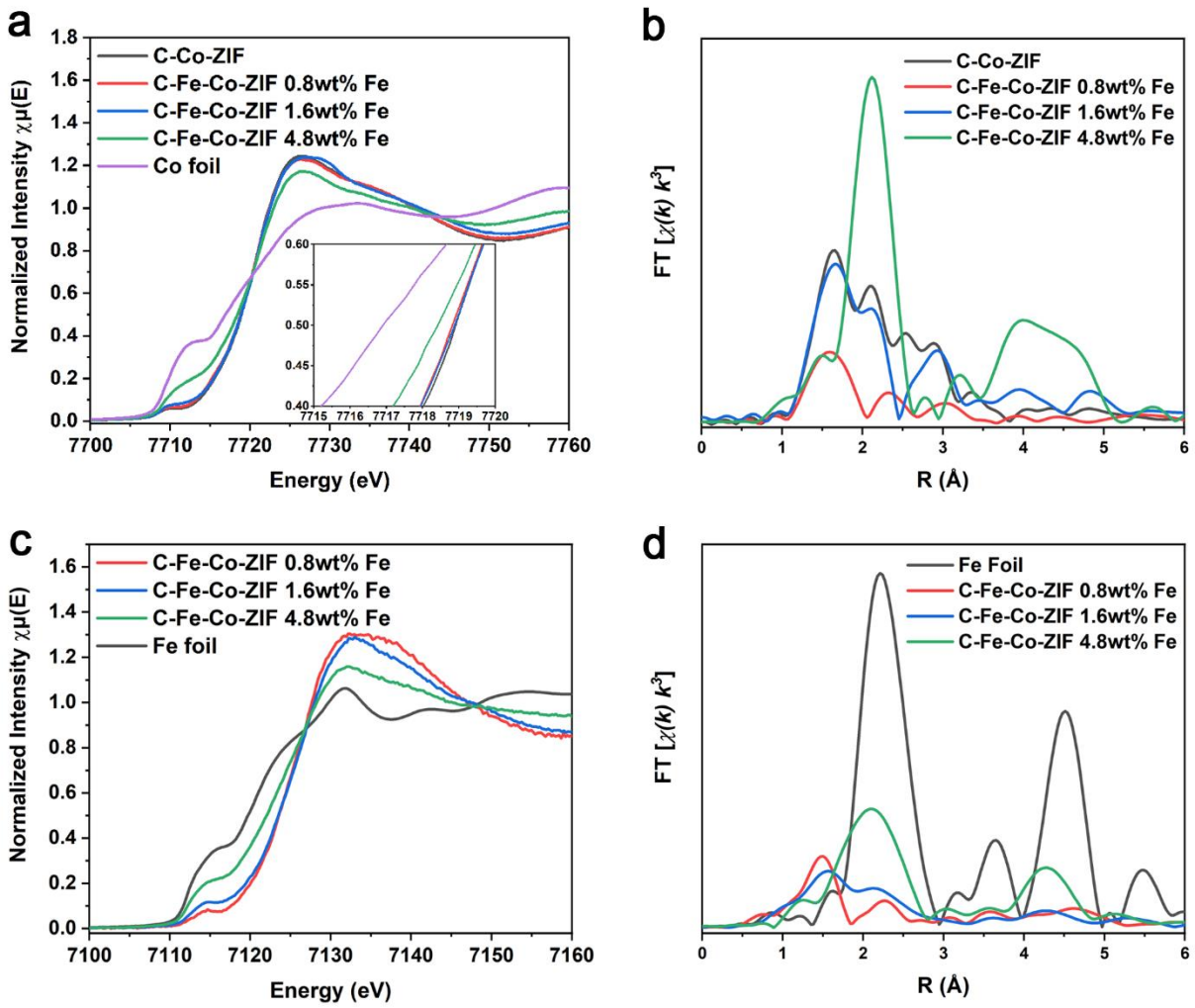

Figure 4.5 (a) Co K-edge XANES, inset: enlarged region of the white line. (b) Co EXAFS. (c) Fe K-edge XANES. (d) Fe EXAFS of C-Fe-Co-ZIF samples.

Hard X-ray (metal K-edge) that is bulk sensitive could not only provide information (XANES) on the metal oxidation states but also give insights into the local coordination environments (from EXAFS), which is essential for the SAC characterization. XANES of Co in **Figure 4.5a** further reveals that gradually increasing the introduction of Fe reduces the valence of Co in the catalysts (shift to the low energy side). The valences of Co atoms in C-Fe-Co-ZIF-0.8 wt%-Fe and 1.6 wt%-Fe are the closest to that of C-Co-ZIF. In addition, the pre-edge structure at ca. 7711 eV increases with the increase of Fe in the samples. This pre-edge peak belongs to the quadrupole electron transition of Co 1s to Co 3d, which reflects the density of empty Co 3d orbitals via hybridization (Mesilov *et al.*, 2017). For C-Fe-Co-ZIF-4.8 wt%-Fe, the pre-edge peak shifts towards that of the Co foil. During the synthesis, only a small amount of Fe is added to Co-ZIF. It is not likely that Co particles are formed because of the increasing metal content of Fe in the final catalyst. Thus, the

increased intensity of the pre-edge peak indicates that the adding of Fe affects the electronic structure of Co. The XANES pattern tends to be close to that of Co foil when the Fe content is increased. It implies that Co elements are gradually turning into metallic states with the addition of Fe.

EXAFS is conducted to investigate the coordination environment of Co sites. As shown in **Figure 4.5b**, C-Co-ZIF exhibits a prominent peak at ca. 1.6 Å, which can be ascribed to the Co-N, Co-O, and Co-C coordination, indicating the single-atom state of Co atoms. Several previous studies confirm that metal-N bonds dominate similarly to the peak in ZIF-8-derived SACs (Ren *et al.*, 2019b; Wang *et al.*, 2018a; Yang *et al.*, 2021). Combined with the XPS results, this peak could be plausibly assigned to Co-N bindings. The peak at ca. 2.1 Å is close to the main peak of Co foil **(Figure 9.3)**, which can be ascribed to metal-metal bindings, i.e., the Co-Co coordination. It indicates that C-Co-ZIF consists of atomically dispersed Co atoms as well as Co clusters, which agrees with the TEM. With a relatively small amount of Fe, the EXAFS *R* space of C-Fe-Co-ZIF-0.8 wt%-Fe shows a dramatic decrease in peak intensities, implying either the significant decrease of coordination number or the intense distortion of the coordination environment of Co atoms. The main peaks of C-Fe-Co-ZIF-0.8 wt%-Fe are located at ca. 1.5 Å and ca. 2.3 Å, which is not identical to that of C-Co-ZIF. It suggests that the Fe atoms greatly affect the coordination environment of Co sites in C-Fe-Co-ZIF-0.8 wt%-Fe. With the increase of Fe content, the *R* space peaks of C-Fe-Co-ZIF-1.6 wt%-Fe tend to be similar to those of C-Co-ZIF with different intensities of the main peaks. It indicates that in the C-Fe-Co-ZIF-1.6 wt%-Fe the coordination environment of Co sites is less affected by the introduction of Fe. With large content of Fe, C-Fe-Co-ZIF-4.8 wt%-Fe exhibits a prominent peak at ca. 2.1 Å that belongs to metal-metal bindings, ascribed to Co-Fe or Fe-Fe coordination. The large amount of Fe could greatly affect the coordination environment of Co sites (C-Fe-Co-ZIF-4.8 wt%-Fe).

The above methodology is applied for the analysis of Fe atoms. XANES of Fe in **Figure 4.5c** reveals that the gradually increased amount of Fe reduces the valence of Fe in the catalysts, while the valences of Fe in C-Fe-Co-ZIF-0.8 wt%-Fe and C-Co-ZIF-1.6 wt%-Fe are similar. The near edge structure at ca. 7115 eV is assigned to 1s to 3d transitions (Chen *et al.*, 2020b). With the increasing adding amount of Fe, the XANES tends to become similar to that of Fe foil, implying the agglomeration of Fe atoms. The coordination environment of Fe sites is investigated by EXAFS **(Figure 4.5d)**. The prominent peak at ca. 1.5 Å of C-Fe-Co-ZIF-0.8 wt%-Fe is ascribed to Fe-N bindings (similar interpretation as Co-N), indicating the dominant single-metal-atom state of Fe atoms. With the increasing amount of Fe, the dominant Fe-N peak for C-Fe-Co-ZIF-1.6 wt%-

Fe shifts a little to ca. 1.6 Å with a decreased intensity, indicating the distortion to the coordination environment of Fe-N in the catalyst. The peaks at ca. 2.1 Å are observed for C-Fe-Co-ZIF-1.6 wt%-Fe and C-Fe-Co-ZIF-4.8 wt%-Fe. This peak location is not identical to the Fe-Fe binding of Fe foil (2.2 Å) but the same as the one in the previous Co *R* space analysis **(Figure 4.5b)**, supporting the assumption of the Co-Fe coordination in the Fe-Co bimetallic catalyst samples.

4.3.2 Catalytic performance of the C-Fe-Co-ZIFs for ECO_2RR:

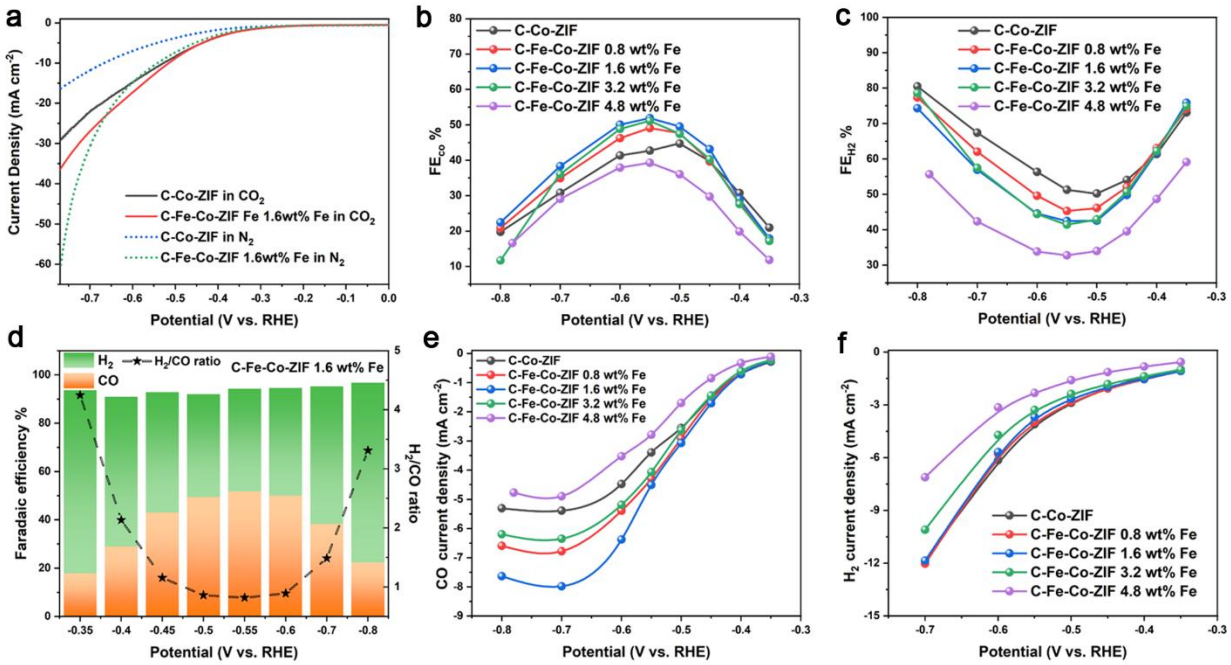

Figure 4.6 The evaluation of the electrocatalytic performance of the samples. (a) LSV curves of C-Co-ZIF and C-Fe-Co-ZIF-1.6 wt%-Fe in N_2 or CO_2-saturated 0.5 M $KHCO_3$ solution at a scan rate of 5 mV s^{-1}. (b) CO Faradaic efficiency of the catalysts at various applied potentials. (c) H_2 Faradaic efficiency of the catalysts at various applied potentials. (d) Bars: FE_{CO} and FE_{H2}; Stars: H_2/CO ratio of C-Fe-Co-ZIF-1.6 wt%-Fe at various applied potentials. (e) CO current density of the catalysts. (f) H_2 current density of the catalysts.

The ECO_2RR evaluations are performed in a custom-made H-cell. Several cycles of CV are pre-run before the electrochemical measurements to stabilize the catalyst electrode. Both CV curves in N_2 and CO_2 atmospheres for different C-Fe-Co-ZIF catalysts are measured **(Figure 9.4)**. LSV curves of C-Fe-Co-ZIF-1.6 wt%-Fe are better than those of the pure C-Co-ZIF, in both N_2 and CO_2 atmospheres **(Figure 4.6a and Figure 9.4)**. Compared to the LSV curve in N_2, C-Fe-Co-ZIF-1.6 wt%-Fe shows an enhanced current response in the CO_2 atmosphere in the range of around -0.35 V to -0.65 V vs. RHE. The crossing of CV curves in N_2 and CO_2 indicates the production rates of CO and H_2 are dependent, implying the tunable ratio of CO/H_2 by adjusting the potential.

FE results in **Figure 4.6b and c** reveal that FE_{CO} and FE_{H2} are in the opposite trend for all the catalysts. C-Fe-Co-ZIF-0.8 wt%-Fe, C-Fe-Co-ZIF-1.6 wt%-Fe, and C-Fe-Co-ZIF-3.2 wt%-Fe exhibit higher FE_{CO} and lower FE_{H2}, compared to those of C-Co-ZIF, indicating the promoted CO production in the Co, Fe bimetallic catalyst during the ECO_2RR process. C-Fe-Co-ZIF-1.6 wt%-Fe and C-Fe-Co-ZIF-3.2 wt%-Fe have similar FE_{CO} and FE_{H2}, with FE_{CO} of around 52% (about 10% higher than that of pure C-Co-ZIF) and FE_{H2} around 42% at -0.55 V vs. RHE. The ratio of H_2/CO can be tuned from 0.8 to 4.2 at different potentials while maintaining the total FE_{CO+H2} above 90% **(Figure 4.6d)**. Most of the C-Fe-Co-ZIFs exhibit a higher CO current than that of C-Co-ZIF. C-Fe-Co-ZIF-1.6 wt%-Fe has the highest CO current density of 8.0 mA cm^{-2} at -0.7 V vs. RHE **(Figure 4.6e)**. Negligible CO is detected under the controlled electrochemical experiments (in the N_2 atmosphere), confirming the direct CO production from the gaseous CO_2 during ECO_2RR. The H_2 current densities of C-Fe-Co-ZIF-0.8 wt%-Fe and C-Fe-Co-ZIF-1.6 wt%-Fe are very close to that of C-Co-ZIF while C-Fe-Co-ZIF-3.2 wt%-Fe and C-Fe-Co-ZIF-4.8 wt%-Fe exhibit decreased H_2 current densities **(Figure 4.6f)**. Notably, C-Fe-Co-ZIF-4.8 wt%-Fe shows decreases in the production activity in both CO and H_2 with a total FE_{CO+H2} of around only 70% **(Figure 9.5)**, implying the more added amount of Fe possibly leads to other product formations instead of CO and H_2.

The chronoamperometry of C-Fe-Co-ZIF-1.6 wt%-Fe in **Figure 4.7a** shows that, during the 10 hours of reaction, the total current density drops quickly (10% drop) in the first hour. Then, the decay of the current density is relatively stable, with the maintenance of over 85% of the initial current density for 9 hours. The explosion of the gas bubbles generated on the catalyst electrode during the reaction could cause the cliffs in the current curve. **In Figure 4.7b** that the FE of CO remains stable for more than 10 hours at 52-53% as well as the FE of H_2 at around 40%, which is better than several hours presented in many published reports (Dong *et al.*, 2019; He *et al.*, 2019; Wang *et al.*, 2019a; Woyessa *et al.*, 2021).

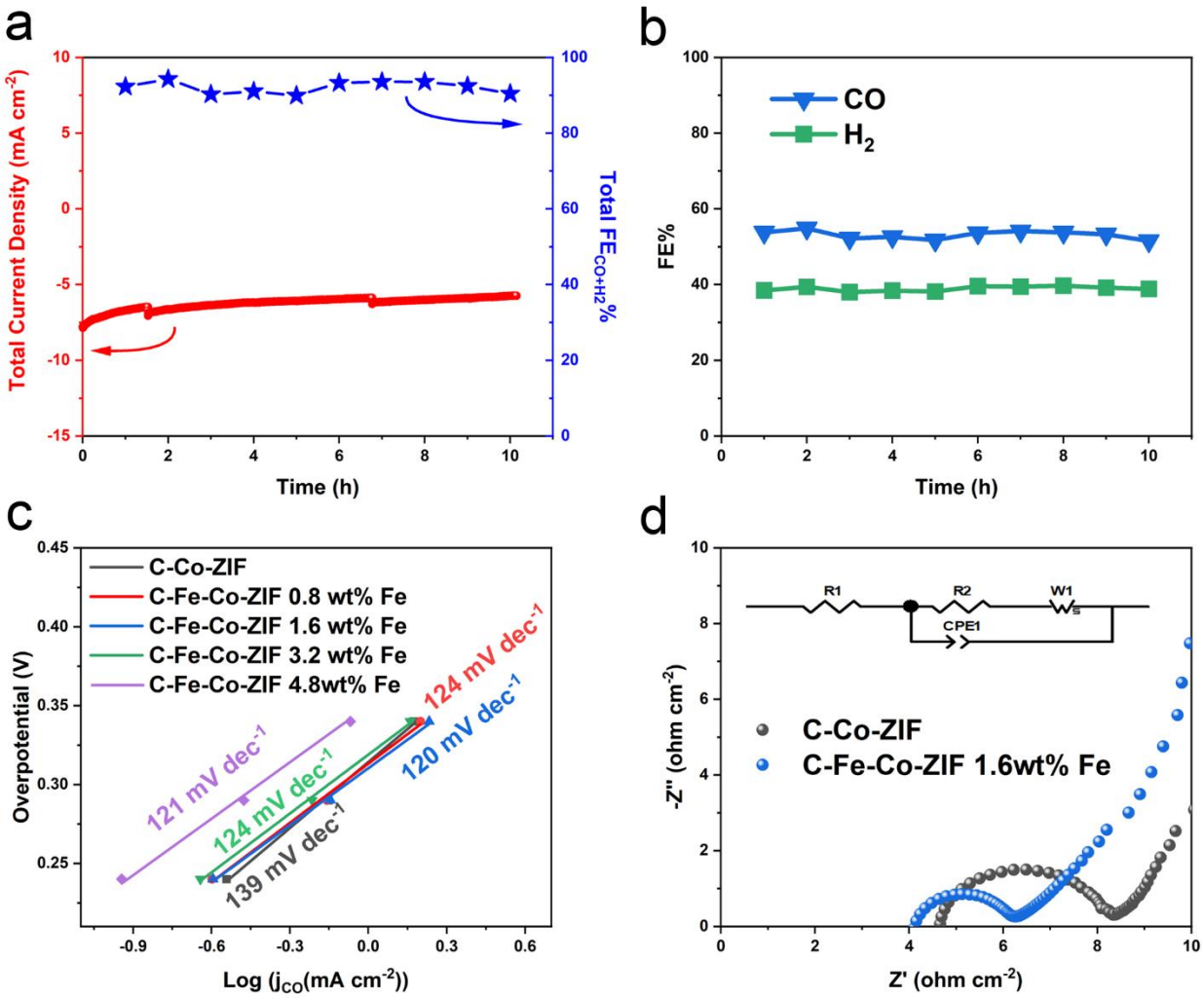

Figure 4.7 The chronoamperometry test of (a) Total current density and total FE_{CO+H2}. And (b) FE_{CO} and FE_{H2} of C-Fe-Co-ZIF-1.6 wt%-Fe at -0.55 V vs. RHE under CO_2 atmosphere for the stability evaluation. (c) Tafel slopes of C-Fe-Co-ZIF catalyst electrodes with different Fe adding amounts. (d) EIS results of C-Co-ZIF and C-Fe-Co-ZIF-1.6 wt%-Fe.

4.3.3 Mechanism investigation:

C-Fe-Co-ZIF-1.6 wt%-Fe has the best CO production activity of ECO_2RR. We compare the Tafel slope values to gain insights into the CO formation during ECO_2RR. The schematic of bimetallic Fe-Co catalysts for ECO_2RR is illustrated in **Figure 4.8**. Tafel slopes of C-Fe-Co-ZIF catalysts are similar in **Figure 4.7c**, of around 120 mV dec^{-1}, which is close to the theoretical value of 118 mV dec^{-1} for the first electron-transfer step, suggesting the first electron-transfer step ($CO_2 + e^- \rightarrow CO_2^{*-}$ or $CO_2 + e^- + H^+ \rightarrow {}^*COOH$) could be the rate-decided step (Gu *et al.*, 2019). Compared to the original C-Co-ZIF has a value of 139 mV dec^{-1} (much higher than that of C-Fe-Co-ZIF catalysts, **Figure 9.6**), the improvement of the CO production in ECO_2RR is caused by the adding

of Fe for C-Fe-Co-ZIF catalysts. The more positive initial point of the Tafel slope represents the higher current density. With the increased added amount of Fe in the catalyst (C-Fe-Co-ZIF-4.8 wt%-Fe), the initial point of the Tafel slope shifts significantly towards a negative value, indicating decreased production rate of CO. The double-layer capacitance is employed to estimate the ECSA of different catalyst electrodes **(Figure 9.7)**. Except for C-Fe-Co-ZIF-4.8 wt%-Fe which has a decreased ECSA, all the other C-Fe-Co-ZIF possess similar ECSA as C-Co-ZIF, implying the enhancement of the CO production for C-Fe-Co-ZIF catalysts comes from the intrinsic properties of the bimetallic catalysts. The TOF of the catalysts is calculated based on **Equation 1.16**, as shown in **Table 4.1**. At -0.7 V vs. RHE, C-Fe-Co-ZIF catalysts show higher TOF_{CO} values than that of C-Co-ZIF, which agrees with the Tafel slope results. In the meantime, C-Fe-Co-ZIF-0.8 wt%-Fe has the highest TOF_{CO} and TOF_{H2} values among all the catalysts, indicating the strong interaction between Fe and Co atoms (see the previous discussion of XAS) in the catalysts that can promote the CO and H_2 productions during ECO_2RR.

Table 4.1 TOF of the catalysts at -0.7 V vs. RHE

	C-Co-ZIF	C-Fe-Co-ZIF-0.8 wt%-Fe	C-Fe-Co-ZIF-1.6 wt%-Fe	C-Fe-Co-ZIF-3.2 wt%-Fe
TOF_{CO} $(site^{-1}s^{-1})$	0.91	1.3	1.2	1.1
TOF_{H2} $(site^{-1}s^{-1})$	2.0	2.3	1.8	1.8

Consistently to all characterizations, C-Fe-Co-ZIF-1.6 wt%-Fe exhibits both increased M-N sites and mild distortions in coordination environments of Co-N and Fe-N, leading to the optimum ECO_2RR performance. The EIS (**Figure 4.7d and Figure 9.8**) reveals that C-Fe-Co-ZIF-1.6 wt%-Fe exhibits an almost 2 times lower charge-transfer resistance than that of C-Co-ZIF (2.085 Ω and 3.691 Ω for C-Fe-Co-ZIF-1.6 wt%-Fe and C-Co-ZIF, respectively, **Figure 9.8 and Table 9.1**). The facilitated CO_2 activation, increased number of M-N sites, and high charge transfer rate attribute to the improved ECO_2RR performance for Fe-Co-ZIF catalysts (Figure 4.8).

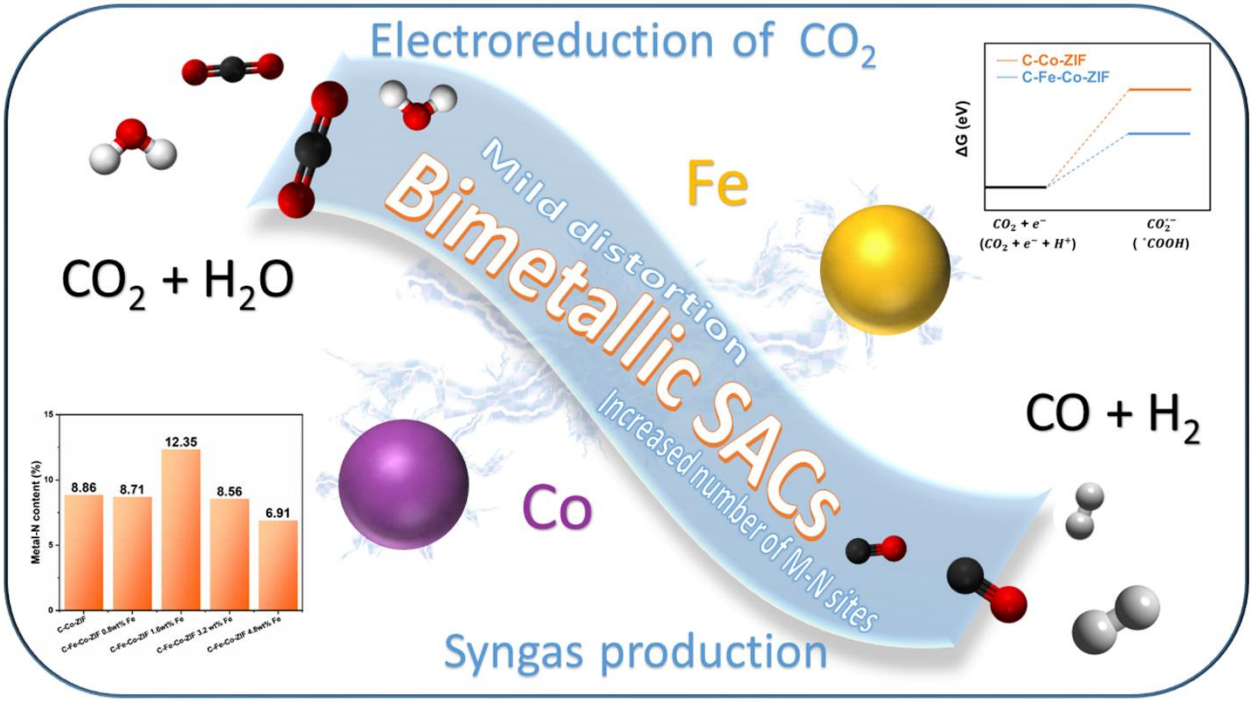

Figure 4.8 The schematic reaction mechanism of bimetallic catalysts for ECO_2RR.

4.3.4 Applications of C-Cu-Co-ZIFs and C-Ni-Co-ZIFs for ECO_2RR:

A series of Cu-Co and Ni-Co bimetallic catalysts based on the same strategy of C-Fe-Co-ZIFs are synthesized to verify the versatility of the atomically dispersed bimetallic method of TM elements in ECO_2RR. The Cu-Co-ZIFs/carbonized Cu-Co-ZIF (C-Cu-Co-ZIF) and Ni-Co-ZIFs/carbonized Ni-Co-ZIF (C-Ni-Co-ZIF) have the same morphology and crystalline structure as that of Fe-Co-ZIF/C-Fe-Co-ZIF **(Figures 9.9 and S10)**. The interactions between Cu and Co or Ni and Co are confirmed by XANES and EXAFS **(Figure 9.11)**. Similar to C-Fe-Co-ZIF samples, C-Cu-Co-ZIF samples also exhibit a positive enhancement in CO production **(Figure 9.12)**. C-Cu-Co-ZIF-3.2 wt%-Cu exhibits the FE_{CO} of around 51% and FE_{H2} of around 37% at -0.55 V vs. RHE. The CO current density reaches 8.3 mA cm-2 at -0.7 V vs. RHE. In contrast, C-Ni-Co-ZIF reveals a negative impact on CO production **(Figure 9.13)**. C-Ni-Co-ZIF-3.2 wt%-Ni exhibits the FE_{CO} of around 35% and FE_{H2} of around 29% at -0.55 V vs. RHE. The CO current density reaches 4.7 mA cm-2 at -0.7 V vs. RHE. It is noted that the total FE_{CO+H2} of C-Ni-Co-ZIF does not reach over 70%, indicating a possibly large amount of product formations other than CO and H_2 **(Figure 9.13d)**. It implies that C-Ni-Co-ZIF samples could be more suitable for other CO_2RR product generations than for syngas production.

4.4 Conclusion

Atomically dispersed Fe-Co bimetallic catalysts are fabricated by introducing Fe into Co-ZIF along with the pyrolysis. The Fe-Co bimetallic catalysts show good catalytic activity towards syngas production from ECO_2RR, with tunable CO/H_2 ratios. C-Fe-Co-ZIF-1.6 wt%-Fe exhibits the highest FE_{CO} of 51.9% and FE_{H2} of 42.4% at -0.55 V vs RHE, where the FE_{CO} is significantly increased (around 10% higher than that of pure C-Co-ZIF). The H_2/CO ratio is tunable in a wide range from 0.8 to 4.2 while maintaining the total FE_{CO+H2} as high as 93% for more than 10 hours. XAS technique greatly benefits the characterization of the bimetallic atomically dispersed Fe-Co catalysts. N K-edge and metal L-edge provide insights into N species and metal oxidation states in the catalysts. Metal K-edge offers detailed information on the coordination environments of the metal atoms. It confirms that the addition of Fe would interfere with the local coordination environment of Co in bimetallic catalysts and C-Fe-Co-ZIF-1.6 wt%-Fe has mild distortions in Co and Fe coordination environments. The proper amount of Fe in C-Fe-Co-ZIF-1.6 wt%-Fe increases the number of M-N sites and creates mild distortions in the local coordination environment of the metal sites, which is the key reason for the best CO production performance in ECO_2RR among all the C-Fe-Co-ZIF samples. The excessive adding of Fe results in other product generation than CO and H_2. Applied with the same strategy, atomically dispersed Cu-Co bimetallic catalysts also exhibit positive results on CO production for the syngas generation, while atomically dispersed Ni-Co bimetallic catalysts facilitate other product generations than syngas. The present results demonstrate the synergistic effects concerning the metal combination and the interactions between different metal atoms should be considered for the design of atomically dispersed TM bimetallic catalysts in ECO_2RR.

5 Chapter 5 The iron single-atom catalysts with the atomic layer deposition modification for the enhanced carbon dioxide electroreduction

Motivation

From Chapter 4, we learned that the introduction of Fe into Co-SAC to form Fe-Co SACs can significantly improve the ECO_2RR performance. It inspires the exploration of pure Fe-SACs for ECO_2RR. Pure Fe SAC such as FeNC catalyst is well known for its promising catalytic performance in the fuel cell industry. (Chenitz *et al.*, 2018; Zhang *et al.*, 2019b) The ZIF-template method also happens to be the commonly used approach to fabricate FeNC. (Yang *et al.*, 2020d; Yang *et al.*, 2020e) Combined with the porosity strategy developed in Chapter 3, we intend to fabricate a FeNC catalyst to test its ECO_2RR performance.

ALD is capable of the synthesis of the ultrathin coating layer of the different functional materials with atomic-level precision. By ALD, the various structures such as the nanoparticles and the nanoislands with tunable structural properties for functional applications can be prepared. As discussed in Chapter 1, the ALD-prepared materials can participate in the design of the catalysts in different ways such as the main catalysts, the stabilizers, and the connections in between. The active nanocatalysts fabricated by ALD can form in the particle size ranges from several angstroms to several nanometers, which increases active sites more than the bulk nanoparticles with the same effective mass. The super small active layers and particles deposited by ALD usually demonstrate a strong interaction with the substrate catalyst to strengthen the effect of the homo- or heterojunctions, resulting in the enhancement of the catalytic performance. For CO_2RR, TiO_2 and Al_2O_3 are commonly used as the over coatings on the active catalysts, which can be helpful to the duration issue of ECO_2RR. (Chen *et al.*, 2019) In this case, we also propose to apply ALD coating layers on FeNC for improving the catalytic stability.

5.1 Introduction

Numerous pieces of research confirm that the $M\text{-}N_x$ structure plays a vital role as the active site for ECO_2RR. (Cho *et al.*, 2022; Song *et al.*, 2023; Wang *et al.*, 2023) Our previous research confirms that the introduction of Fe single-atom active sites can promote the ECO_2RR performance toward CO production in a bimetallic Co-Fe SAC. Recent reports also demonstrate that FeNC catalysts with Fe single-atom active sites exhibit high CO production activity in ECO_2RR.(Li *et al.*, 2022; Pan *et al.*, 2020; Vijay *et al.*, 2020) Our group happens to have rich

experience in FeNC fabrication.(Wei *et al.*, 2018; Yang *et al.*, 2020d; Yang *et al.*, 2020e; Zhang *et al.*, 2019b) Aiming to construct the catalyst with better FEco, we further investigate the ECO_2RR performance of the FeNC catalyst. As aforementioned in chapter 1, the ALD technique emerges as a powder tool to fabricate catalysts with atomic precision and is a desirable approach to deposit ultra-thin films on the catalyst, which could contribute a lot to the catalytic activity and stability enhancement.

Various techniques can fulfill the fabrication of thin films such as chemical vapor deposition (CVD), layer deposition, spin coating, sol-gel synthesis, and ALD.(Chrisey *et al.*, 2003; Knapp *et al.*, 2016; Xiao *et al.*, 2016) However, when it comes to ultra-thin film fabrication with great conformality and uniformity, ALD stands out among these techniques. As aforementioned, ALD provides the uniform and conformal deposition of the material, and the thickness of the ALD layer can be precisely controlled at the atomic level by adjusting the number of reaction cycles, which offers exquisite construction of the material composition and structure. For complex material structures with deep holes, trenches, and pores, ALD is capable of producing uniform coatings all over the surface of the material with layer thickness from sub nanometers to several nanometers. (Lim *et al.*, 2003) Besides, to fabricate a complex fine structure, some catalysts are prepared by multiple steps. A relatively high operating temperature in the subsequent steps might deactivate the active junctions formed in the pre-synthesized catalyst. In this case, the mild synthetic condition of ALD (low temperature) ascertains the performance conversation of the substrate catalyst. For example, the ALD-TiO_2 protective layer has been proved to improve the corrosion-resistant property of the Si photocathode. In the meantime, the ALD deposition temperature of 150℃ barely affected the CO_2 reduction performance of the Si photocathodes. (Li *et al.*, 2019) One major drawback of ALD is the limited deposition rate. Normally, the deposition rate of ALD is less than half a monolayer (< 0.2 nm) per cycle.(Leskelä *et al.*, 2002) But with the proper selection of the synthetic parameters such as precursors and temperature, it is possible to accelerate the deposition rate. Gordon et al. reported that, with the suitable tuning of the dose size and the operating temperature, alternating surface reactions of trimethylaluminum and tris(tert-butoxy)silanol vapors could fabricate the silica nanolaminates of > 32 atomic layers per ALD cycle.(Hausmann *et al.*, 2002) Moreover, the ALD process is highly depend on the precursors. A successful deposition by ALD requires specific vaporous precursors corresponding to the target compound, which are mostly organic chemicals.(Prakash *et al.*, 2019) With the continuous development of ALD technique nanomaterials and advanced nanotechnology, more and more precursors are found to be applicable in the ALD process. To our advantage, the coating layers on the SACs are intended to be ultra-thin so that they would not block the active sites of the

catalyst during CO_2RR. It only requires a few cycles numbers (~>100) during ALD process to produce ultra-thin layers, which means the expeditious synthetic routine for ALD layer coatings on the catalyst.

In this work, we fabricated the FeNC catalyst with the re-fined synthetic method. The prepared FeNC exhibited the maximum FEco of around 76%, which is much higher than those of the C-Co-ZIF HM 15 min and C-Fe-Co-ZIF presented in Chapter 3 and Chapter 4, respectively. Combined with the ALD technique, we modified the FeNC catalyst with different ALD-Al_2O_3 cycles. It turned out that the small cycle number of ALD-Al_2O_3 could slightly promote the FEco of FeNC in ECO_2RR and perfectly prevent FeNC from the aging issue. It demonstrates the positive potential of ALD modification on the SAC for ECO_2RR. With the profound investigation in the future (e.g. different ALD material modifications such as TiO_2, CoO, and NiO), the catalytic activity and stability of SAC on ECO_2RR could be further enhanced.

5.2 Experimental section

5.2.1 Synthesis of $Fe(phen)_3^{2+}$ loaded ZIF-8:

1,10-phen solution (100 mg in 50 mL of ethanol/DI water mixture) was mixed with the FeAc solution (32 mg in 25 ml DI water) under vigorous stirring. Then, ZIF-8 solution (800 mg in 50 mL of ethanol) was added, followed by subsequent stirring for 2 hours at room temperature. The as-obtained solution was dried in the oven at 90 ℃ overnight.

5.2.2 Synthesis of FeNC:

The obtained $[Fe(phen)_3]^{2+}$ loaded ZIF-8 was ground by the ball-milling method at 400 rpm for 3 h. The ground powder was then transferred into a quartz tube to perform pyrolysis under Ar protection at 1050 ℃ for 1h.

5.2.3 Synthesis of ALD-Al_2O_3-FeNC:

The prepared FeNC was put in a homemade container with a mesh top to allow the interaction of ALD precursor gases with the sample. ALD process was conducted in a GEMStar XT™ (Arradiance Inc.). The precursors to deposit Al_2O_3 are trimethylaluminum ($Al_2(CH_3)_6$, TMA) and H_2O. TMA precursor was pre-heated at 70 °C. The ALD chamber temperature was 250 °C during the ALD process. The ALD-Al_2O_3 deposition routine is as followed: exposure time for TMA was 60 mS; Exposure time for H_2O: 60 mS. Purge flow: Ar 40 SCCM. The number of cycles: 5, 10,

25, 100. The prepared samples are named X ALD-Al_2O_3 FeNC (X is the ALD cycle number used during the ALD process).

5.2.1 Material characterizations

TEM was performed on a JEOL ARM200F operated at 200 kV. For atomic resolution imaging, the measurements were performed under HAADF-STEM mode. Samples for TEM were prepared by drop-drying the samples from their diluted ethanol suspensions onto carbon-coated copper grids. X-ray absorption spectroscopy including XANES and EXAFS at Fe K-edge were collected in total-fluorescence-yield mode using a 32-element Ge detector at ambient condition on the HXMA beamline at the CLS.

5.2.2 Electrochemical measurements

Catalyst electrodes were prepared by dropping the catalyst ink onto the carbon paper (Sigracet 25 BC) with a fixed area of 1 cm^2. The catalyst ink was prepared by mixing 0.5 mg of the catalyst powder, 120 µL of DI water, 120 µL of ethanol, and 2 µL of Nafion® perfluorinated resin solution (5 wt%, Sigma). The mixture was treated with ultrasound for 30 min and dropped onto the carbon paper on an 80 ℃ hot plate. The electrode was finally dried under 70 ℃ in an oven for further experiments.

CV was performed at the scan rate of 20 mV s^{-1}), LSV was performed at the scan rate of 5 mV s^{-1}), and the chronoamperometry test was carried out in a custom-made two-chamber H-type cell on a CHI 760D electrochemical workstation with the catalyst electrode as the working electrode. Working and reference electrodes were fixed in one chamber and the counter electrode was fixed in the other chamber. A proton exchange membrane (Nafion™ N115) separated the two chambers of the H-cell. The reference electrode was an Ag/AgCl electrode with a saturated KCl filling solution. The counter electrode was a Pt wire. Potential versus RHE was calculated as E vs. RHE = E vs. Ag/AgCl + 0.197 V + 0.0592 V × pH. The pH values of CO_2 and N_2-saturated 0.5 M $KHCO_3$ electrolytes used in this work are 7.23 and 8.36, respectively. Unless notified elsewhere, the automatic iR compensation (80 %) was applied to all the measurements.

5.1 Results and discussion

5.1.1 Preparation and characterization of catalysts:

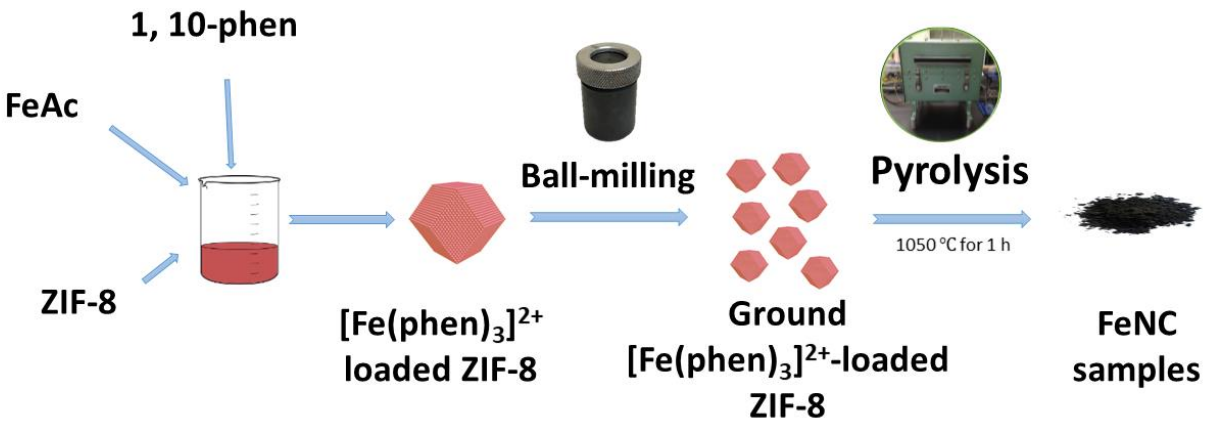

Figure 5.1 Fabrication schematic of the FeNC catalyst.

Based on the experience of FeNC fabrication with our group, **Figure 5.1** illustrates the synthetic procedure of FeNC. $[Fe(phen)_3]^{2+}$ is used as the Fe source loaded on ZIF-8 for a better distribution of Fe in the substrate. Combined with ball-milling and pyrolysis, the final FeNC catalyst is prepared. TEM results in **Figures 5.2a and b** demonstrate that there are no visible metal particles formed in FeNC. The XANES and EXAFS spectra from XAS in **Figures 5.2c and d** also confirm the SAC properties of FeNC (positive charged), with a typical Fe-N bonding presented in EXAFS. These results validate our synthetic method for FeNC SAC fabrication.

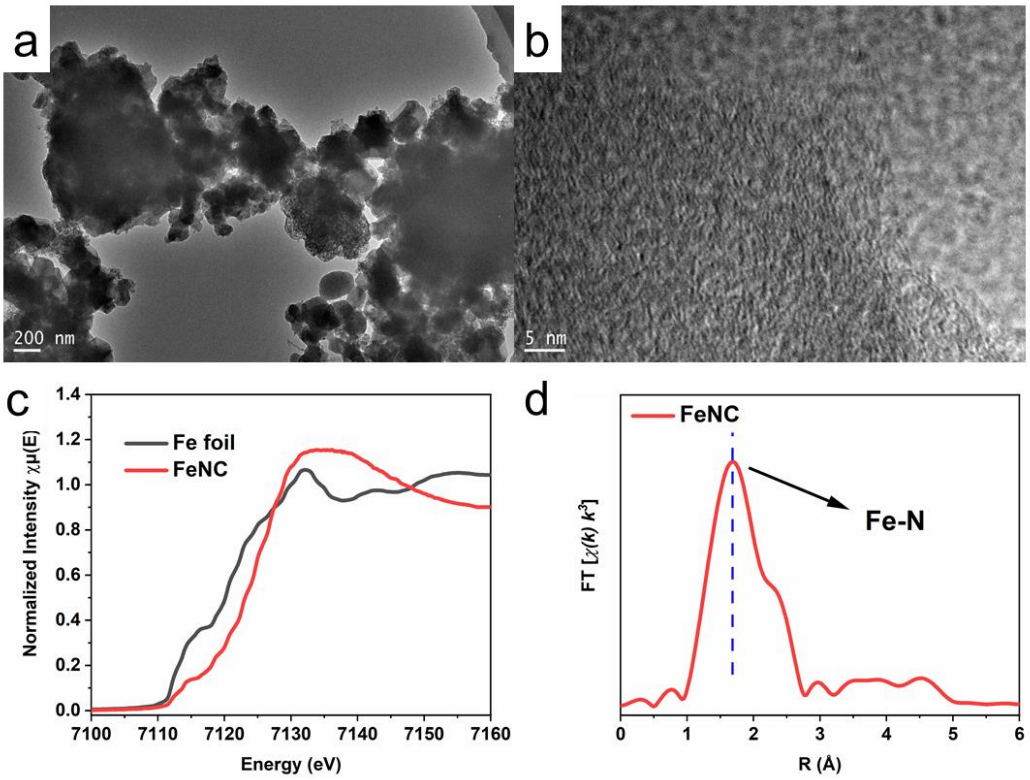

Figure 5.2 (a) and (b) TEM images of FeNC. (c) Fe K-edge XANES and (d) Fe K-edge EXAFS of FeNC.

5.1.2 Catalytic performance of the FeNC for ECO_2RR:

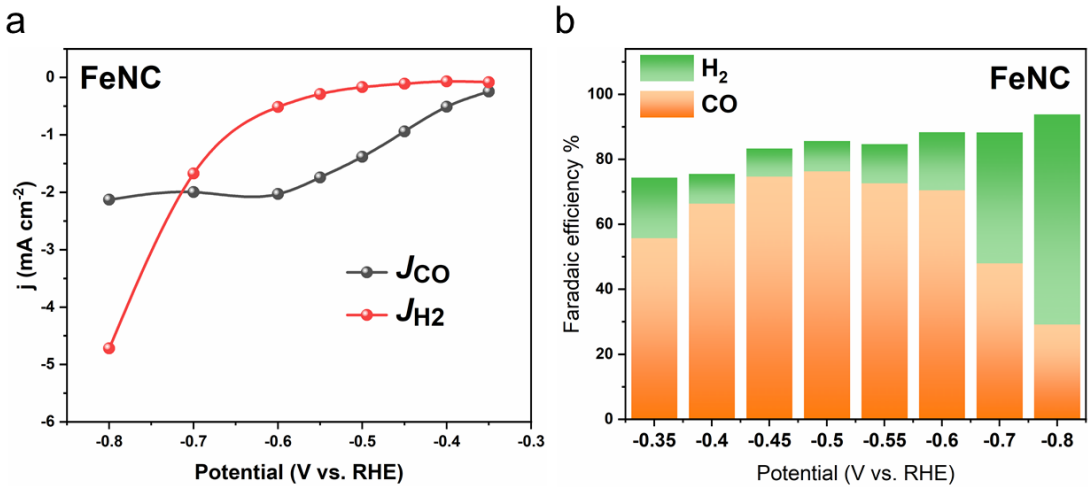

Figure 5.3 (a) CO and H_2 current densities of FeNC. (b) CO and H_2 FEs of FeNC

The FeNC catalyst electrode was applied in a customized H-cell to evaluate the catalytic performance of ECO_2RR (details in the experimental section). Several pre-run segments of CV

were performed to stabilize the catalyst electrodes before the test. FeNC exhibits catalytic activity toward CO and H_2 production **(Figure 5.3a)**, with a total syngas FE of around 83%. Besides, FeNC affords FEco up to around 76% at -0.45 V and -0.5 V vs. RHE **(Figure 5.3b)**, which is much higher than those of Co SACs and Co-Fe SACs presented in Chapters 3 and 4 above. It demonstrates that FeNC is a great catalyst for CO production in ECO_2RR. With rational modification, the CO productivity of FeNC can be further improved.

5.1.3 Al K-edge XAS characterization of ALD-Al_2O_3-FeNC:

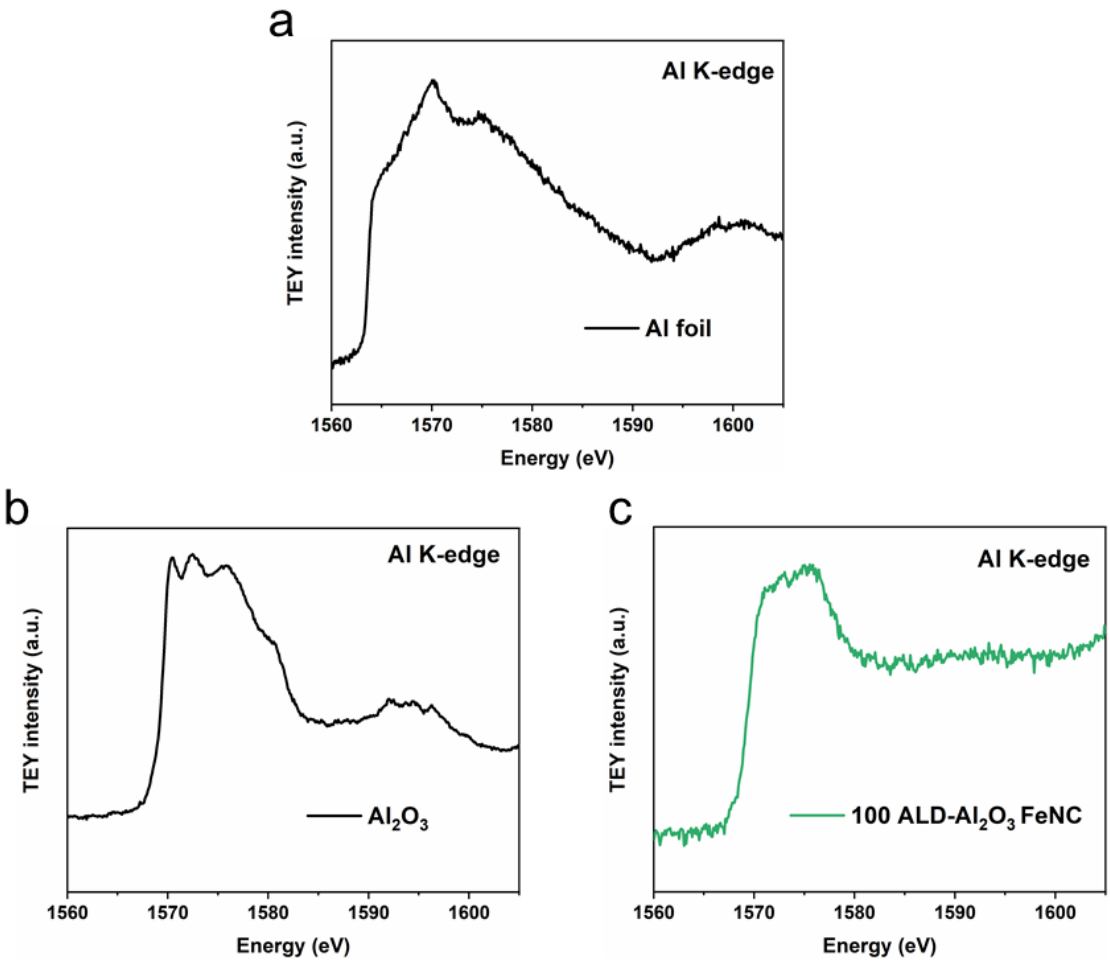

Figure 5.4 Al K-edge XAS of (a) Al foil, (b) Al_2O_3, and (c) 100 ALD-Al_2O_3 FeNC.

We then applied ALD-Al_2O_3 on FeNC to modify the catalyst, expecting the improvement of catalytic activity and stability in ECO_2RR. Because the cycle numbers of ALD-Al_2O_3 are small (10-100), the loading amount of ALD-Al_2O_3 is too low to be detected by conventional characterization measurements **(Figure 10.1)**. In this case, soft X-ray XAS was employed to analyze the Al

element in the ALD-Al_2O_3 FeNC catalysts. **Figure 5.4a** is the Al K-edge of standard Al reference. It appears that pure Al metal has a broad feature starting from before 1565 eV with a sharp peak at ca. 1570 eV. **Figure 5.4b** is the Al K-edge of the standard Al_2O_3 reference. Pure Al_2O_3 has a broad feature starting from 1570 eV with 3 peaks on a plateau from 1570-1580 eV. Comparing the two reference samples, it is obvious that Al^{3+} has a big energy shift toward higher energy than that of Al^0. 100 ALD-Al_2O_3 FeNC is the only sample that reveals distinguishable features among all the ALD-Al_2O_3 FeNC samples in Al K-edge XAS, as shown in **Figure 5.4c** with a broad feature starting from 1570 eV and a plateau from 1570-1580 eV. It shows that 100 ALD-Al_2O_3 FeNC exhibits a similar feature shape to that of the standard Al_2O_3 reference. It confirms the successful deposition of ALD-Al_2O_3 on FeNC.

5.1.4 Catalytic performance of the ALD-Al_2O_3-FeNC for ECO_2RR:

The ALD-Al_2O_3 FeNC catalyst electrodes were also tested for ECO_2RR. The deposition of ALD-Al_2O_3 on FeNC has a slight promotion in FEco. **Figure 5.5a** shows the FEco comparison between the ALD-Al_2O_3 FeNC catalysts and the original FeNC. 10 ALD-Al_2O_3 FeNC and 100 ALD-Al_2O_3 FeNC exhibit close FEco to that of the original FeNC while 25 ALD-Al_2O_3 FeNC affords some FEco promotions at the low potential range (-0.35 to -0.45 V vs. RHE). It demonstrates that an optimized small amount of ALD-Al_2O_3 can promote the CO product selectivity for FeNC on ECO_2RR. The underlying mechanism is waiting to be investigated with profound characterizations in the future to understand the contribution of ALD-Al_2O_3 on the FEco promotion of FeNC. After knowing the positive impact of ALD-Al_2O_3 on FEco for FeNC. We further carried out the catalytic stability test to see if ALD-Al_2O_3 coatings also have an impact on the ECO_2RR stability for FeNC.

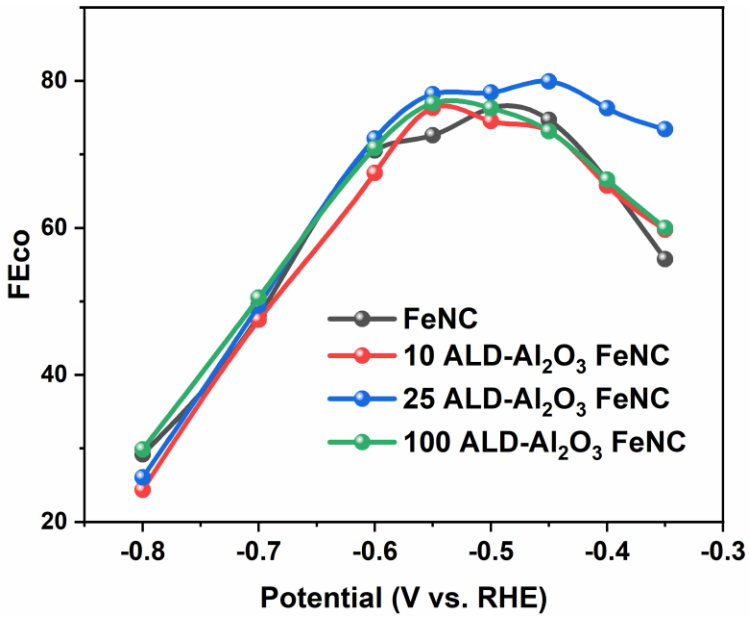

Figure 5.5 The evaluation of the electrocatalytic performance. CO Faradaic efficiency of the ALD-Al_2O_3 FeNC catalysts at various applied potentials.

The aging issue is a big problem for catalyst materials. In experience, fresh samples usually allow the best catalytic activity. After several months or even days, the aged samples show a decay in catalytic activity due to the valence variation of the active sites and the degradation of the catalyst structure.(Okatenko *et al.*, 2023; Zhang *et al.*, 2016) The ALD technique happens to be powerful in the fabrication of ultra-thin overcoating layers on the substate materials. Given these, we continued to explore the effect of ALD-Al_2O_3 against the aging problem for FeNC. As shown in **Figure 5.6a**, FeNC suffers from a dramatic FEco loss (around 18 % loss in the range from -0.4 V to -0.6 V vs. RHE, the highest FEco potential region for FeNC) after the aging of 10 months. Notably, 25 ALD-Al_2O_3 FeNC retains FEco in the range from -0.4 V to -0.6 V vs. RHE **(Figure 5.6b)**. With the FEco promotion provided by 25 ALD-Al_2O_3 **(Figure 5.5)**, after the aging of 10 months, 25 ALD-Al_2O_3 FeNC affords a 22 % FEco boost compared to the FeNC. It proves that except for the enhancement for FEco, ALD-Al_2O_3 can also significantly prevent the catalytic decay from aging of FeNC for ECO_2RR.

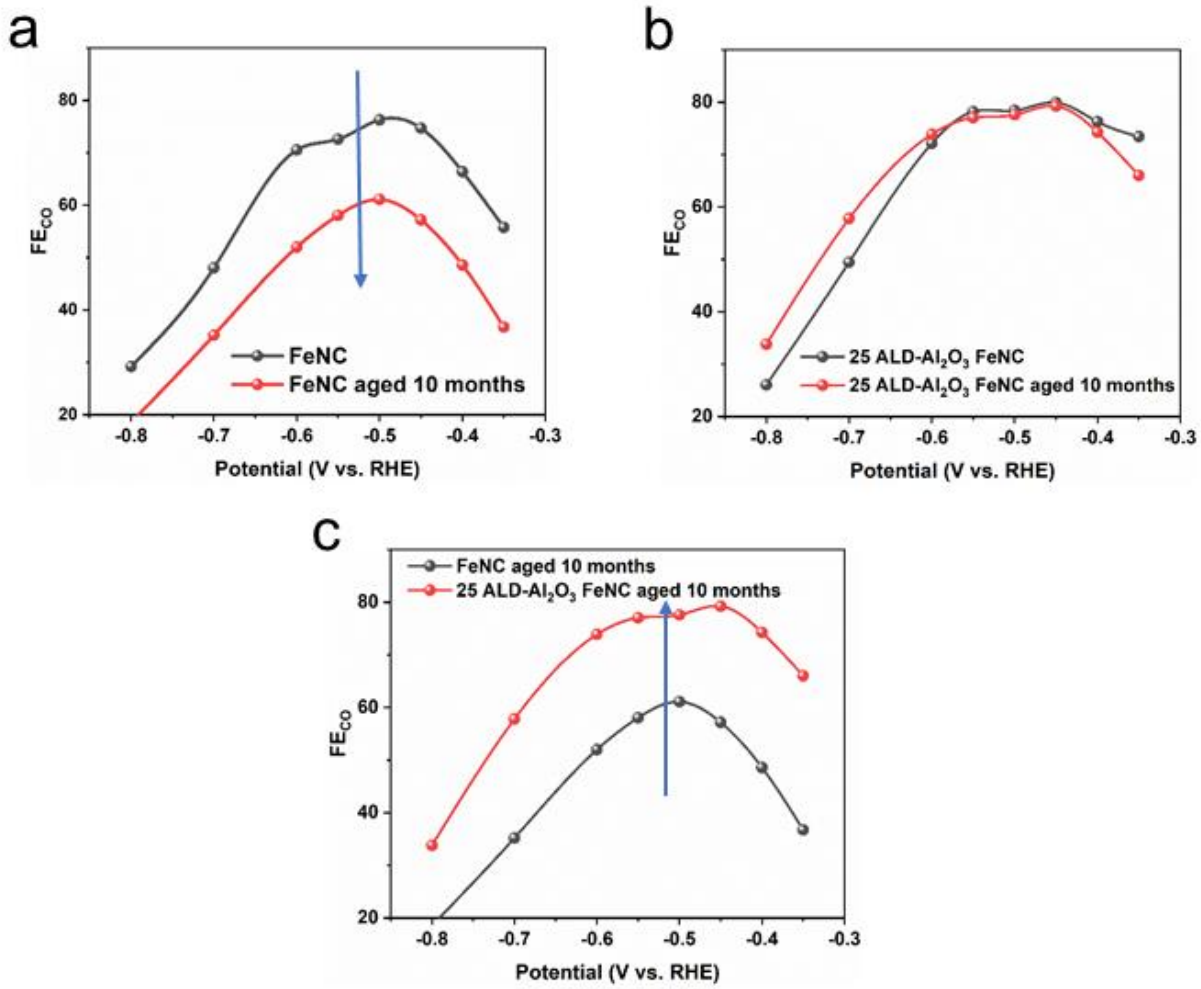

Figure 5.6 The FE of the original FeNC and the aged FeNC, the original ALD-Al_2O_3 FeNC, and aged ALD-Al_2O_3 FeNC at different potentials. FEco of (a) the original FeNC and aged FeNC (b) the 25 ALD-Al_2O_3 and the aged 25 ALD-Al_2O_3 FeNC. (c) FEco comparison of the aged FeNC and aged ALD-Al_2O_3 FeNC.

5.2 Conclusion and perspectives

FeNC was prepared as Fe SAC to perform ECO_2RR and reached a high FEco of around 76% at -0.45 V and -0.5 V vs. RHE. ALD technique was employed to add ALD-Al_2O_3 on FeNC. The 25 cycles of ALD-Al_2O_3 can slightly improve the FEco of FeNC up to around 80 %. Besides, 25 ALD-Al_2O_3 FeNC retains perfectly the ECO_2RR catalytic activity after the aging of 10 months. It means that ALD-Al_2O_3 holds great potential as the protection layer for catalyst aging issue in industrial applications.

Advanced characteristic measurements such as *in-situ* and *ex-situ* characterizations need to be conducted to understand the underlying mechanism of ALD-Al_2O_3's promoting CO production and preventing the aging issue in ECO_2RR of FeNC in the future.

Moreover, combined with the discoveries from the previous two research works, to better employ the ALD layer strategy, we can apply ECO_2RR active materials as ALD layers on FeNC to further improve the ECO_2RR performance. 1. To improve FEco, Co and Ni are promising transition metal candidates to conduct the experiments for CO production enhancement, whose ALD precursors have already reported. For ALD-NiO, bis(cyclopentadienyl)nickel(II) ($Ni(cp)_2$) is the Ni precursor and O_2 is the oxidation precursor. For ALD-CoO, bis(cyclopentadienyl)cobalt(II) ($Co(cp)_2$) is the Co precursor and O_2 is the oxidation precursor. The structure and thickness of ALD-prepared materials will be controlled by the precursor gas exposure time and the number of ALD cycles. 2. To further enhance the ECO_2RR performance, multi-metallic ALD-coating (e.g. bimetallic layer deposition such as Co-Ni ALD-coating) can also be fabricated to extend the catalytic potential of ALD in ECO_2RR. 3. For other possible ALD protection layers, TiO_2 is also a candidate as an over-coating material on catalyst materials for the stability issue, which exhibits CO_2RR catalytic activity in PCO_2RR. For ALD-TiO_2, titanium(IV) isopropoxide is the Ti precursor and H_2O is the oxidation precursor. With all these promising ALD materials, the ALD technique offers tremendous possibilities on improving the ECO_2RR performance of SACs.

6 CONCLUSION

To achieve highly efficient ECO_2RR performance, the rational design of fine catalysts requires to be profoundly explored. In this thesis, we focus on the modification methods (porosity adjustment, active site modification, bimetallic strategy, ALD technique) on state-of-art SACs for improved ECO_2RR performance, along with the logical analyses to investigate the relation between rational catalyst design and catalytic performance.

6.1 Simple grinding approach to modify the pore structure and active sites of SAC.

In Chapter 3, the profound investigation into the effect of ball-milling on ECO_2RR is introduced.

1. ZIF-8 derived Co SACs are synthesized with different grinding processes. The moderate grinding process of HM 15 mins affords the best ECO_2RR performance among all the other samples.
2. XAS and XES results confirm that the grinding process can cause slight variations in the electronic structure of the Co active sites, which can contribute to the promoted CO production in ECO_2RR.
3. The grinding method can modify the pore structure of Co SAC. A moderate grinding process promotes micro-pore and macro-pore structures of the catalyst material that benefits the active site hosting and mass transfer in ECO_2RR, respectively. The intense grinding process results in seriously damaged pore structures in the catalyst material, decreasing the exposed surface area and the prohibited mass transfer of ECO_2RR. Besides, the catalyst with the moderate grinding process also affords better stability than that of the original one.

This work illustrates that the simple grinding procedure can affect the ZIF-8-derived SACs in both electronic structures and physical pore structures, promoting ECO_2RR. It might also apply to other catalytic reactions and should be considered during the synthesis and evaluation of this kind of catalyst material.

6.2 Bimetallic strategy to modify active sites in SAC.

In Chapter 4, Fe is introduced in Co SAC to form bimetallic Fe-Co SAC for ECO_2RR.

1. Fe-Co bimetallic SACs are fabricated by introducing Fe into Co-SAC. The Fe-Co bimetallic SACs exhibit high activity towards syngas production in ECO_2RR, with an extremely stable FE_{CO+H2} as high as 93 % for more than 10 hours.
2. Metal K-edge XAS confirms that the addition of Fe would interfere with the local coordination environment of Co in bimetallic catalysts. The proper amount of Fe in C-Fe-Co-ZIF-1.6 wt%-Fe increases the number of M-N sites and creates mild distortions in the local coordination environment of the metal sites, showing the best CO production performance in ECO_2RR among all the C-Fe-Co-ZIF samples.
3. Using the same bimetallic strategy, Cu-Co bimetallic SACs also exhibit positive results on CO production for the syngas generation, while Ni-Co bimetallic SACs facilitate other product generations than syngas.

This work demonstrates the synergistic effects concerning the metal combination and the interactions between different metal atoms should be considered for the design of atomically dispersed TM bimetallic catalysts in ECO_2RR.

6.3 FeNC as Fe SAC and ALD modification for ECO_2RR.

In Chapter 5, Fe SAC FeNC is tested in ECO_2RR, along with the ALD-Al_2O_3 modification.

1. FeNC was prepared as Fe SAC to perform ECO_2RR and reached a high FEco of around 76 % at -0.45 V and -0.5 V vs. RHE. ALD technique was employed to add ALD-Al_2O_3 on FeNC. The 25 cycles of ALD-Al_2O_3 can slightly improve the FEco of FeNC up to 80 %.
2. 25 cycles of ALD-Al_2O_3 prevent FeNC from aging. 25 ALD-Al_2O_3 FeNC retains perfectly the ECO_2RR catalytic activity after the aging of 10 months.
3. Future work can concentrate on the ALD-coating fabrication of ECO_2RR active materials such as CoO and NiO whose ALD precursors are accessible. Moreover, ALD bimetallic materials can also be considered for more opportunities to promote ECO_2RR by ALD.

This work reveals the great potential of ALD-Al_2O_3 in catalytic performance promotion and catalyst protection. The later has big potential in future industry applications. Profound characterizations need to be analyzed to understand the promotion and protection that ALD-Al_2O_3 offers to FeNC in ECO_2RR in the future. And other promising ALD materials can be employed to promote the ECO_2RR of SACs.

7 BIBLIOGRAPHIE

Agarwal AS, Zhai Y, Hill D, Sridhar N (2011) The electrochemical reduction of carbon dioxide to formate/formic acid: engineering and economic feasibility. *ChemSusChem* 4(9):1301-1310.

Andrade JD (1985) X-ray Photoelectron Spectroscopy (XPS). 10.1007/978-1-4684-8610-0_5:105-195.

Andrei V, Reuillard B, Reisner E (2019) Bias-free solar syngas production by integrating a molecular cobalt catalyst with perovskite-BiVO4 tandems. *Nat Mater* 10.1038/s41563-019-0501-6.

Anonyme (2021) From Paris to Glasgow. *Nature Catalysis* 4(11):913-914.

Bae D, Seger B, Vesborg PC, Hansen O, Chorkendorff I (2017) Strategies for stable water splitting via protected photoelectrodes. *Chemical Society Reviews* 46(7):1933-1954.

Benson EE, Kubiak CP, Sathrum AJ, Smieja JM (2009) Electrocatalytic and homogeneous approaches to conversion of CO_2 to liquid fuels. *Chemical Society Reviews* 38(1):89-99.

Bhosale RR, Kumar A, AlMomani F, Alxneit I (2016) Sol–gel derived CeO 2 –Fe 2 O 3 nanoparticles: Synthesis, characterization and solar thermochemical application. *Ceramics International* 42(6):6728-6737.

Bunaciu AA, Udristioiu EG, Aboul-Enein HY (2015) X-ray diffraction: instrumentation and applications. *Critical Reviews in Analytical Chemistry* 45(4):289-299.

Burstein GT (2005) A hundred years of Tafel's Equation: 1905–2005. *Corrosion Science* 47(12):2858-2870.

Chang XX, Zhao YR, Xu BJ (2020) pH Dependence of Cu Surface Speciation in the Electrochemical CO Reduction Reaction. *ACS Catalysis* 10(23):13737-13747.

Chao C-C, Motoyama M, Prinz FB (2012) Nanostructured Platinum Catalysts by Atomic-Layer Deposition for Solid-Oxide Fuel Cells. *Advanced Energy Materials* 2(6):651-654.

Chen A, Lin B-L (2018) A Simple Framework for Quantifying Electrochemical CO 2 Fixation. *Joule* 2(4):594-606.

Chen D, Wang Y, Liu D, Liu H, Qian C, He H, Yang J (2020a) Surface composition dominates the electrocatalytic reduction of CO_2 on ultrafine CuPd nanoalloys. *Carbon Energy* 2(3):443-451.

Chen W-T, Hsu C-W, Lee J-F, Pao C-W, Hsu IJ (2020b) Theoretical Analysis of Fe K-Edge XANES on Iron Pentacarbonyl. *ACS Omega* 5(10):4991-5000.

Chen Z, Zhang G, Du L, Zheng Y, Sun L, Sun S (2020c) Nanostructured Cobalt-Based Electrocatalysts for CO_2 Reduction: Recent Progress, Challenges, and Perspectives. *Small* 16(52):e2004158.

Chen Z, Zhang G, Wen Y, Chen N, Chen W, Regier T, Dynes J, Zheng Y, Sun S (2021a) Atomically Dispersed Fe-Co Bimetallic Catalysts for the Promoted Electroreduction of Carbon Dioxide. *Nanomicro Lett* 14(1):25.

Chen Z, Zhang X, Liu W, Jiao M, Mou K, Zhang X, Liu L (2021b) Amination strategy to boost CO_2 electroreduction current density of M-N/C single-atom catalysts to industrial application level. *Energy & Environmental Science* 10.1039/d0ee04052e.

Chen ZS, Zhang GX, Chen HR, Prakash J, Zheng Y, Sun SH (2022) Multi-metallic catalysts for the electroreduction of carbon dioxide: Recent advances and perspectives. *Renewable & Sustainable Energy Reviews* 155:111922.

Chen ZS, Zhang GX, Prakash J, Zheng Y, Sun SH (2019) Rational Design of Novel Catalysts with Atomic Layer Deposition for the Reduction of Carbon Dioxide. *Advanced Energy Materials* 9(37):1900889.

Cheng H, Liu S, Zhang J, Zhou T, Zhang N, Zheng XS, Chu W, Hu Z, Wu C, Xie Y (2020) Surface Nitrogen-Injection Engineering for High Formation Rate of CO_2 Reduction to Formate. *Nano Letters* 20(8):6097-6103.

Cheng M-J, Kwon Y, Head-Gordon M, Bell AT (2015) Tailoring Metal-Porphyrin-Like Active Sites on Graphene to Improve the Efficiency and Selectivity of Electrochemical CO_2 Reduction. *The Journal of Physical Chemistry C* 119(37):21345-21352.

Cheng N, Stambula S, Wang D, Banis MN, Liu J, Riese A, Xiao B, Li R, Sham TK, Liu LM, Botton GA, Sun X (2016) Platinum single-atom and cluster catalysis of the hydrogen evolution reaction. *Nat Commun* 7:13638.

Chenitz R, Kramm UI, Lefèvre M, Glibin V, Zhang G, Sun S, Dodelet J-P (2018) A specific demetalation of Fe–N4 catalytic sites in the micropores of NC_Ar + NH3 is at the origin of the initial activity loss of the highly active Fe/N/C catalyst used for the reduction of oxygen in PEM fuel cells. *Energy & Environmental Science* 11(2):365-382.

Cho JH, Lee C, Hong SH, Jang HY, Back S, Seo MG, Lee M, Min HK, Choi Y, Jang YJ, Ahn SH, Jang HW, Kim SY (2022) Transition Metal Ion Doping on ZIF-8 Enhances the Electrochemical CO_2 Reduction Reaction. *Advanced Materials* 10.1002/adma.202208224:e2208224.

Chrisey DB, Pique A, McGill RA, Horwitz JS, Ringeisen BR, Bubb DM, Wu PK (2003) Laser deposition of polymer and biomaterial films. *Chemical Reviews* 103(2):553-576.

CHUANG TJ, BRIDLE CR, RICE DW (1976) INTERPRETATION OF THE X-RAY PHOTOEMISSION SPECTRA OF COBALT OXIDES AND COBALT OXIDE SURFACES. *Surface Science* 59:413-429.

Cychosz KA, Thommes M (2018) Progress in the Physisorption Characterization of Nanoporous Gas Storage Materials. *Engineering* 4(4):559-566.

Dai L, Qin Q, Wang P, Zhao X, Hu C, Liu P, Qin R, Chen M, Ou D, Xu C, Mo S, Wu B, Fu G, Zhang P, Zheng N (2017) Ultrastable atomic copper nanosheets for selective electrochemical reduction of carbon dioxide. *Sci Adv* 3(9):e1701069.

De Gregorio GL, Burdyny T, Loiudice A, Iyengar P, Smith WA, Buonsanti R (2020) Facet-Dependent Selectivity of Cu Catalysts in Electrochemical CO_2 Reduction at Commercially Viable Current Densities. *ACS Catal* 10(9):4854-4862.

de Groot F (2001) High-resolution X-ray emission and X-ray absorption spectroscopy. *Chemical Reviews* 101(6):1779-1808.

Detavernier C, Dendooven J, Sree SP, Ludwig KF, Martens JA (2011) Tailoring nanoporous materials by atomic layer deposition. *Chemical Society Reviews* 40(11):5242-5253.

Dinh C-T, Burdyny T, Kibria MG, Seifitokaldani A, Gabardo CM, García de Arquer FP, Kiani A, Edwards JP, De Luna P, Bushuyev OS, Zou C, Quintero-Bermudez R, Pang Y, Sinton D, Sargent EH (2018) CO_2 electroreduction to ethylene via hydroxide-mediated copper catalysis at an abrupt interface. *Science* 360(6390):783-787.

Dong H, Zhang L, Li L, Deng W, Hu C, Zhao ZJ, Gong J (2019) Abundant Ce^{3+} Ions in Au-CeO_x Nanosheets to Enhance CO_2 Electroreduction Performance. *Small* 15(17):e1900289.

Douglas A, Carter R, Li M, Pint CL (2018) Toward Small-Diameter Carbon Nanotubes Synthesized from Captured Carbon Dioxide: Critical Role of Catalyst Coarsening. *ACS Appl Mater Interfaces* 10(22):19010-19018.

Douglas A, Carter R, Muralidharan N, Oakes L, Pint CL (2017) Iron catalyzed growth of crystalline multi-walled carbon nanotubes from ambient carbon dioxide mediated by molten carbonates. *Carbon* 116:572-578.

Fan L, Xia C, Zhu P, Lu Y, Wang H (2020) Electrochemical CO_2 reduction to high-concentration pure formic acid solutions in an all-solid-state reactor. *Nat Commun* 11(1):3633.

Fang B, Bonakdarpour A, Reilly K, Xing Y, Taghipour F, Wilkinson DP (2014) Large-Scale Synthesis of TiO_2 Microspheres with Hierarchical Nanostructure for Highly Efficient Photodriven Reduction of CO_2 to CH_4. *ACS Applied Materials & Interfaces* 6(17):15488-15498.

Fujita E (1999) Photochemical carbon dioxide reduction with metal complexes. *Coordination Chemistry Reviews* 185-186:373-384.

Gao S, Jiao X, Sun Z, Zhang W, Sun Y, Wang C, Hu Q, Zu X, Yang F, Yang S, Liang L, Wu J, Xie Y (2016a) Ultrathin Co3O4 Layers Realizing Optimized CO_2 Electroreduction to Formate. *Angewandte Chemie, International Edition in English* 55(2):698-702.

Gao S, Lin Y, Jiao X, Sun Y, Luo Q, Zhang W, Li D, Yang J, Xie Y (2016b) Partially oxidized atomic cobalt layers for carbon dioxide electroreduction to liquid fuel. *Nature* 529(7584):68-71.

Gao Y, Wu Q, Liang X, Wang Z, Zheng Z, Wang P, Liu Y, Dai Y, Whangbo MH, Huang B (2020) Cu2O Nanoparticles with Both {100} and {111} Facets for Enhancing the Selectivity and Activity of CO_2 Electroreduction to Ethylene. *Adv Sci (Weinh)* 7(6):1902820.

Garcia de Arquer FP, Dinh CT, Ozden A, Wicks J, McCallum C, Kirmani AR, Nam DH, Gabardo C, Seifitokaldani A, Wang X, Li YC, Li F, Edwards J, Richter LJ, Thorpe SJ, Sinton D, Sargent EH (2020) CO_2 electrolysis to multicarbon products at activities greater than 1 A cm^{-2}. *Science* 367(6478):661-666.

Geng Z, Kong X, Chen W, Su H, Liu Y, Cai F, Wang G, Zeng J (2018) Oxygen Vacancies in ZnO Nanosheets Enhance CO_2 Electrochemical Reduction to CO. *Angewandte Chemie, International Edition in English* 57(21):6054-6059.

George SM (2010) Atomic layer deposition: an overview. *Chemical Reviews* 110(1):111-131.

George SM, Ott AW, Klaus JW (1996) Surface Chemistry for Atomic Layer Growth. *The Journal of Physical Chemistry* 100(31):13121-13131.

Gu J, Hsu CS, Bai L, Chen HM, Hu X (2019) Atomically dispersed Fe^{3+} sites catalyze efficient CO_2 electroreduction to CO. *Science* 364(6445):1091-1094.

Guo S, Zhao S, Wu X, Li H, Zhou Y, Zhu C, Yang N, Jiang X, Gao J, Bai L, Liu Y, Lifshitz Y, Lee ST, Kang Z (2017) A Co_3O_4-CDots-C_3N_4 three component electrocatalyst design concept for efficient and tunable CO_2 reduction to syngas. *Nat Commun* 8(1):1828.

Guo Y, Yao S, Xue Y, Hu X, Cui H, Zhou Z (2022) Nickel single-atom catalysts intrinsically promoted by fast pyrolysis for selective electroreduction of CO_2 into CO. *Applied Catalysis B: Environmental* 304:120997.

Han N, Ding P, He L, Li Y, Li Y (2019) Promises of Main Group Metal–Based Nanostructured Materials for Electrochemical CO_2 Reduction to Formate. *Advanced Energy Materials* 10(11):1902338.

Han P, Wang ZJ, Kuang M, Wang YF, Liu JN, Hu LF, Qian LP, Zheng GF (2018) 2D Assembly of Confined Space toward Enhanced CO_2 Electroreduction. *Advanced Energy Materials* 8(25):1801230.

Han ZK, Sarker D, Ouyang R, Mazheika A, Gao Y, Levchenko SV (2021) Single-atom alloy catalysts designed by first-principles calculations and artificial intelligence. *Nat Commun* 12(1):1833.

Hausmann D, Becker J, Wang S, Gordon RG (2002) Rapid vapor deposition of highly conformal silica nanolaminates. *Science* 298(5592):402-406.

He Q, Liu D, Lee JH, Liu Y, Xie Z, Hwang S, Kattel S, Song L, Chen JG (2019) Electrochemical Conversion of CO_2 to Syngas with Controllable CO/H_2 Ratios over Co and Ni Single-Atom Catalysts. *Angewandte Chemie, International Edition in English* 10.1002/anie.201912719.

He Y, Zhang L, Teng B, Fan M (2015) New application of Z-scheme Ag_3PO_4/g-C_3N_4 composite in converting CO_2 to fuel. *Environmental Science and Technology* 49(1):649-656.

Hibberd AM, Doan HQ, Glass EN, de Groot FMF, Hill CL, Cuk T (2015) Co Polyoxometalates and a Co_3O_4 Thin Film Investigated by L-Edge X-ray Absorption Spectroscopy. *The Journal of Physical Chemistry C* 119(8):4173-4179.

Hod I, Sampson MD, Deria P, Kubiak CP, Farha OK, Hupp JT (2015) Fe-Porphyrin-Based Metal–Organic Framework Films as High-Surface Concentration, Heterogeneous Catalysts for Electrochemical Reduction of CO_2. *ACS Catalysis* 5(11):6302-6309.

Holder CF, Schaak RE (2019) Tutorial on Powder X-ray Diffraction for Characterizing Nanoscale Materials. *ACS Nano* 13(7):7359-7365.

Hu C, Bai S, Gao L, Liang S, Yang J, Cheng S-D, Mi S-B, Qiu J (2019) Porosity-Induced High Selectivity for CO_2 Electroreduction to CO on Fe-Doped ZIF-Derived Carbon Catalysts. *ACS Catalysis* 9(12):11579-11588.

Hu S, Shaner MR, Beardslee JA, Lichterman M, Brunschwig BS, Lewis NS (2014) Amorphous TiO_2 coatings stabilize Si, GaAs, and GaP photoanodes for efficient water oxidation. *Science* 344(6187):1005-1009.

Hulva J, Meier M, Bliem R, Jakub Z, Kraushofer F, Schmid M, Diebold U, Franchini C, Parkinson GS (2021) Unraveling CO adsorption on model single-atom catalysts. *Science* 371(6527):375-379.

Hwang YJ, Hahn C, Liu B, Yang P (2012) Photoelectrochemical properties of TiO_2 nanowire arrays: a study of the dependence on length and atomic layer deposition coating. *ACS Nano* 6(6):5060-5069.

Inoue T, Fujishima A, Konishi S, Honda K (1979) Photoelectrocatalytic reduction of carbon dioxide in aqueous suspensions of semiconductor powders. *Nature* 277(5698):637-638.

Jeong H, Kwon O, Kim BS, Bae J, Shin S, Kim HE, Kim J, Lee HJ (2020) Highly durable metal ensemble catalysts with full dispersion for automotive applications beyond single-atom catalysts. *Nature Catalysis* 3(4):368-375.

Jhong H-RM, Brushett FR, Kenis PJA (2013) The Effects of Catalyst Layer Deposition Methodology on Electrode Performance. *Advanced Energy Materials* 3(5):589-599.

Ji S, Qu Y, Wang T, Chen Y, Wang G, Li X, Dong J, Chen Q, Zhang W, Zhang Z, Liang S, Yu R, Wang Y, Wang D, Li Y (2020) Rare-Earth Single Erbium Atoms for Enhanced Photocatalytic CO_2 Reduction. *Angewandte Chemie, International Edition in English* 59(26):10651-10657.

Jiang Z, Wang T, Pei J, Shang H, Zhou D, Li H, Dong J, Wang Y, Cao R, Zhuang Z, Chen W, Wang D, Zhang J, Li Y (2020) Discovery of main group single Sb–N4 active sites for CO_2 electroreduction to formate with high efficiency. *Energy & Environmental Science* 10.1039/d0ee01486a.

Jiao L, Zhu J, Zhang Y, Yang W, Zhou S, Li A, Xie C, Zheng X, Zhou W, Yu SH, Jiang HL (2021) Non-Bonding Interaction of Neighboring Fe and Ni Single-Atom Pairs on MOF-Derived N-Doped Carbon for Enhanced CO_2 Electroreduction. *Journal of the American Chemical Society* 143(46):19417-19424.

Jin L, Liu B, Wang P, Yao H, Achola LA, Kerns P, Lopes A, Yang Y, Ho J, Moewes A, Pei Y, He J (2018) Ultrasmall Au nanocatalysts supported on nitrided carbon for electrocatalytic CO_2 reduction: the role of the carbon support in high selectivity. *Nanoscale* 10(30):14678-14686.

Jing H, Zhu P, Zheng X, Zhang Z, Wang D, Li Y (2022) Theory-oriented screening and discovery of advanced energy transformation materials in electrocatalysis. *Advanced Powder Materials* 1(1):100013.

Johnson RW, Hultqvist A, Bent SF (2014) A brief review of atomic layer deposition: from fundamentals to applications. *Materials Today* 17(5):236-246.

Jung YS, Lu P, Cavanagh AS, Ban C, Kim G-H, Lee S-H, George SM, Harris SJ, Dillon AC (2013) Unexpected Improved Performance of ALD Coated $LiCoO_2$/Graphite Li-Ion Batteries. *Advanced Energy Materials* 3(2):213-219.

Kang J, He S, Zhou W, Shen Z, Li Y, Chen M, Zhang Q, Wang Y (2020) Single-pass transformation of syngas into ethanol with high selectivity by triple tandem catalysis. *Nat Commun* 11(1):827.

Kibria MG, Edwards JP, Gabardo CM, Dinh CT, Seifitokaldani A, Sinton D, Sargent EH (2019) Electrochemical CO_2 Reduction into Chemical Feedstocks: From Mechanistic Electrocatalysis Models to System Design. *Advanced Materials* 10.1002/adma.201807166:e1807166.

Kim W, Edri E, Frei H (2016) Hierarchical Inorganic Assemblies for Artificial Photosynthesis. *Accounts of Chemical Research* 49(9):1634-1645.

Knapp CE, Carmalt CJ (2016) Solution based CVD of main group materials. *Chemical Society Reviews* 45(4):1036-1064.

Konno H (2016) X-ray Photoelectron Spectroscopy. 10.1016/b978-0-12-805256-3.00008-8:153-171.

Kornienko N, Zhao Y, Kley CS, Zhu C, Kim D, Lin S, Chang CJ, Yaghi OM, Yang P (2015) Metal-organic frameworks for electrocatalytic reduction of carbon dioxide. *Journal of the American Chemical Society* 137(44):14129-14135.

Kot M, Kegelmann L, Das C, Kus P, Tsud N, Matolinova I, Albrecht S, Matolin V, Schmeisser D (2018) Room-Temperature Atomic-Layer-Deposited Al2 O3 Improves the Efficiency of Perovskite Solar Cells over Time. *ChemSusChem* 10.1002/cssc.201801434.

Kou ZK, Li X, Wang TT, Ma YY, Zang WJ, Nie GD, Wang J (2021) Fundamentals, On-Going Advances and Challenges of Electrochemical Carbon Dioxide Reduction. *Electrochemical Energy Reviews* 10.1007/s41918-021-00096-5.

Kutz RB, Chen Q, Yang H, Sajjad SD, Liu Z, Masel IR (2017) Sustainion Imidazolium-Functionalized Polymers for Carbon Dioxide Electrolysis. *Energy Technology* 5(6):929-936.

Leow WR, Lum Y, Ozden A, Wang Y, Nam DH, Chen B, Wicks J, Zhuang TT, Li F, Sinton D, Sargent EH (2020) Chloride-mediated selective electrosynthesis of ethylene and propylene oxides at high current density. *Science* 368(6496):1228-1233.

Leskelä M, Ritala M (2002) Atomic layer deposition (ALD): from precursors to thin film structures. *Thin Solid Films* 409(1):138-146.

Lewis NS (2016) Aspects of science and technology in support of legal and policy frameworks associated with a global carbon emissions-control regime. *Energy & Environmental Science* 9(7):2172-2176.

Li C, Wang T, Liu B, Chen M, Li A, Zhang G, Du M, Wang H, Liu SF, Gong J (2019) Photoelectrochemical CO_2 reduction to adjustable syngas on grain-boundary-mediated a-Si/TiO_2/Au photocathodes with low onset potentials. *Energy & Environmental Science* 12(3):923-928.

Li TC, Góes MS, Fabregat-Santiago F, Bisquert J, Bueno PR, Prasittichai C, Hupp JT, Marks TJ (2009) Surface Passivation of Nanoporous TiO_2 via Atomic Layer Deposition of ZrO_2 for Solid-State Dye-Sensitized Solar Cell Applications. *The Journal of Physical Chemistry C* 113(42):18385-18390.

Li Z, He D, Yan X, Dai S, Younan S, Ke Z, Pan X, Xiao X, Wu H, Gu J (2020) Size-Dependent Nickel-Based Electrocatalysts for Selective CO_2 Reduction. *Angewandte Chemie, International Edition in English* 59(42):18572-18577.

Li Z, Wu R, Xiao S, Yang Y, Lai L, Chen JS, Chen Y (2022) Axial chlorine coordinated iron-nitrogen-carbon single-atom catalysts for efficient electrochemical CO_2 reduction. *Chemical Engineering Journal* 430:132882.

Lim BS, Rahtu A, Gordon RG (2003) Atomic layer deposition of transition metals. *Nat Mater* 2(11):749-754.

Lin L, Li H, Wang Y, Li H, Wei P, Nan B, Si R, Wang G, Bao X (2021) Temperature-Dependent CO_2 Electroreduction over Fe-N-C and Ni-N-C Single-Atom Catalysts. *Angewandte Chemie, International Edition in English* 60(51):26582-26586.

Lin L, Li H, Yan C, Li H, Si R, Li M, Xiao J, Wang G, Bao X (2019) Synergistic Catalysis over Iron-Nitrogen Sites Anchored with Cobalt Phthalocyanine for Efficient CO_2 Electroreduction. *Advanced Materials* 31(41):e1903470.

Liu H, Meng X, Dao TD, Zhang H, Li P, Chang K, Wang T, Li M, Nagao T, Ye J (2015) Conversion of Carbon Dioxide by Methane Reforming under Visible-Light Irradiation: Surface-Plasmon-Mediated Nonpolar Molecule Activation. *Angewandte Chemie, International Edition in English* 54(39):11545-11549.

Liu J, Kong X, Zheng L, Guo X, Liu X, Shui J (2020a) Rare Earth Single-Atom Catalysts for Nitrogen and Carbon Dioxide Reduction. *ACS Nano* 14(1):1093-1101.

Liu J, Zhu D, Guo C, Vasileff A, Qiao SZ (2017) Design Strategies toward Advanced MOF-Derived Electrocatalysts for Energy-Conversion Reactions. *Advanced Energy Materials* 7(23):1700518.

Liu M, Pang Y, Zhang B, De Luna P, Voznyy O, Xu J, Zheng X, Dinh CT, Fan F, Cao C, de Arquer FPG, Safaei TS, Mepham A, Klinkova A, Kumacheva E, Filleter T, Sinton D, Kelley SO, Sargent EH (2016) Enhanced electrocatalytic CO_2 reduction via field-induced reagent concentration. *Nature* 537(7620):382-386.

Liu P, Chen B, Liang C, Yao W, Cui Y, Hu S, Zou P, Zhang H, Fan HJ, Yang C (2021) Tip-Enhanced Electric Field: A New Mechanism Promoting Mass Transfer in Oxygen Evolution Reactions. *Advanced Materials* 33(9):e2007377.

Liu Y, Tian D, Biswas AN, Xie Z, Hwang S, Lee JH, Meng H, Chen JG (2020b) Transition Metal Nitrides as Promising Catalyst Supports for Tuning CO/H2 Syngas Production from Electrochemical CO_2 Reduction. *Angewandte Chemie, International Edition in English* 59(28):11345-11348.

Long J, Zhang H, Ming J, Zhao J, Gu Q, Xu C, Ding Z, Yuan R, Zhang Z, Lin H, Wang X (2019) High-rate, tunable syngas production with artificial photosynthetic cells. *Angewandte Chemie, International Edition in English* 10.1002/anie.201902361.

Lou XD (2019) Bi2O3 Nanosheets Grown on Multi-Channel Carbon Matrix Catalyze Efficient CO_2 Electroreduction to HCOOH. *Angewandte Chemie, International Edition in English* 10.1002/anie.201907674.

Lu P, Yang Y, Yao J, Wang M, Dipazir S, Yuan M, Zhang J, Wang X, Xie Z, Zhang G (2019) Facile synthesis of single-nickel-atomic dispersed N-doped carbon framework for efficient electrochemical CO_2 reduction. *Applied Catalysis B: Environmental* 241:113-119.

Lu Y, Zhou P, Han J, Yu F (2015) Fischer–Tropsch synthesis of liquid hydrocarbons over mesoporous SBA-15 supported cobalt catalysts. *RSC Advances* 5(73):59792-59803.

Luo M, Zhao Z, Zhang Y, Sun Y, Xing Y, Lv F, Yang Y, Zhang X, Hwang S, Qin Y, Ma JY, Lin F, Su D, Lu G, Guo S (2019) PdMo bimetallene for oxygen reduction catalysis. *Nature* 574(7776):81-85.

Lv F, Huang B, Feng J, Zhang W, Wang K, Li N, Zhou J, Zhou P, Yang W, Du Y, Su D, Guo S (2021) A highly efficient atomically thin curved PdIr bimetallene electrocatalyst. *National Science Review* 10.1093/nsr/nwab019.

Ma W, Wan H, Zhang L, Zheng JY, Zhou Z (2021) Single-atom catalysts for electrochemical energy storage and conversion. *Journal of Energy Chemistry* 63:170-194.

Ma W, Xie S, Liu T, Fan Q, Ye J, Sun F, Jiang Z, Zhang Q, Cheng J, Wang Y (2020) Electrocatalytic reduction of CO_2 to ethylene and ethanol through hydrogen-assisted C–C coupling over fluorine-modified copper. *Nature Catalysis* 3(6):478-487.

Magesh G, Kim ES, Kang HJ, Banu M, Kim JY, Kim JH, Lee JS (2014) A versatile photoanode-driven photoelectrochemical system for conversion of CO_2 to fuels with high faradaic efficiencies at low bias potentials. *Journal of Materials Chemistry A* 2(7):2044.

McNutt M (2015) Climate warning, 50 years later. *Science* 350(6262):721.

Meng X, Ionescu M, Banis MN, Zhong Y, Liu H, Zhang Y, Sun S, Li R, Sun X (2010) Heterostructural coaxial nanotubes of CNT@Fe2O3 via atomic layer deposition: effects of surface functionalization and nitrogen-doping. *Journal of Nanoparticle Research* 13(3):1207-1218.

Meng X, Wang T, Liu L, Ouyang S, Li P, Hu H, Kako T, Iwai H, Tanaka A, Ye J (2014) Photothermal conversion of CO_2 into CH_4 with H_2 over Group VIII nanocatalysts: an alternative approach for solar fuel production. *Angewandte Chemie, International Edition in English* 53(43):11478-11482.

Meng X, Zhang Y, Sun S, Li R, Sun X (2011) Three growth modes and mechanisms for highly structure-tunable SnO_2 nanotube arrays of template-directed atomic layer deposition. *Journal of Materials Chemistry* 21(33):12321.

Meng Y, Zhang X, Hung WH, He J, Tsai YS, Kuang Y, Kenney MJ, Shyue JJ, Liu Y, Stone KH, Zheng X, Suib SL, Lin MC, Liang Y, Dai H (2019) Highly active oxygen evolution integrated with efficient CO_2 to CO electroreduction. *Proc Natl Acad Sci U S A* 116(48):23915-23922.

Mesilov VV, Galakhov VR, Gubkin AF, Sherstobitova EA, Zakharova GS, Uimin MA, Yermakov AY, Kvashnina KO, Smirnov DA (2017) X-ray Diffraction and X-ray Spectroscopy Studies of Cobalt-Doped Anatase TiO_2:Co Nanopowders. *The Journal of Physical Chemistry C* 121(43):24235-24244.

Mohammed A, Abdullah A (2018) Scanning electron microscopy (SEM): A review. *Proceedings of the 2018 International Conference on Hydraulics and Pneumatics—HERVEX, Băile Govora, Romania.* p 7-9.

Mohd Adli N, Shan W, Hwang S, Samarakoon W, Karakalos S, Li Y, Cullen DA, Su D, Feng Z, Wang G, Wu G (2021) Engineering Atomically Dispersed FeN4 Active Sites for CO_2 Electroreduction. *Angewandte Chemie, International Edition in English* 60(2):1022-1032.

Mu Y, Wang TT, Zhang J, Meng CG, Zhang YF, Kou ZK (2022) Single-Atom Catalysts: Advances and Challenges in Metal-Support Interactions for Enhanced Electrocatalysis. *Electrochemical Energy Reviews* 5(1):145-186.

Nardi KL, Yang N, Dickens CF, Strickler AL, Bent SF (2015) Creating Highly Active Atomic Layer Deposited NiO Electrocatalysts for the Oxygen Evolution Reaction. *Advanced Energy Materials* 5(17):1500412.

Ni WP, Gao Y, Lin Y, Ma C, Guo XG, Wang SY, Zhang SG (2021) Nonnitrogen Coordination Environment Steering Electrochemical CO_2-to-CO Conversion over Single-Atom Tin Catalysts in a Wide Potential Window. *ACS Catalysis* 11(9):5212-5221.

Niu K, Xu Y, Wang H, Ye R, Xin HL, Lin F, Tian C, Lum Y, Bustillo KC, Doeff MM, Koper MTM, Ager J, Xu R, Zheng H (2017) A spongy nickel-organic CO_2 reduction photocatalyst for nearly 100% selective CO production. *Sci Adv* 3(7):e1700921.

Niwa H, Takachi M, Okamoto J, Wu WB, Chu YY, Singh A, Huang DJ, Moritomo Y (2017) Strong localization of oxidized Co^{3+} state in cobalt-hexacyanoferrate. *Sci Rep* 7(1):16579.

Okatenko V, Loiudice A, Newton MA, Stoian DC, Blokhina A, Chen AN, Rossi K, Buonsanti R (2023) Alloying as a Strategy to Boost the Stability of Copper Nanocatalysts during the Electrochemical CO_2 Reduction Reaction. *Journal of the American Chemical Society* 10.1021/jacs.2c13437.

Ouyang M, Papanikolaou KG, Boubnov A, Hoffman AS, Giannakakis G, Bare SR, Stamatakis M, Flytzani-Stephanopoulos M, Sykes ECH (2021) Directing reaction pathways via in situ control of active site geometries in PdAu single-atom alloy catalysts. *Nature Communications* 12(1).

Pan F, Li B, Sarnello E, Fei Y, Gang Y, Xiang X, Du Z, Zhang P, Wang G, Nguyen HT, Li T, Hu YH, Zhou HC, Li Y (2020) Atomically Dispersed Iron-Nitrogen Sites on Hierarchically

Mesoporous Carbon Nanotube and Graphene Nanoribbon Networks for CO_2 Reduction. *ACS Nano* 14(5):5506-5516.

Pan L, Kim JH, Mayer MT, Son M-K, Ummadisingu A, Lee JS, Hagfeldt A, Luo J, Grätzel M (2018a) Boosting the performance of Cu_2O photocathodes for unassisted solar water splitting devices. *Nature Catalysis* 10.1038/s41929-018-0077-6.

Pan X, Jiao F, Miao D, Bao X (2021) Oxide-Zeolite-Based Composite Catalyst Concept That Enables Syngas Chemistry beyond Fischer-Tropsch Synthesis. *Chemical Reviews* 121(11):6588-6609.

Pan Y, Lin R, Chen Y, Liu S, Zhu W, Cao X, Chen W, Wu K, Cheong WC, Wang Y, Zheng L, Luo J, Lin Y, Liu Y, Liu C, Li J, Lu Q, Chen X, Wang D, Peng Q, Chen C, Li Y (2018b) Design of Single-Atom Co-N5 Catalytic Site: A Robust Electrocatalyst for CO_2 Reduction with Nearly 100% CO Selectivity and Remarkable Stability. *Journal of the American Chemical Society* 140(12):4218-4221.

Pan YX, You Y, Xin S, Li Y, Fu G, Cui Z, Men YL, Cao FF, Yu SH, Goodenough JB (2017) Photocatalytic CO_2 Reduction by Carbon-Coated Indium-Oxide Nanobelts. *Journal of the American Chemical Society* 139(11):4123-4129.

Panzone C, Philippe R, Chappaz A, Fongarland P, Bengaouer A (2020) Power-to-Liquid catalytic CO_2 valorization into fuels and chemicals: focus on the Fischer-Tropsch route. *Journal of CO_2 Utilization* 38:314-347.

Park H, Kim KY, Youn DH, Choi YH, Kim WY, Lee JS (2017) Auto-Reduction Behavior of Cobalt on Graphitic Carbon Nitride Coated Alumina Supports for Fischer-Tropsch Synthesis. *ChemCatChem* 9(21):4098-4104.

Peng F, Wang J, Ge G, He T, Cao L, He Y, Ma H, Sun S (2013) Photochemical reduction of CO_2 catalyzed by silicon nanocrystals produced by high energy ball milling. *Materials Letters* 92:65-67.

Prakash J, Kumar V, Erasmus LJB, Duvenhage MM, Sathiyan G, Bellucci S, Sun S, Swart HC (2018) Phosphor Polymer Nanocomposite: ZnO:Tb^{3+} Embedded Polystyrene Nanocomposite Thin Films for Solid-State Lighting Applications. *ACS Applied Nano Materials* 1(2):977-988.

Prakash J, Swart HC, Zhang G, Sun S (2019) Emerging applications of atomic layer deposition for the rational design of novel nanostructures for surface-enhanced Raman scattering. *Journal of Materials Chemistry C* 7(6):1447-1471.

Prakash J, Tripathi A, Gautam S, Chae KH, Song J, Rigato V, Tripathi J, Asokan K (2014) Phenomenological understanding of dewetting and embedding of noble metal nanoparticles in thin films induced by ion irradiation. *Materials Chemistry and Physics* 147(3):920-924.

Pu Z, Amiinu IS, Cheng R, Wang P, Zhang C, Mu S, Zhao W, Su F, Zhang G, Liao S, Sun S (2020) Single-Atom Catalysts for Electrochemical Hydrogen Evolution Reaction: Recent Advances and Future Perspectives. *Nano-Micro Letters* 12(1).

Puurunen RL (2005) Surface chemistry of atomic layer deposition: A case study for the trimethylaluminum/water process. *Journal of Applied Physics* 97(12):121301.

Puurunen RL, Lindblad M, Root A, Outi I. Krause A (2001) Successive reactions of gaseous trimethylaluminium and ammonia on porous alumina. *Physical Chemistry Chemical Physics* 3(6):1093-1102.

Puurunen RL, Root A, Haukka S, Iiskola EI, Lindblad M, Krause AOI (2000) IR and NMR Study of the Chemisorption of Ammonia on Trimethylaluminum-Modified Silica. *The Journal of Physical Chemistry B* 104(28):6599-6609.

Qiao H, Wang X, Dong Q, Zheng H, Chen G, Hong M, Yang C-P, Wu M, He K, Hu L (2021) A High-Entropy Phosphate Catalyst for Oxygen Evolution Reaction. *Nano Energy* 10.1016/j.nanoen.2021.106029:106029.

Qiao J, Liu Y, Hong F, Zhang J (2014) A review of catalysts for the electroreduction of carbon dioxide to produce low-carbon fuels. *Chemical Society Reviews* 43(2):631-675.

Ratso S, Sougrati MT, Käärik M, Merisalu M, Rähn M, Kisand V, Kikas A, Paiste P, Leis J, Sammelselg V, Jaouen F, Tammeveski K (2019) Effect of Ball-Milling on the Oxygen Reduction Reaction Activity of Iron and Nitrogen Co-doped Carbide-Derived Carbon Catalysts in Acid Media. *ACS Applied Energy Materials* 2(11):7952-7962.

Ren S, Joulie D, Salvatore D, Torbensen K, Wang M, Robert M, Berlinguette CP (2019a) Molecular electrocatalysts can mediate fast, selective CO_2 reduction in a flow cell. *Science* 365(6451):367-369.

Ren W, Tan X, Yang W, Jia C, Xu S, Wang K, Smith SC, Zhao C (2019b) Isolated Diatomic Ni-Fe Metal-Nitrogen Sites for Synergistic Electroreduction of CO_2. *Angewandte Chemie, International Edition in English* 58(21):6972-6976.

Ricciardulli T, Gorthy S, Adams JS, Thompson C, Karim AM, Neurock M, Flaherty DW (2021) Effect of Pd Coordination and Isolation on the Catalytic Reduction of O_2 to H_2O_2 over PdAu Bimetallic Nanoparticles. *Journal of the American Chemical Society* 143(14):5445-5464.

Rikkinen E, Santasalo-Aarnio A, Airaksinen S, Borghei M, Viitanen V, Sainio J, Kauppinen EI, Kallio T, Krause AOI (2011) Atomic Layer Deposition Preparation of Pd Nanoparticles on a Porous Carbon Support for Alcohol Oxidation. *The Journal of Physical Chemistry C* 115(46):23067-23073.

Ritala M (2000) Atomic Layer Deposition of Oxide Thin Films with Metal Alkoxides as Oxygen Sources. *Science* 288(5464):319-321.

Ross MB, Li Y, De Luna P, Kim D, Sargent EH, Yang P (2019) Electrocatalytic Rate Alignment Enhances Syngas Generation. *Joule* 3(1):257-264.

Roy A, Hursán D, Artyushkova K, Atanassov P, Janáky C, Serov A (2018) Nanostructured metal-N-C electrocatalysts for CO_2 reduction and hydrogen evolution reactions. *Applied Catalysis B: Environmental* 232:512-520.

Sarveena, Vargas JM, Shukla DK, Meneses CT, Mendoza Zelis P, Singh M, Sharma SK (2016) Synthesis, phase composition, Mossbauer and magnetic characterization of iron oxide nanoparticles. *Physical Chemistry Chemical Physics* 18(14):9561-9568.

Schiros T, Nordlund D, Palova L, Prezzi D, Zhao L, Kim KS, Wurstbauer U, Gutierrez C, Delongchamp D, Jaye C, Fischer D, Ogasawara H, Pettersson LG, Reichman DR, Kim P, Hybertsen MS, Pasupathy AN (2012) Connecting dopant bond type with electronic structure in N-doped graphene. *Nano Letters* 12(8):4025-4031.

Schneider J, Jia HF, Muckerman JT, Fujita E (2012) Thermodynamics and kinetics of CO_2, CO, and H+ binding to the metal centre of CO_2 reduction catalysts. *Chemical Society Reviews* 41(6):2036-2051.

Schreier M, Heroguel F, Steier L, Ahmad S, Luterbacher JS, Mayer MT, Luo JS, Gratzel M (2017) Solar conversion of CO_2 to CO using Earth-abundant electrocatalysts prepared by atomic layer modification of CuO. *Nature Energy* 2(7):17087.

Shan W, Liu R, Zhao H, He Z, Lai Y, Li S, He G, Liu J (2020) In Situ Surface-Enhanced Raman Spectroscopic Evidence on the Origin of Selectivity in CO_2 Electrocatalytic Reduction. *ACS Nano* 14(9):11363-11372.

Shao Z, Zhang C, Li Y, Shen H, Zhang D, Yu X, Zhang Y (2022) A Review of Non-Destructive Evaluation (NDE) Techniques for Residual Stress Profiling of Metallic Components in Aircraft Engines. *Aerospace* 9(10):534.

Shelke AR, Wang HT, Chiou JW, Shown I, Sabbah A, Chen KH, Teng SA, Lin IA, Lee CC, Hsueh HC, Liang YH, Du CH, Yadav PL, Ray SC, Hsieh SH, Pao CW, Tsai HM, Chen CH, Chen KH, Chen LC, Pong WF (2022) Bandgap Shrinkage and Charge Transfer in 2D Layered SnS_2 Doped with V for Photocatalytic Efficiency Improvement. *Small* 18(2):e2105076.

Shen SJ, Han C, Wang B, Du YA, Wang YD (2020) Dual active sites-dependent syngas proportions from aqueous CO_2 electroreduction. *Applied Catalysis B-Environmental* 279:119380.

Shi R, Guo J, Zhang X, Waterhouse GIN, Han Z, Zhao Y, Shang L, Zhou C, Jiang L, Zhang T (2020) Efficient wettability-controlled electroreduction of CO_2 to CO at Au/C interfaces. *Nat Commun* 11(1):3028.

Song Y, Mao J, Zhu C, Li S, Li G, Dong X, Jiang Z, Chen W, Wei W (2023) Ni Nanoclusters Anchored on Ni-N-C Sites for CO_2 Electroreduction at High Current Densities. *ACS Appl Mater Interfaces* 10.1021/acsami.2c23095.

Stiebritz MT, Hiller CJ, Sickerman NS, Lee CC, Tanifuji K, Ohki Y, Hu Y (2018) Ambient conversion of CO_2 to hydrocarbons by biogenic and synthetic $[Fe_4S_4]$ clusters. *Nature Catalysis* 10.1038/s41929-018-0079-4.

Sun D, Xu X, Qin Y, Jiang SP, Shao Z (2020) Rational Design of Ag-Based Catalysts for the Electrochemical CO_2 Reduction to CO: A Review. *ChemSusChem* 13(1):39-58.

Sun S, Zhang G, Gauquelin N, Chen N, Zhou J, Yang S, Chen W, Meng X, Geng D, Banis MN, Li R, Ye S, Knights S, Botton GA, Sham T-K, Sun X (2013) Single-atom Catalysis Using Pt/Graphene Achieved through Atomic Layer Deposition. *Scientific Reports* 3(1).

Sun X (2019) Highly Selective Electrochemical Reduction of CO_2 to Alcohols on FeP Nanoarray. *Angewandte Chemie, International Edition in English* 10.1002/anie.201912836.

Sun X, Suarez AIO, Meijerink M, van Deelen T, Ould-Chikh S, Zecevic J, de Jong KP, Kapteijn F, Gascon J (2017) Manufacture of highly loaded silica-supported cobalt Fischer-Tropsch catalysts from a metal organic framework. *Nat Commun* 8(1):1680.

Sun X, Tuo Y, Ye C, Chen C, Lu Q, Li G, Jiang P, Chen S, Zhu P, Ma M, Zhang J, Bitter JH, Wang D, Li Y (2021) Phosphorus Induced Electron Localization of Single Iron Sites for Boosted CO_2 Electroreduction Reaction. *Angewandte Chemie, International Edition in English* 60(44):23614-23618.

Suntola T (1989) Atomic layer epitaxy. *Materials Science Reports* 4(5):261-312.

Suntola T, Hyvarinen J (1985) Atomic Layer Epitaxy. *Annual Review of Materials Science* 15(1):177-195.

Switzer JA (2012) Chemistry. Atomic layer electrodeposition. *Science* 338(6112):1300-1301.

Terrer C, Phillips RP, Hungate BA, Rosende J, Pett-Ridge J, Craig ME, van Groenigen KJ, Keenan TF, Sulman BN, Stocker BD, Reich PB, Pellegrini AFA, Pendall E, Zhang H, Evans RD, Carrillo Y, Fisher JB, Van Sundert K, Vicca S, Jackson RB (2021) A trade-off between plant and soil carbon storage under elevated CO_2. *Nature* 591(7851):599-603.

Timm R, Head AR, Yngman S, Knutsson JV, Hjort M, McKibbin SR, Troian A, Persson O, Urpelainen S, Knudsen J, Schnadt J, Mikkelsen A (2018) Self-cleaning and surface chemical reactions during hafnium dioxide atomic layer deposition on indium arsenide. *Nat Commun* 9(1):1412.

Varghese OK, Paulose M, Latempa TJ, Grimes CA (2009) High-rate solar photocatalytic conversion of CO_2 and water vapor to hydrocarbon fuels. *Nano Letters* 9(2):731-737.

Vasileff A, Xu C, Jiao Y, Zheng Y, Qiao S-Z (2018) Surface and Interface Engineering in Copper-Based Bimetallic Materials for Selective CO_2 Electroreduction. *Chem* 4(8):1809-1831.

Vernon-Parry KD (2000) Scanning electron microscopy: an introduction. *III-Vs Review* 13(4):40-44.

Vijay S, Gauthier JA, Heenen HH, Bukas VJ, Kristoffersen HH, Chan KR (2020) Dipole-Field Interactions Determine the CO_2 Reduction Activity of 2D Fe-N-C Single-Atom Catalysts. *ACS Catalysis* 10(14):7826-7835.

Wang J, Huang Y-C, Wang Y, Deng H, Shi Y, Wei D, Li M, Dong C-L, Jin H, Mao SS, Shen S (2023) Atomically Dispersed Metal–Nitrogen–Carbon Catalysts with d-Orbital Electronic Configuration-Dependent Selectivity for Electrochemical CO_2-to-CO Reduction. *ACS Catalysis* 13(4):2374-2385.

Wang J, Kattel S, Hawxhurst CJ, Lee JH, Tackett BM, Chang K, Rui N, Liu CJ, Chen JG (2019a) Enhancing Activity and Reducing Cost for Electrochemical Reduction of CO_2 by Supporting Palladium on Metal Carbides. *Angewandte Chemie, International Edition in English* 58(19):6271-6275.

Wang T, Luo Z, Li C, Gong J (2014) Controllable fabrication of nanostructured materials for photoelectrochemical water splitting via atomic layer deposition. *Chemical Society Reviews* 43(22):7469-7484.

Wang T, Sang X, Zheng W, Yang B, Yao S, Lei C, Li Z, He Q, Lu J, Lei L, Dai L, Hou Y (2020a) Gas Diffusion Strategy for Inserting Atomic Iron Sites into Graphitized Carbon Supports for Unusually High-Efficient CO_2 Electroreduction and High-Performance Zn-CO_2 Batteries. *Advanced Materials* 32(29):e2002430.

Wang X, Chen Z, Zhao X, Yao T, Chen W, You R, Zhao C, Wu G, Wang J, Huang W, Yang J, Hong X, Wei S, Wu Y, Li Y (2018a) Regulation of Coordination Number over Single Co Sites: Triggering the Efficient Electroreduction of CO_2. *Angewandte Chemie, International Edition in English* 57(7):1944-1948.

Wang X, Wang ZL, Bai Y, Tan L, Xu YQ, Hao XJ, Wang JK, Mahadi AH, Zhao YF, Zheng LR, Song YF (2020b) Tuning the selectivity of photoreduction of CO_2 to syngas over Pd/layered double hydroxide nanosheets under visible light up to 600 nm. *Journal of Energy Chemistry* 46:1-7.

Wang Y, Liu J, Wang Y, Wang Y, Zheng G (2018b) Efficient solar-driven electrocatalytic CO_2 reduction in a redox-medium-assisted system. *Nat Commun* 9(1):5003.

Wang Y, Marquard SL, Wang D, Dares C, Meyer TJ (2017) Single-Site, Heterogeneous Electrocatalytic Reduction of CO_2 in Water as the Solvent. *ACS Energy Letters* 2(6):1395-1399.

Wang Y, Wang Z, Dinh C-T, Li J, Ozden A, Golam Kibria M, Seifitokaldani A, Tan C-S, Gabardo CM, Luo M, Zhou H, Li F, Lum Y, McCallum C, Xu Y, Liu M, Proppe A, Johnston A, Todorovic P, Zhuang T-T, Sinton D, Kelley SO, Sargent EH (2019b) Catalyst synthesis under CO_2 electroreduction favours faceting and promotes renewable fuels electrosynthesis. *Nature Catalysis* 3(2):98-106.

Wang ZL (2003) New Developments in Transmission Electron Microscopy for Nanotechnology. *Advanced Materials* 15(18):1497-1514.

Wei J, Ge Q, Yao R, Wen Z, Fang C, Guo L, Xu H, Sun J (2017) Directly converting CO_2 into a gasoline fuel. *Nat Commun* 8:15174.

Wei Q, Zhang G, Yang X, Fu Y, Yang G, Chen N, Chen W, Sun S (2018) Litchi-like porous Fe/N/C spheres with atomically dispersed FeNx promoted by sulfur as highly efficient oxygen electrocatalysts for Zn–air batteries. *Journal of Materials Chemistry A* 6(11):4605-4610.

Wen G, Ren B, Park MG, Yang J, Dou H, Zhang Z, Deng YP, Bai Z, Yang L, Gostick J, Botton GA, Hu Y, Chen Z (2020) Ternary Sn-Ti-O Electrocatalyst Boosts the Stability and Energy Efficiency of CO_2 Reduction. *Angewandte Chemie, International Edition in English* 59(31):12860-12867.

Wen GB, Lee DU, Ren BH, Hassan FM, Jiang GP, Cano ZP, Gostick J, Croiset E, Bai ZY, Yang L, Chen ZW (2018) Orbital Interactions in Bi-Sn Bimetallic Electrocatalysts for Highly Selective Electrochemical CO_2 Reduction toward Formate Production. *Advanced Energy Materials* 8(31):1802427.

Woyessa GW, dela Cruz J-aB, Rameez M, Hung C-H (2021) Nanocomposite catalyst of graphitic carbon nitride and Cu/Fe mixed metal oxide for electrochemical CO_2 reduction to CO. *Applied Catalysis B: Environmental* 291:120052.

Wu CH, Liu C, Su D, Xin HL, Fang H-T, Eren B, Zhang S, Murray CB, Salmeron MB (2018) Bimetallic synergy in cobalt–palladium nanocatalysts for CO oxidation. *Nature Catalysis* 2(1):78-85.

Wu J, Huang Y, Ye W, Li Y (2017) CO_2 Reduction: From the Electrochemical to Photochemical Approach. *Adv Sci (Weinh)* 4(11):1700194.

Wu M, Zhang G, Chen N, Chen W, Qiao J, Sun S (2020a) A self-supported electrode as a high-performance binder- and carbon-free cathode for rechargeable hybrid zinc batteries. *Energy Storage Materials* 24:272-280.

Wu M, Zhang G, Hu Y, Wang J, Sun T, Regier T, Qiao J, Sun S (2020b) Graphitic-shell encapsulated FeNi alloy/nitride nanocrystals on biomass-derived N-doped carbon as an efficient electrocatalyst for rechargeable Zn-air battery. *Carbon Energy* 3(1):176-187.

Wu Y, Jiang Z, Lu X, Liang Y, Wang H (2019) Domino electroreduction of CO_2 to methanol on a molecular catalyst. *Nature* 575(7784):639-642.

Wuttig A, Yoon Y, Ryu J, Surendranath Y (2017) Bicarbonate Is Not a General Acid in Au-Catalyzed CO_2 Electroreduction. *Journal of the American Chemical Society* 139(47):17109-17113.

Xia C, Zhu P, Jiang Q, Pan Y, Liang WT, Stavitsk E, Alshareef HN, Wang HT (2019) Continuous production of pure liquid fuel solutions via electrocatalytic CO_2 reduction using solid-electrolyte devices. *Nature Energy* 4(9):776-785.

Xiao FX, Pagliaro M, Xu YJ, Liu B (2016) Layer-by-layer assembly of versatile nanoarchitectures with diverse dimensionality: a new perspective for rational construction of multilayer assemblies. *Chemical Society Reviews* 45(11):3088-3121.

Xie J, Liao L, Gong Y, Li Y, Shi F, Pei A, Sun J, Zhang R, Kong B, Subbaraman R, Christensen J, Cui Y (2017) Stitching h-BN by atomic layer deposition of LiF as a stable interface for lithium metal anode. *Sci Adv* 3(11):eaao3170.

Xie J, Yang P, Wang Y, Qi T, Lei Y, Li CM (2018) Puzzles and confusions in supercapacitor and battery: Theory and solutions. *Journal of Power Sources* 401:213-223.

Yan C, Li H, Ye Y, Wu H, Cai F, Si R, Xiao J, Miao S, Xie S, Yang F, Li Y, Wang G, Bao X (2018) Coordinatively unsaturated nickel–nitrogen sites towards selective and high-rate CO_2 electroreduction. *Energy & Environmental Science* 11(5):1204-1210.

Yang D, Ni B, Wang X (2020a) Heterogeneous Catalysts with Well-Defined Active Metal Sites toward CO_2 Electrocatalytic Reduction. *Advanced Energy Materials* 10(25):2001142.

Yang H, Lin Q, Zhang C, Yu X, Cheng Z, Li G, Hu Q, Ren X, Zhang Q, Liu J, He C (2020b) Carbon dioxide electroreduction on single-atom nickel decorated carbon membranes with industry compatible current densities. *Nature Communications* 11(1).

Yang H, Wu Y, Li G, Lin Q, Hu Q, Zhang Q, Liu J, He C (2019) Scalable Production of Efficient Single-Atom Copper Decorated Carbon Membranes for CO_2 Electroreduction to Methanol. *Journal of the American Chemical Society* 141(32):12717-12723.

Yang HB, Hung S-F, Liu S, Yuan K, Miao S, Zhang L, Huang X, Wang H-Y, Cai W, Chen R, Gao J, Yang X, Chen W, Huang Y, Chen HM, Li CM, Zhang T, Liu B (2018) Atomically dispersed Ni(i) as the active site for electrochemical CO_2 reduction. *Nature Energy* 3(2):140-147.

Yang J, Li W, Wang D, Li Y (2020c) Single-Atom Materials: Small Structures Determine Macroproperties. *Small Structures* 2(2):2000051.

Yang X, Wang M, Zachman MJ, Zhou H, He Y, Liu S, Zang H-Y, Feng Z, Wu G (2021) Binary Atomically Dispersed Metal-Site Catalysts with Core−Shell Nanostructures for O_2 and CO_2 Reduction Reactions. *Small Science* 10.1002/smsc.202100046:2100046.

Yang X, Wang Y, Zhang G, Du L, Yang L, Markiewicz M, Choi J-y, Chenitz R, Sun S (2020d) SiO_2-Fe/N/C catalyst with enhanced mass transport in PEM fuel cells. *Applied Catalysis B: Environmental* 264:118523.

Yang X, Zhang G, Du L, Zhang J, Chiang FK, Wen Y, Wang X, Wu Y, Chen N, Sun S (2020e) PGM-Free Fe/N/C and Ultralow Loading Pt/C Hybrid Cathode Catalysts with Enhanced Stability and Activity in PEM Fuel Cells. *ACS Appl Mater Interfaces* 12(12):13739-13749.

Yang XF, Wang A, Qiao B, Li J, Liu J, Zhang T (2013) Single-atom catalysts: a new frontier in heterogeneous catalysis. *Accounts of Chemical Research* 46(8):1740-1748.

Yao D, Tang C, Vasileff A, Zhi X, Jiao Y, Qiao SZ (2021) The Controllable Reconstruction of Bi-MOFs for Electrochemical CO_2 Reduction through Electrolyte and Potential Mediation. *Angewandte Chemie, International Edition in English* 60(33):18178-18184.

Ye Y, Cai F, Li H, Wu H, Wang G, Li Y, Miao S, Xie S, Si R, Wang J, Bao X (2017) Surface functionalization of ZIF-8 with ammonium ferric citrate toward high exposure of Fe-N active sites for efficient oxygen and carbon dioxide electroreduction. *Nano Energy* 38:281-289.

Yin SH, Yang J, Han Y, Li G, Wan LY, Chen YH, Chen C, Qu XM, Jiang YX, Sun SG (2020) Construction of Highly Active Metal-Containing Nanoparticles and FeCo-N_4 Composite

Sites for the Acidic Oxygen Reduction Reaction. *Angewandte Chemie* 132(49):22160-22163.

Yuan L, Xu YJ (2015) Photocatalytic conversion of CO_2 into value-added and renewable fuels. *Applied Surface Science* 342:154-167.

Zamora Zeledon JA, Stevens MB, Gunasooriya G, Gallo A, Landers AT, Kreider ME, Hahn C, Norskov JK, Jaramillo TF (2021) Tuning the electronic structure of Ag-Pd alloys to enhance performance for alkaline oxygen reduction. *Nat Commun* 12(1):620.

Zhang A, He R, Li H, Chen Y, Kong T, Li K, Ju H, Zhu J, Zhu W, Zeng J (2018a) Nickel Doping in Atomically Thin Tin Disulfide Nanosheets Enables Highly Efficient CO_2 Reduction. *Angewandte Chemie, International Edition in English* 10.1002/anie.201806043.

Zhang B, Zhang B, Jiang Y, Ma T, Pan H, Sun W (2021a) Single-Atom Electrocatalysts for Multi-Electron Reduction of CO_2. *Small* 10.1002/smll.202101443:e2101443.

Zhang C, Yang S, Wu J, Liu M, Yazdi S, Ren M, Sha J, Zhong J, Nie K, Jalilov AS, Li Z, Li H, Yakobson BI, Wu Q, Ringe E, Xu H, Ajayan PM, Tour JM (2018b) Electrochemical CO_2 Reduction with Atomic Iron-Dispersed on Nitrogen-Doped Graphene. *Advanced Energy Materials* 8(19):1703487.

Zhang G, Chenitz R, Lefèvre M, Sun S, Dodelet J-P (2016) Is iron involved in the lack of stability of Fe/N/C electrocatalysts used to reduce oxygen at the cathode of PEM fuel cells? *Nano Energy* 29:111-125.

Zhang G, Jia Y, Zhang C, Xiong X, Sun K, Chen R, Chen W, Kuang Y, Zheng L, Tang H, Liu W, Liu J, Sun X, Lin W-F, Dai H (2019a) A general route via formamide condensation to prepare atomically dispersed metal–nitrogen–carbon electrocatalysts for energy technologies. *Energy & Environmental Science* 12(4):1317-1325.

Zhang G, Sun S, Sun X (2013a) Atomic Layer Deposition of Metals and Metal Oxides for Fuel Cells Applications. *Nanostructured and Advanced Materials for Fuel Cells*, Jiang SP, Shen PK (Édit.) CRC Press, Boca Raton. p 249-289.

Zhang G, Yang X, Dubois M, Herraiz M, Chenitz R, Lefèvre M, Cherif M, Vidal F, Glibin VP, Sun S, Dodelet J-P (2019b) Non-PGM electrocatalysts for PEM fuel cells: effect of fluorination on the activity and stability of a highly active NC_Ar + NH_3 catalyst. *Energy & Environmental Science* 12(10):3015-3037.

Zhang H, Hwang S, Wang M, Feng Z, Karakalos S, Luo L, Qiao Z, Xie X, Wang C, Su D, Shao Y, Wu G (2017) Single Atomic Iron Catalysts for Oxygen Reduction in Acidic Media: Particle Size Control and Thermal Activation. *Journal of the American Chemical Society* 139(40):14143-14149.

Zhang H, Liu G, Shi L, Ye J (2018c) Single-Atom Catalysts: Emerging Multifunctional Materials in Heterogeneous Catalysis. *Advanced Energy Materials* 8(1):1701343.

Zhang N, Zhang X, Kang Y, Ye C, Jin R, Yan H, Lin R, Yang J, Xu Q, Wang Y, Zhang Q, Gu L, Liu L, Song W, Liu J, Wang D, Li Y (2021b) Supported Pd2 Dual-atom Site Catalyst for Efficient Electrochemical CO_2 Reduction. *Angewandte Chemie, International Edition in English* 10.1002/anie.202101559.

Zhang T, Walsh AG, Yu J, Zhang P (2021c) Single-atom alloy catalysts: structural analysis, electronic properties and catalytic activities. *Chemical Society Reviews* 50(1):569-588.

Zhang W, Qin Q, Dai L, Qin R, Zhao X, Chen X, Ou D, Chen J, Chuong TT, Wu B, Zheng N (2018d) Electrochemical Reduction of Carbon Dioxide to Methanol on Hierarchical

Pd/SnO_2 Nanosheets with Abundant Pd-O-Sn Interfaces. *Angewandte Chemie, International Edition in English* 57(30):9475-9479.

Zhang Y, Jiao L, Yang W, Xie C, Jiang HL (2021d) Rational Fabrication of Low-Coordinate Single-Atom Ni Electrocatalysts by MOFs for Highly Selective CO_2 Reduction. *Angewandte Chemie, International Edition in English* 60(14):7607-7611.

Zhang Y, Su X, Li L, Qi H, Yang C, Liu W, Pan X, Liu X, Yang X, Huang Y, Zhang T (2020a) Ru/TiO_2 Catalysts with Size-Dependent Metal/Support Interaction for Tunable Reactivity in Fischer–Tropsch Synthesis. *ACS Catalysis* 10(21):12967-12975.

Zhang Z, Pan S-Y, Li H, Cai J, Olabi AG, Anthony EJ, Manovic V (2020b) Recent advances in carbon dioxide utilization. *Renewable and Sustainable Energy Reviews* 125:109799.

Zhang Z, Xiao J, Chen XJ, Yu S, Yu L, Si R, Wang Y, Wang S, Meng X, Wang Y, Tian ZQ, Deng D (2018e) Reaction Mechanisms of Well-Defined Metal-N4 Sites in Electrocatalytic CO_2 Reduction. *Angewandte Chemie, International Edition in English* 57(50):16339-16342.

Zhang ZY, Patterson M, Ren MM, Wang Y, Flake JC, Sprunger PT, Kurtz RL (2013b) Atomic layer deposition of ZnO on Cu-nanoclusters for methanol synthesis. *Journal of Vacuum Science & Technology A* 31(1).

Zhao C, Dai X, Yao T, Chen W, Wang X, Wang J, Yang J, Wei S, Wu Y, Li Y (2017) Ionic Exchange of Metal-Organic Frameworks to Access Single Nickel Sites for Efficient Electroreduction of CO_2. *Journal of the American Chemical Society* 139(24):8078-8081.

Zhao Y, Wang C, Liu Y, MacFarlane DR, Wallace GG (2018a) Engineering Surface Amine Modifiers of Ultrasmall Gold Nanoparticles Supported on Reduced Graphene Oxide for Improved Electrochemical CO_2 Reduction. *Advanced Energy Materials* 8(25):1801400.

Zhao Z, Liu H, Gao W, Xue W, Liu Z, Huang J, Pan X, Huang Y (2018b) Surface-Engineered PtNi-O Nanostructure with Record-High Performance for Electrocatalytic Hydrogen Evolution Reaction. *Journal of the American Chemical Society* 140(29):9046-9050.

Zheng T, Jiang K, Ta N, Hu Y, Zeng J, Liu J, Wang H (2018) Large-Scale and Highly Selective CO_2 Electrocatalytic Reduction on Nickel Single-Atom Catalyst. *Joule* 10.1016/j.joule.2018.10.015.

Zheng X, De Luna P, García de Arquer FP, Zhang B, Becknell N, Ross MB, Li Y, Banis MN, Li Y, Liu M, Voznyy O, Dinh CT, Zhuang T, Stadler P, Cui Y, Du X, Yang P, Sargent EH (2017) Sulfur-Modulated Tin Sites Enable Highly Selective Electrochemical Reduction of CO_2 to Formate. *Joule* 1(4):794-805.

Zhou JH, Yuan K, Zhou L, Guo Y, Luo MY, Guo XY, Meng QY, Zhang YW (2019a) Boosting Electrochemical Reduction of CO_2 at a Low Overpotential by Amorphous Ag-Bi-S-O Decorated Bi^0 Nanocrystals. *Angewandte Chemie, International Edition in English* 58(40):14197-14201.

Zhou W, Cheng K, Kang J, Zhou C, Subramanian V, Zhang Q, Wang Y (2019b) New horizon in C1 chemistry: breaking the selectivity limitation in transformation of syngas and hydrogenation of CO_2 into hydrocarbon chemicals and fuels. *Chemical Society Reviews* 10.1039/c8cs00502h.

Zhou X, Dong J, Zhu Y, Liu L, Jiao Y, Li H, Han Y, Davey K, Xu Q, Zheng Y, Qiao SZ (2021) Molecular Scalpel to Chemically Cleave Metal-Organic Frameworks for Induced Phase Transition. *Journal of the American Chemical Society* 143(17):6681-6690.

Zhou X, Li K, Lin Y, Song L, Liu J, Liu Y, Zhang L, Wu Z, Song S, Li J, Zhang H (2020a) A Single-Atom Manipulation Approach for Synthesis of Atomically Mixed Nanoalloys as Efficient Catalysts. *Angewandte Chemie, International Edition in English* 59(32):13568-13574.

Zhou X, Shan J, Chen L, Xia BY, Ling T, Duan J, Jiao Y, Zheng Y, Qiao SZ (2022) Stabilizing Cu(2+) Ions by Solid Solutions to Promote CO_2 Electroreduction to Methane. *Journal of the American Chemical Society* 144(5):2079-2084.

Zhou Y, King DM, Liang XH, Li JH, Weimer AW (2010) Optimal preparation of Pt/TiO_2 photocatalysts using atomic layer deposition. *Applied Catalysis B-Environmental* 101(1-2):54-60.

Zhou Y, Tao X, Chen G, Lu R, Wang D, Chen MX, Jin E, Yang J, Liang HW, Zhao Y, Feng X, Narita A, Mullen K (2020b) Multilayer stabilization for fabricating high-loading single-atom catalysts. *Nat Commun* 11(1):5892.

Zhu J, Yang Y, Chen L, Xiao W, Liu H, Abruña HD, Wang D (2018) Copper-Induced Formation of Structurally Ordered Pt–Fe–Cu Ternary Intermetallic Electrocatalysts with Tunable Phase Structure and Improved Stability. *Chemistry of Materials* 30(17):5987-5995.

Zhu S, Delmo EP, Li T, Qin X, Tian J, Zhang L, Shao M (2021) Recent Advances in Catalyst Structure and Composition Engineering Strategies for Regulating CO_2 Electrochemical Reduction. *Advanced Materials* 10.1002/adma.202005484:e2005484.

Zu X, Li X, Liu W, Sun Y, Xu J, Yao T, Yan W, Gao S, Wang C, Wei S, Xie Y (2019) Efficient and Robust Carbon Dioxide Electroreduction Enabled by Atomically Dispersed $Sn(delta)^+$ Sites. *Advanced Materials* 10.1002/adma.201808135:e1808135.

Zuo Y, Li T, Zhang N, Jing T, Rao D, Schmuki P, Kment S, Zboril R, Chai Y (2021) Spatially Confined Formation of Single Atoms in Highly Porous Carbon Nitride Nanoreactors. *ACS Nano* 10.1021/acsnano.1c01872.

8 ANNEXE I: The supplements to Chapter 3

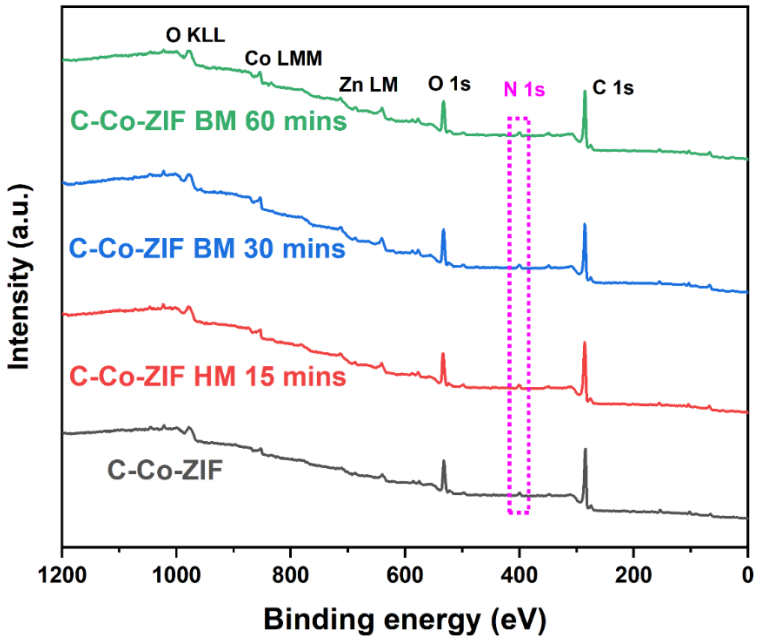

Figure 8.1 The XPS surveys of the C-Co-ZIF samples with different grinding processes.

Table 8.1 The absolute contents of different elements in the C-Co-ZIF samples with different grinding processes.

	C at%	N at%	O at%	Co at%	Zn at%
C-Co-ZIF	78.97	3.08	17.56	0.18	0.20
C-Co-ZIF HM 15 mins	79.07	3.55	16.94	0.22	0.21
C-Co-ZIF BM 30 mins	77.06	3.66	18.87	0.20	0.20
C-Co-ZIF BM 60 mins	78.87	3.11	17.67	0.17	0.18

Table 8.2 The absolute contents of the N element and metal-N contents in the C-Co-ZIF samples with different grinding processes and TOF results of CO production at -0.7 V vs. RHE.

	Absolute N wt% from the XPS survey	Relative M-N content % from N1s analysis	Absolute M-N wt% in the samples	TOF (site-1 s-1)
C-Co-ZIF	3.33	8.75	0.29	1.08
C-Co-ZIF HM 15 mins	3.83	9.17	0.35	1.91
C-Co-ZIF BM 30 mins	3.93	8.67	0.34	1.36
C-Co-ZIF BM 60 mins	3.36	9.00	0.30	1.43

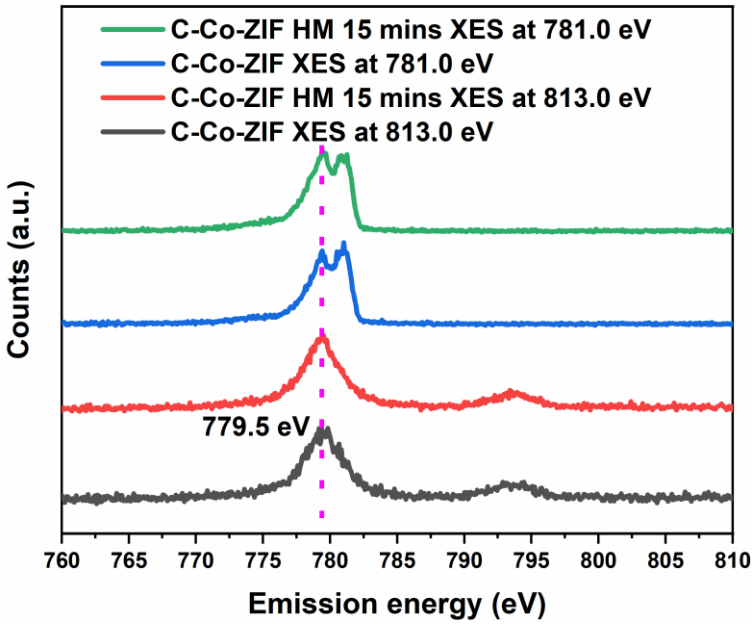

Figure 8.2 XES spectra comparison of C-Co-ZIF and C-Co-ZIF HM 15 mins, excited at 781.0 eV and 813.0 eV.

Table 8.3 The EIS charge transfer and mass transfer resistance results of the C-Co-ZIF samples with different grinding processes.

	Charge transfer resistance (Ω)	Mass transfer resistance (Ω)
C-Co-ZIF	3.35	2.01
C-Co-ZIF HM 15 mins	3.73	2.81
C-Co-ZIF BM 30 mins	3.96	4.88
C-Co-ZIF BM 60 mins	4.08	29.08

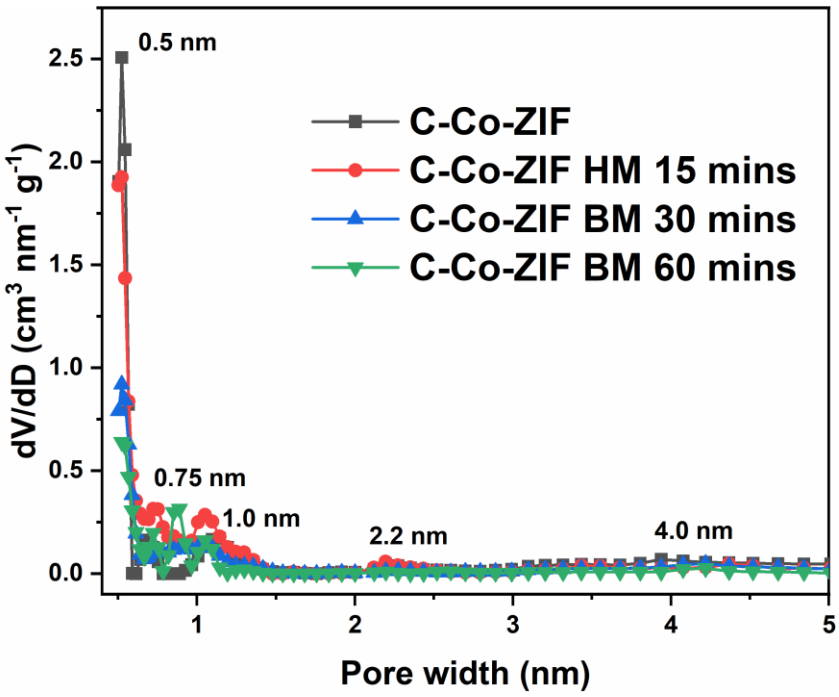

Figure 8.3 The pore size distribution analysis in the 0-5 nm region.

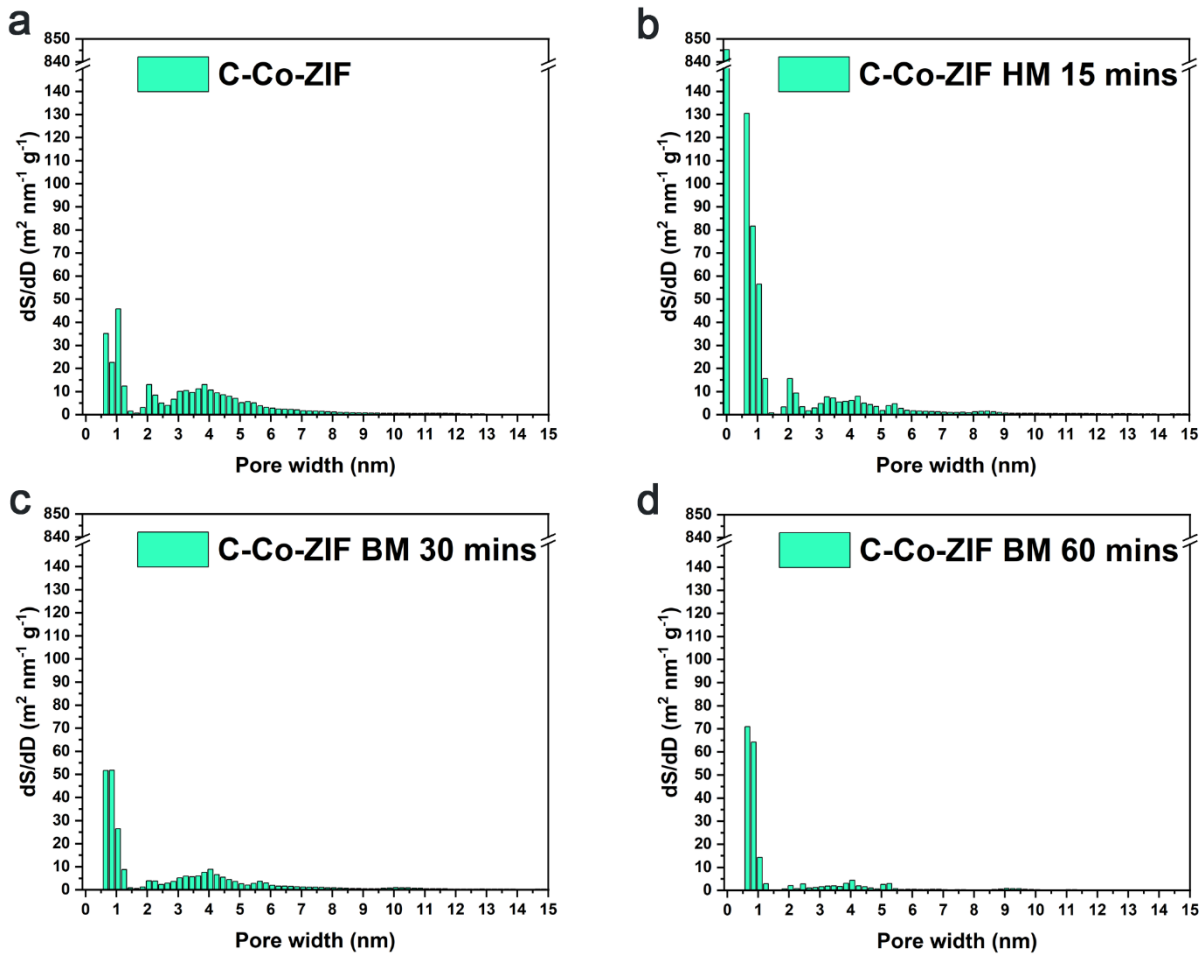

Figure 8.4 (a-d) The surface area distribution (0-15 nm) analysis of C-Co-ZIF samples with different grinding processes.

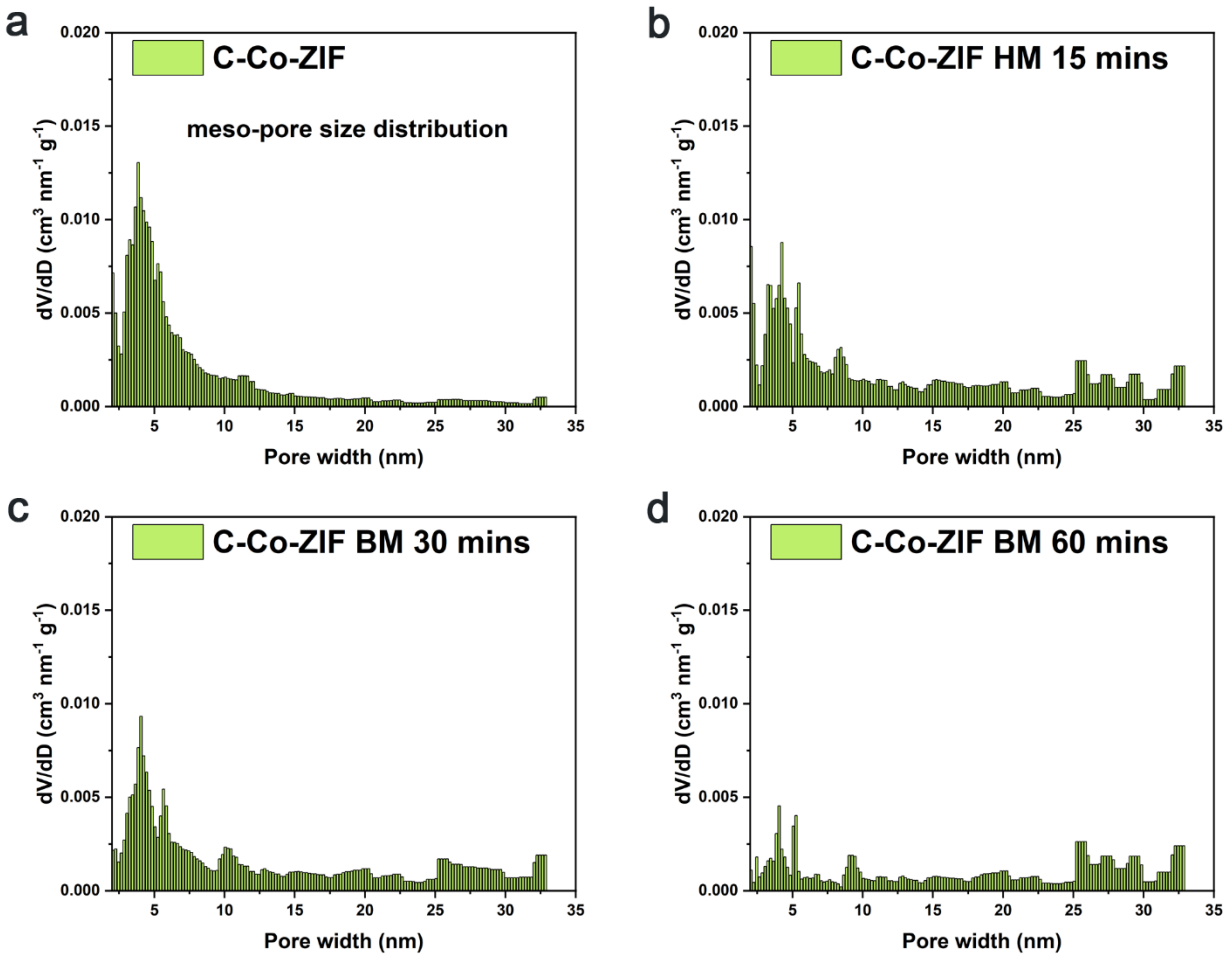

Figure 8.5 (a-d) The meso-pore size distribution analysis of C-Co-ZIF samples with different grinding processes.

9 ANNEXE II The supplements to Chapter 4

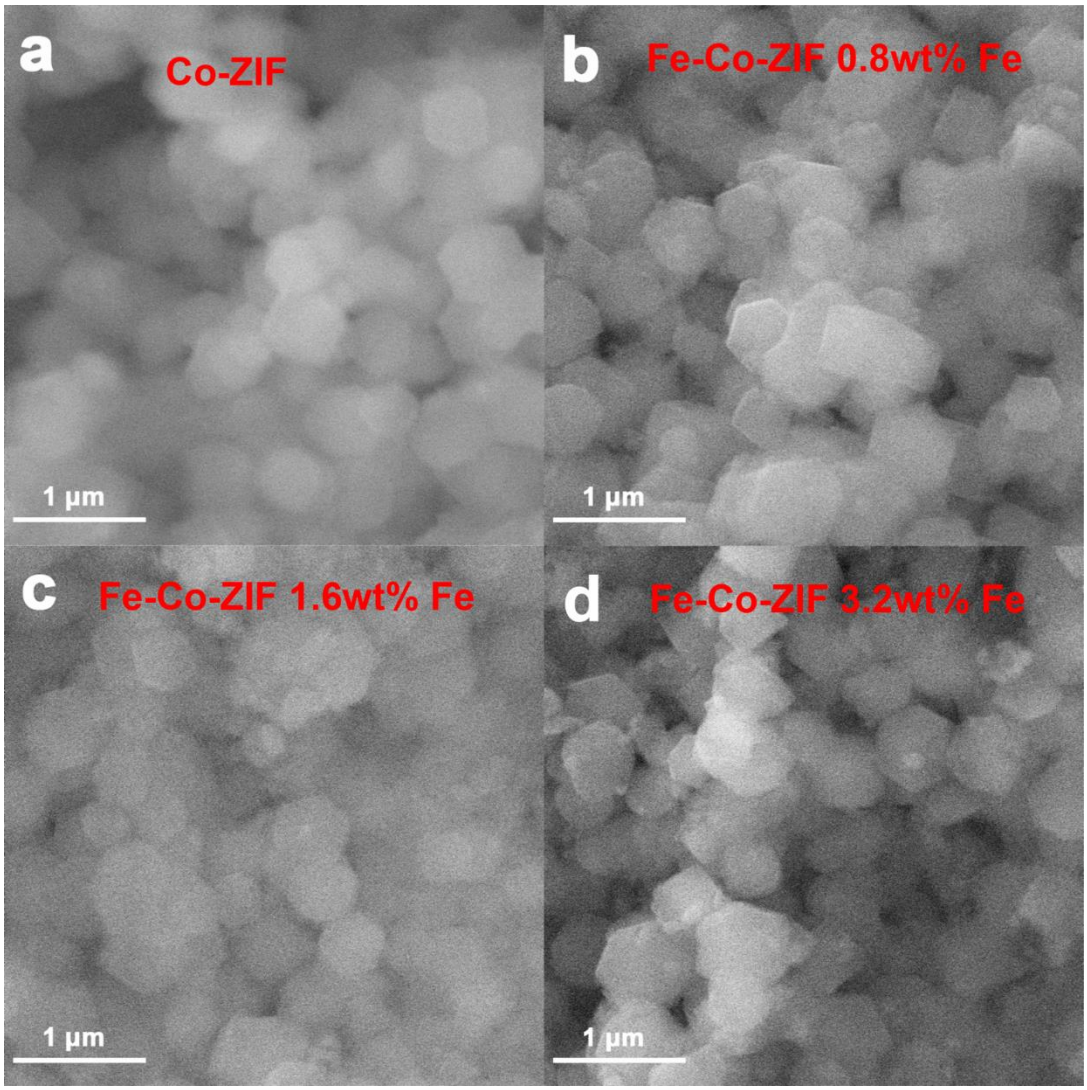

Figure 9.1 SEM images of (a) Co-ZIF powders. (b) Fe-Co-ZIF-0.8 wt%-Fe powders. (c) Fe-Co-ZIF-1.6 wt%-Fe powders. (d) Fe-Co-ZIF-3.2 wt%-Fe powders.

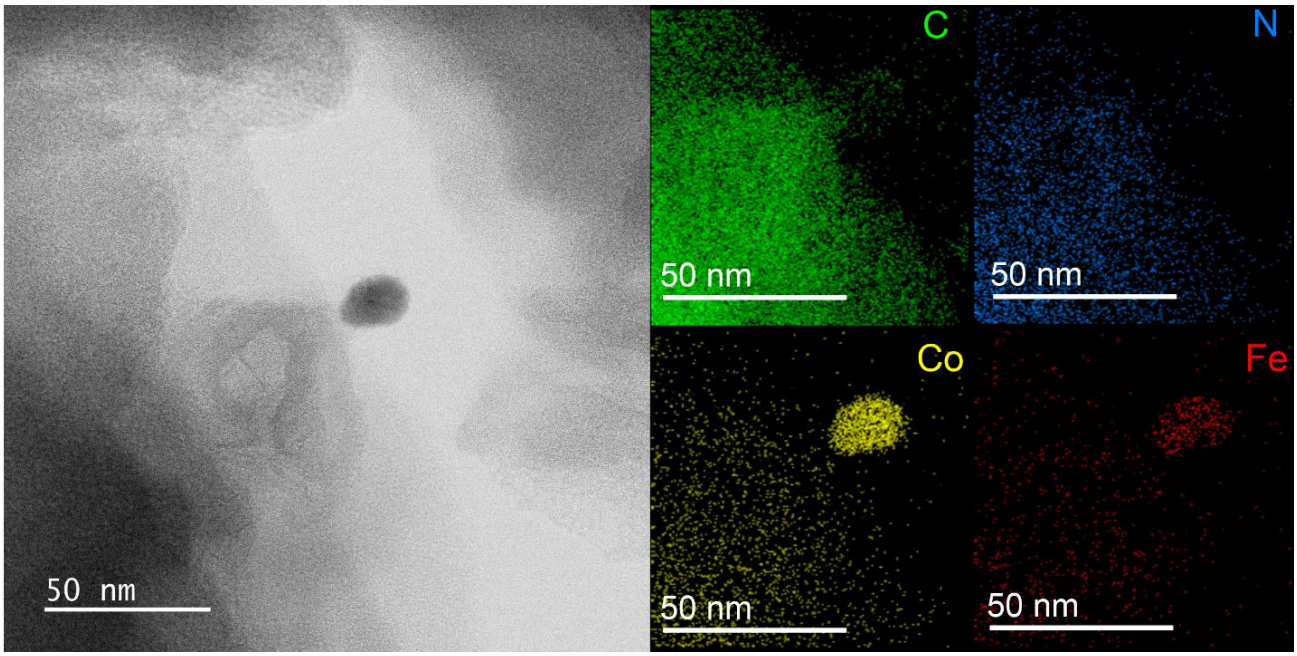

Figure 9.2 TEM and EDX images of the clusters in the sample of C-Fe-Co-ZIF-3.2 wt%-Fe.

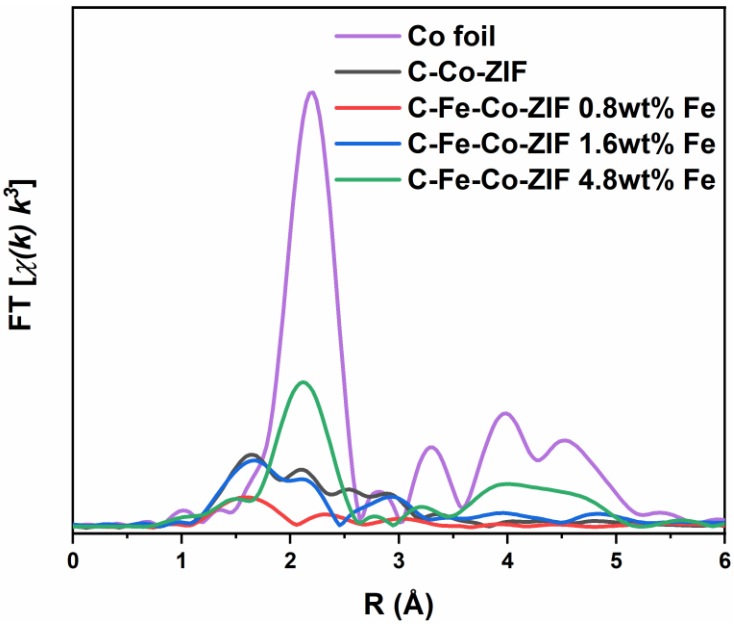

Figure 9.3 EXAFS of Co foil, C-Co-ZIF, and C-Fe-Co-ZIF catalysts.

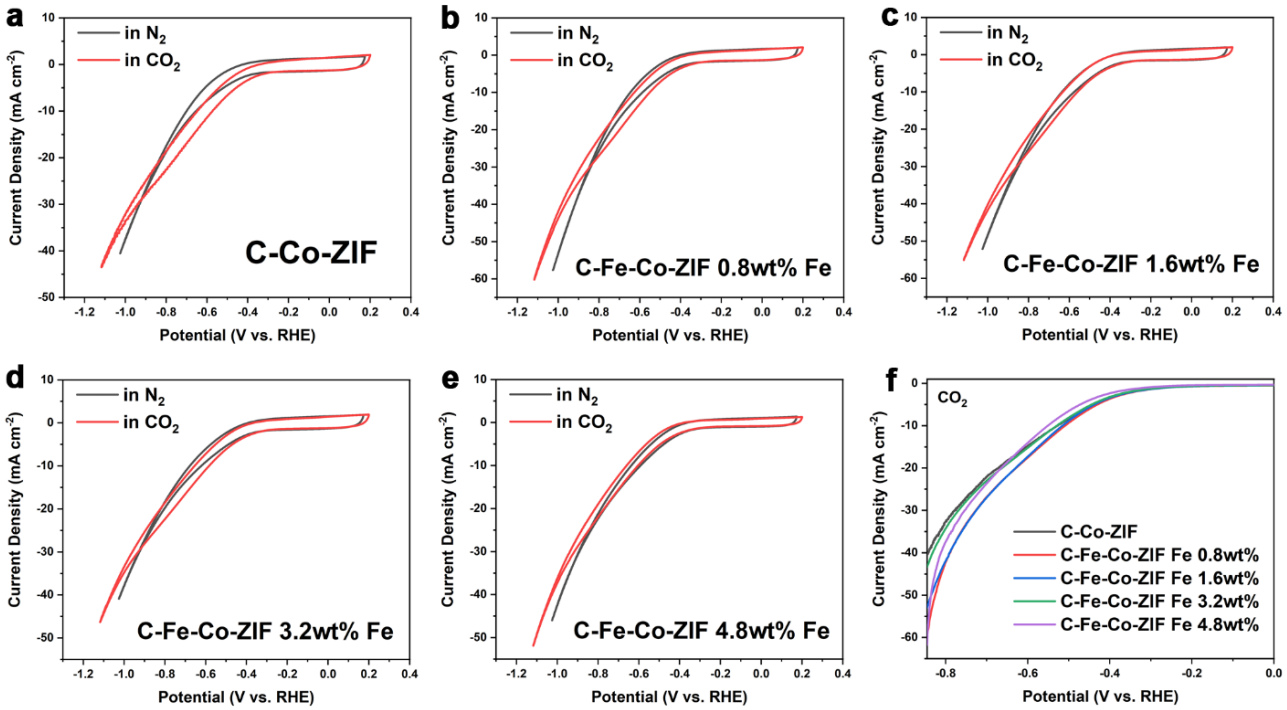

Figure 9.4 Cyclic voltammograms of (a) C-Co-ZIF. (b) C-Fe-Co-ZIF-0.8 wt%-Fe. (c) C-Fe-Co-ZIF-1.6 wt%-Fe. (d) C-Fe-Co-ZIF-3.2 wt%-Fe. (e) C-Fe-Co-ZIF-4.8 wt%-Fe in CO_2-saturated 0.5 M $KHCO_3$ solution at a scan rate of 20 mV s^{-1} (no iR-compensation was made during CV tests). (f) LSV curves of the samples in CO_2-saturated 0.5 M $KHCO_3$ solution at a scan rate of 5 mV s^{-1} (80% iR-compensation).

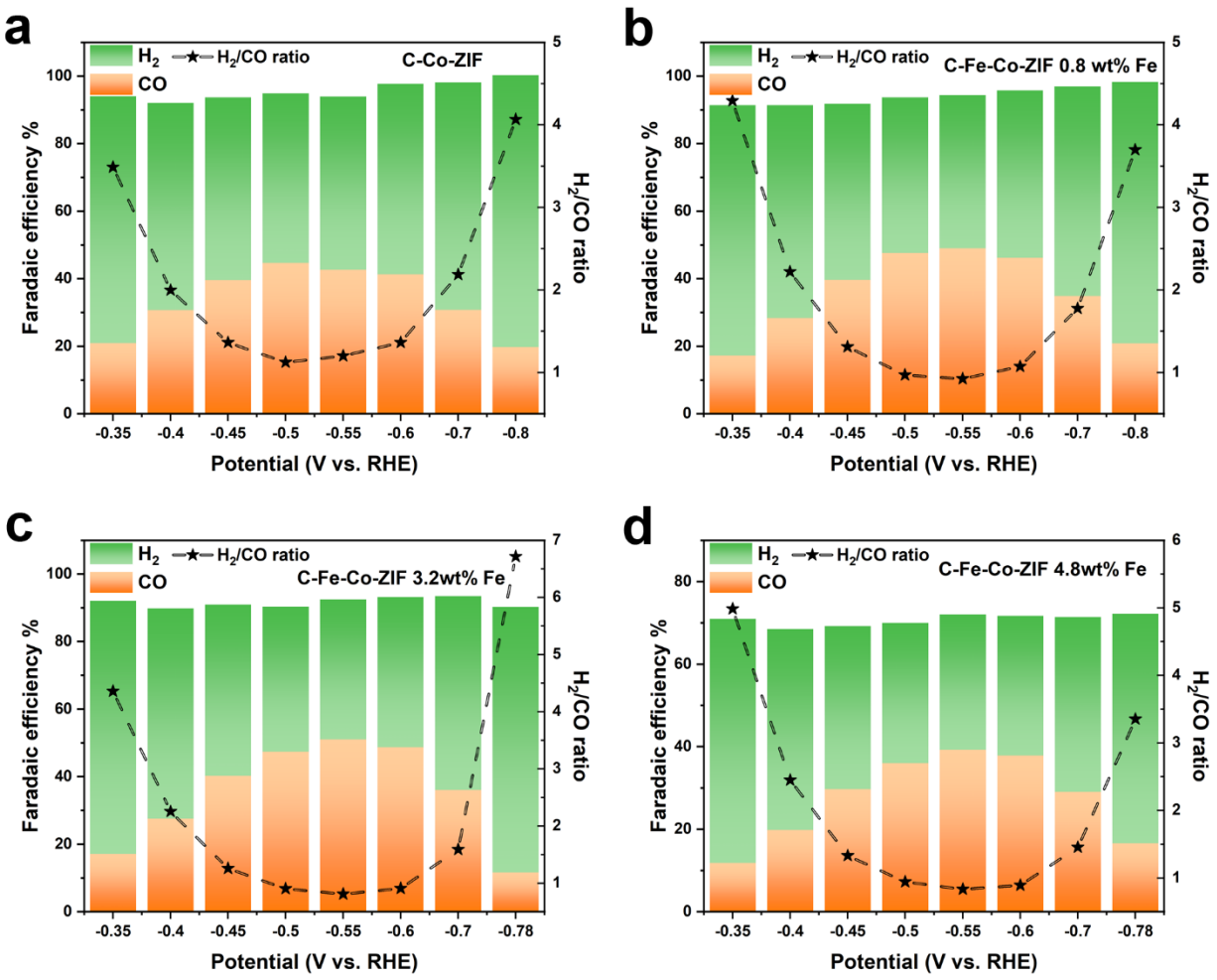

Figure 9.5 Bars: FE_{CO} and FE_{H2}; Stars: H_2/CO ratio of (a) C-Co-ZIF. (b) C-Fe-Co-ZIF-0.8 wt%-Fe. (c) C-Fe-Co-ZIF-3.2 wt%-Fe. (d) C-Fe-Co-ZIF-4.8 wt%-Fe at various applied potentials.

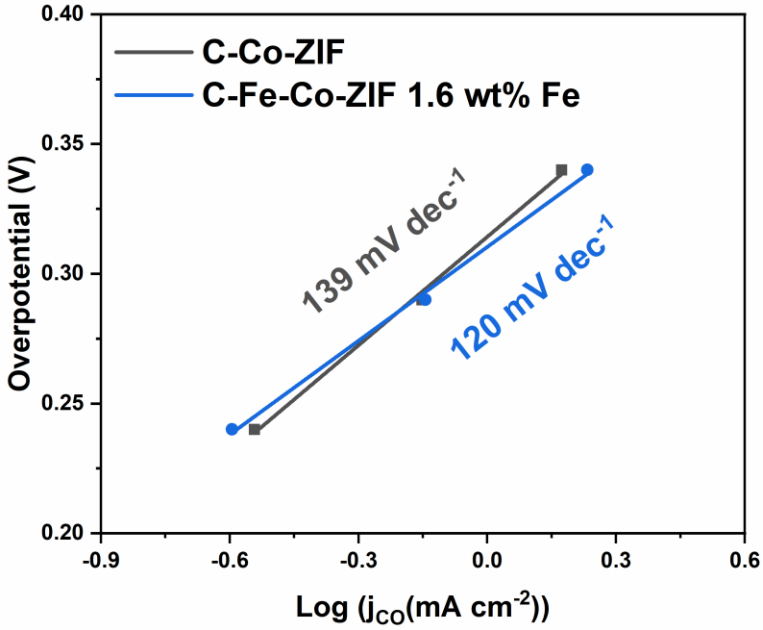

Figure 9.6 Tafel slopes of C-Co-ZIF and C-Fe-Co-ZIF-1.6 wt%-Fe.

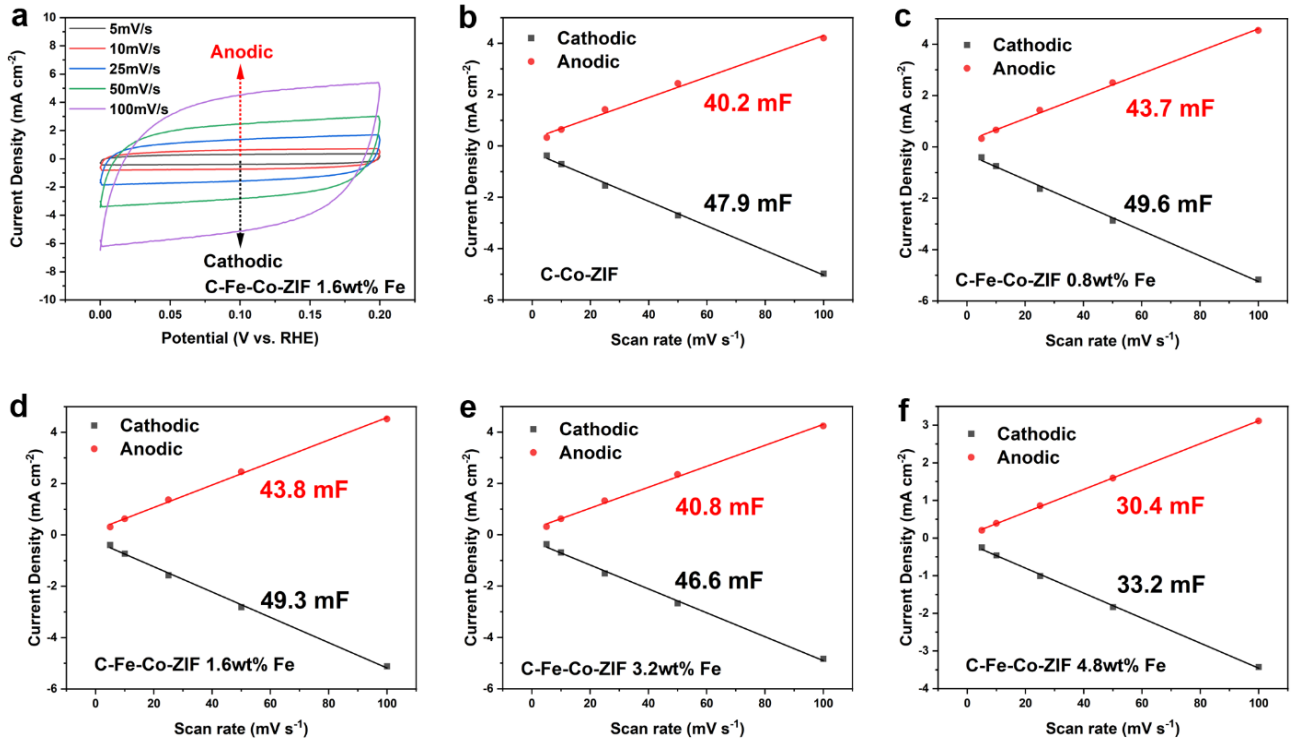

Figure 9.7 Double-layer capacitance tests for evaluating the electrochemical active surface area of the catalysts (a) CVs of C-Fe-Co-ZIF-1.6 wt%Fe sample with scan rate from 5 mV s^{-1} to 100 mV s^{-1}. The cathodic (dark line) and anodic (red line) currents were measured at 0.10 V vs. RHE as a function of the scan rate of (b) C-Co-ZIF. (c) C-Fe-Co-ZIF-0.8 wt%-Fe. (d) C-Fe-Co-ZIF-1.6 wt%-Fe. (e) C-Fe-Co-ZIF-3.2 wt%-Fe. (f) C-Fe-Co-ZIF-4.8 wt%-Fe. The average value of the cathodic and anodic slopes is taken as the double-layer capacitance of the catalyst electrode.

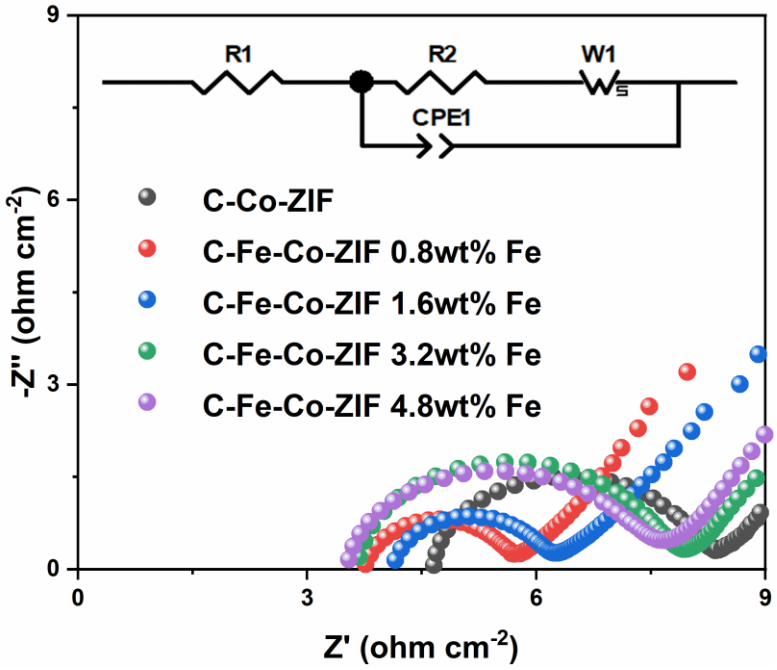

Figure 9.8 EIS results of C-Co-ZIF and C-Fe-Co-ZIF catalysts.

Table 9.1 Resistance of the catalysts at open circuit potential

	Resistance (Ω)
C-Co-ZIF	3.691
C-Fe-Co-ZIF-0.8 wt%-Fe	2.028
C-Fe-Co-ZIF-1.6 wt%-Fe	2.085
C-Fe-Co-ZIF-3.2 wt%-Fe	4.149
C-Fe-Co-ZIF-4.8 wt%-Fe	4.296

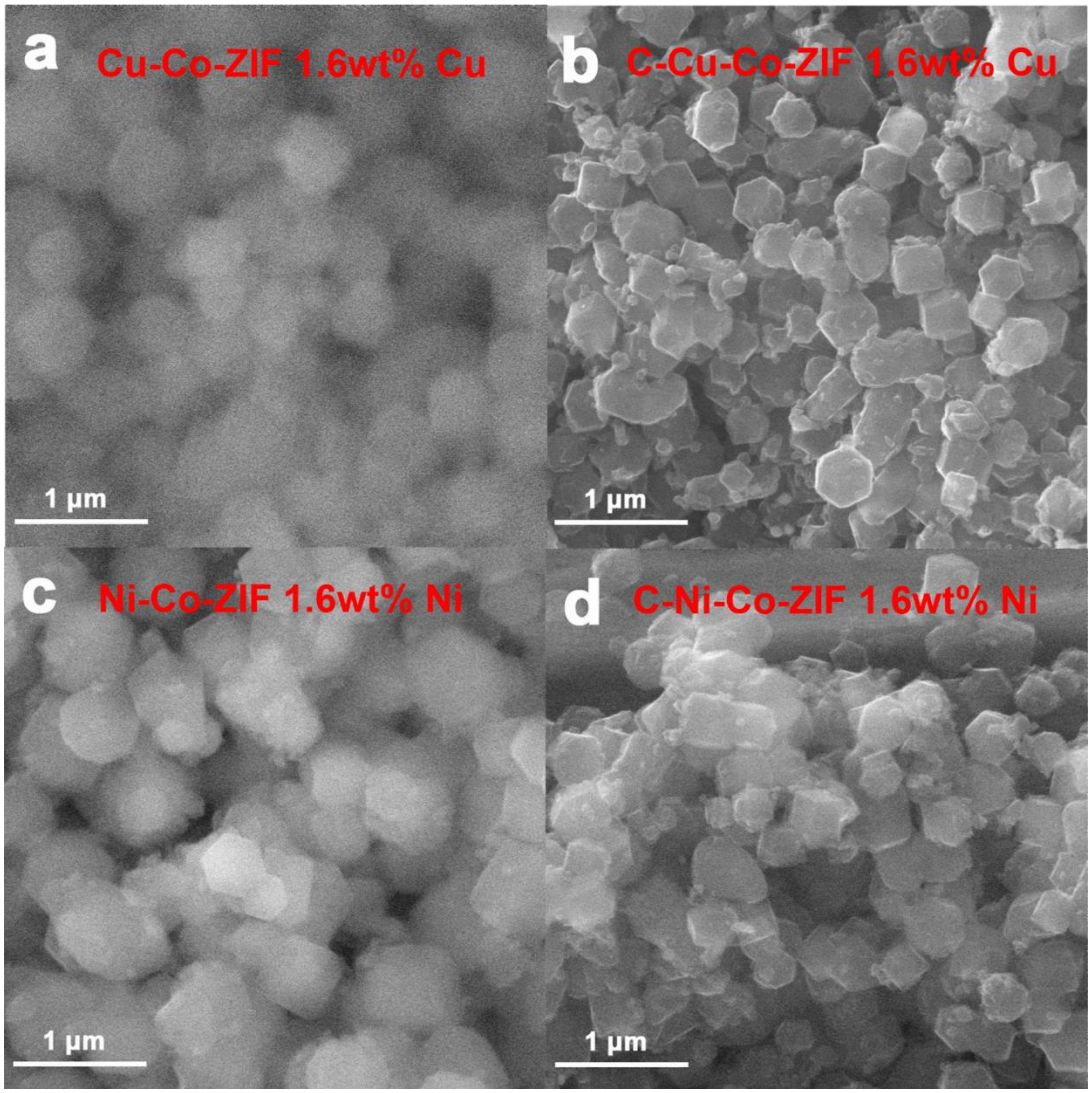

Figure 9.9 SEM images of a Cu-Co-ZIF-1.6 wt%-Cu. b C-Cu-Co-ZIF-1.6 wt%-Cu. c Ni-Co-ZIF-1.6 wt%-Ni. d C-Ni-Co-ZIF-1.6 wt%-Ni.

All the original and carbonized Cu-Co-ZIFs and Ni-Co-ZIFs have the same morphology with a particle size of around 300 nm. It illustrates that the series of Cu and Ni modified Co-ZIF samples retain the morphology of the original Co-ZIFs independent of the metal sources during the synthesis and pyrolysis processes.

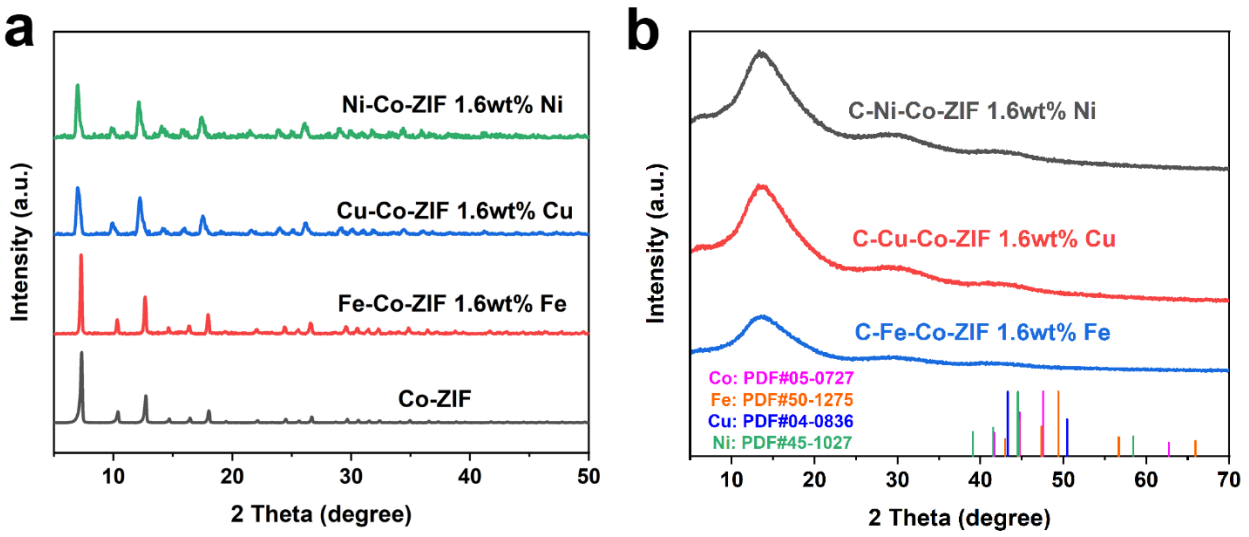

Figure 9.10 XRD patterns of (a) M-Co-ZIF samples with M adding the amount of 1.6 wt% (M=Ni, Cu, Co). (b) C-M-Co-ZIF samples with M adding the amount of 1.6 wt% (M=Ni, Cu, Fe).

Cu-Co-ZIF and Ni-Co-ZIF share the same crystalline structure as that of Fe-Co-ZIF, without any characteristic peak assigned to Cu and Ni crystals. It indicates that Cu-Co-ZIF and Ni-Co-ZIF keep the same crystalline structure as that of Co-ZIF as well. After the pyrolysis, carbonized Cu-Co-ZIF (C-Cu-Co-ZIF) and carbonized Ni-Co-ZIF (C-Ni-Co-ZIF) also appear to be the amorphous carbon material, same as C-Fe-Co-ZIF.

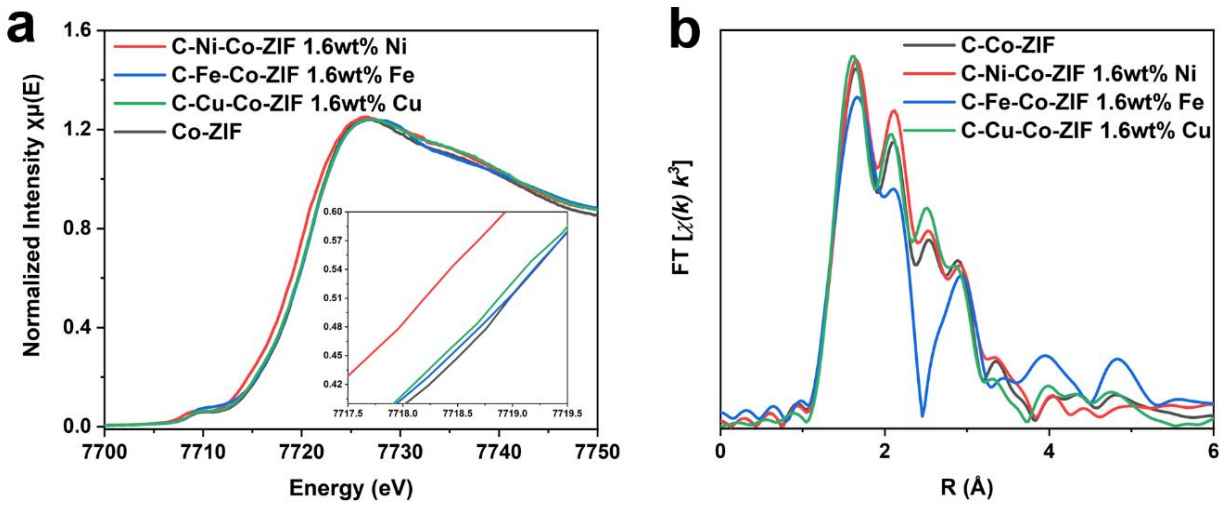

Figure 9.11 (a) XANES (insert: enlarged white line region). (b) EXAFS of C-Co-ZIF and C-M-Co-ZIF samples with M adding amount of 1.6 wt% (M=Ni, Cu, Fe).

In **Fig. S11a**, the valances of Co atoms in C-Fe-Co-ZIF and C-Cu-Co-ZIF are close to that of C-Co-ZIF while the introduction of Ni reduces the valance of Co atoms in the catalyst, which is relatively greater than Fe and Cu.

The atomically dispersed state of the TM atoms and the interactions between Co and the introduced foreign TM atoms (Cu and Ni) are also confirmed by the analysis of EXAFS (**Fig. S11b**) where peaks at M-N and M-M regions appear for both C-Cu-Co-ZIF and C-Ni-Co-ZIF. Compared to C-Fe-Co-ZIF, the Co *R* space patterns in C-Cu-Co-ZIF and C-Ni-Co-ZIF are closer to that of C-Co-ZIF.

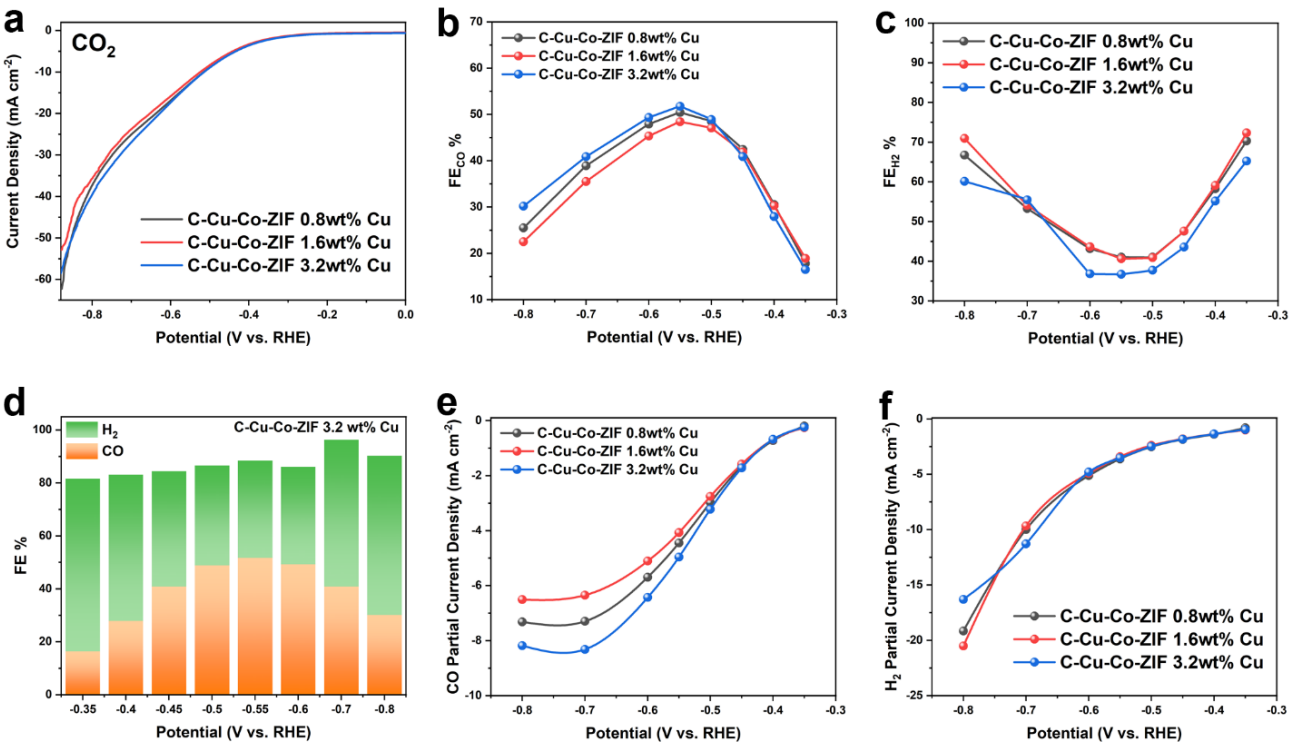

Figure 9.12 The evaluation of the electrocatalytic performance of C-Cu-Co-ZIF with different Cu adding amounts. (a) LSV curves in CO_2-saturated 0.5 M $KHCO_3$ solution at a scan rate of 5 mV s^{-1}. (b) CO Faradaic efficiency of the catalysts at various applied potentials. (c) H_2 Faradaic efficiency of the catalysts at various applied potentials. (d) Total Faradaic efficiency of CO and H_2 of C-Cu-Co-ZIF-3.2 wt%-Cu at various applied potentials. (e) CO current density of the catalysts. (f) H_2 current density of the catalysts.

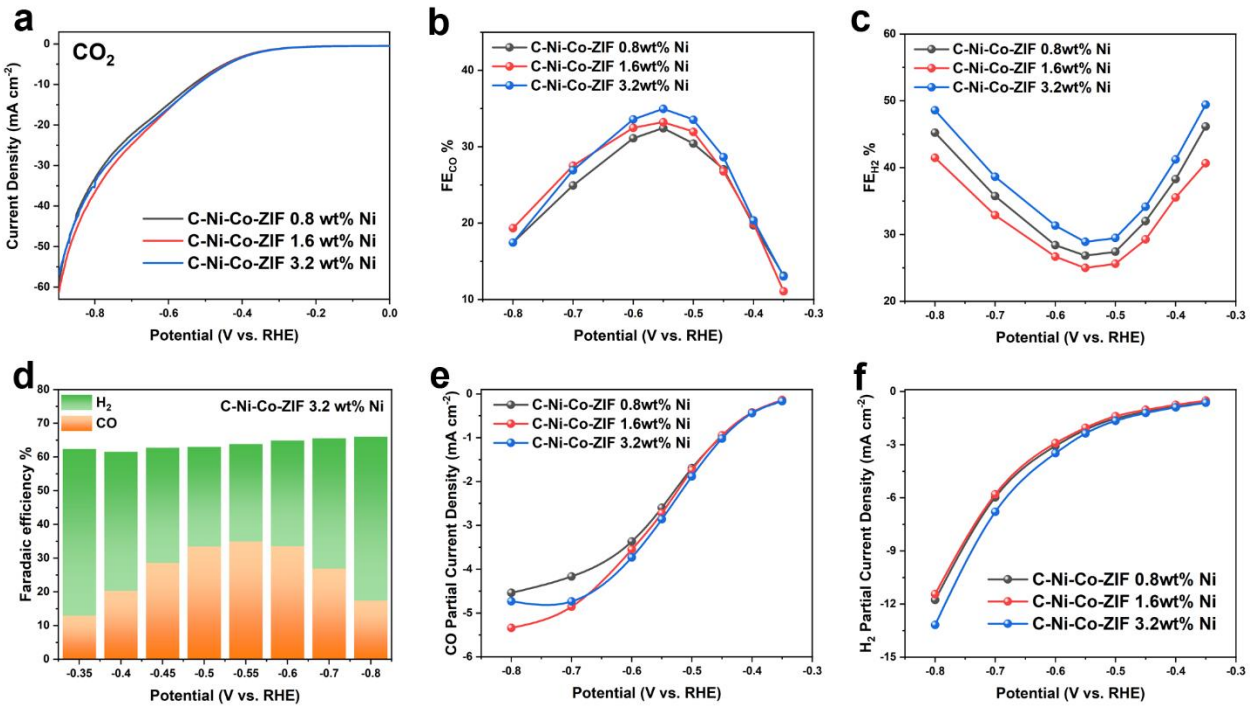

Figure 9.13 The evaluation of the electrocatalytic performance of C-Ni-Co-ZIF with different Ni adding amounts. (a) LSV curves in CO_2-saturated 0.5 M $KHCO_3$ solution at a scan rate of 5 mV s^{-1}. (b) CO Faradaic efficiency of the catalysts at various applied potentials. (c) H_2 Faradaic efficiency of the catalysts at various applied potentials. (d) Total Faradaic efficiency of CO and H_2 of C-Ni-Co-ZIF-3.2wt%-Ni at various applied potentials. (e) CO current density of the catalysts. (f) H_2 current density of the catalysts.

10 ANNEXE II The supplements to Chapter 5

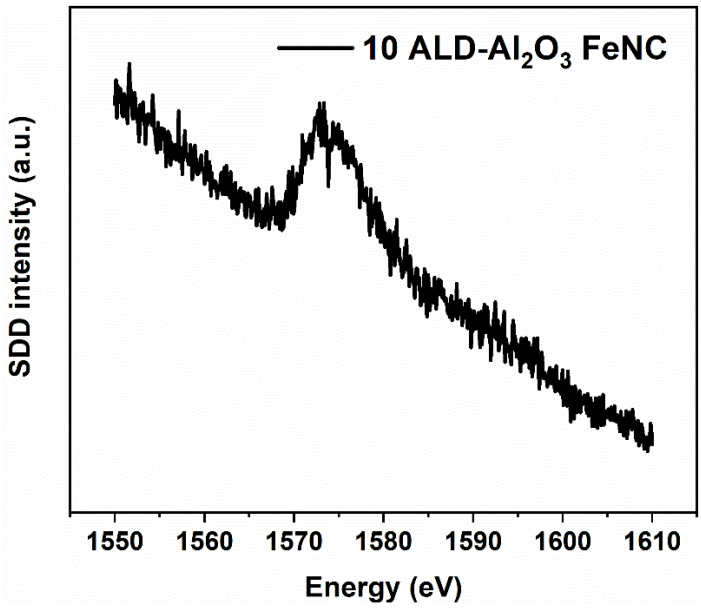

Figure 10.1 Al K-edge XAS of 10 ALD-Al_2O_3 FeNC.

Small ALD-Al_2O_3 cycles such as 10 cannot even present a distinguishable feature in Al K-edge XAS.